

Performance Assessment of a Zeolite Heat Store

by

Muhammad Sheik

Submitted in fulfilment of the academic requirements for the degree of Master of Science in
Mechanical Engineering, College of Agriculture, Engineering and Science,
University of KwaZulu-Natal

Supervisor: Prof. Graham Smith (UKZN)

Co-supervisor: Dr Peter Klein (CSIR)

Declaration 1 - Plagiarism

I, Muhammad Sheik, declare that

1. The research reported in this thesis, except where otherwise indicated, is my original research.
2. This thesis has not been submitted for any degree or examination at any other university.
3. This thesis does not contain other persons' data, pictures, graphs or other information, unless specifically acknowledged as being sourced from other persons.
4. This thesis does not contain other persons' writing, unless specifically acknowledged as being sourced from other researchers. Where other written sources have been quoted, then:
 - a. Their words have been re-written but the general information attributed to them has been referenced
 - b. Where their exact words have been used, then their writing has been placed in italics and inside quotation marks, and referenced.
5. This thesis does not contain text, graphics or tables copied and pasted from the Internet, unless specifically acknowledged, and the source being detailed in the thesis and in the References sections.

Signed: _____ Date: _____.

Mr Muhammad Sheik

As the candidate's supervisor I have approved this dissertation for submission.

Signed: _____ Date: _____.

Prof Graham Smith: BSc Eng. (Natal), MSc Eng. (Natal), PhD (Cantab)

As the candidate's co-supervisor I have approved this dissertation for submission.

Signed: _____ Date: _____.

Dr Peter Klein: BSc Eng. (Wits), PhD (Wits)

Declaration 2 - Publications

Publication 1: SASEC - 2021 (Published)

Sheik M., Klein P., Segakweng T., “*Experimental Analysis of a zeolite Heat Storage System*” 7th Southern African Sustainable Energy Conference, Stellenbosch, 2021

Muhammad Sheik was the primary author of this paper and conducted all the research contained with supervision from Dr Peter Klein and assistance from Tshiamo Segakweng in setting up the experimental apparatus.

Signed: _____ Date: _____.

Mr Muhammad Sheik

Acknowledgements

I would like to acknowledge the Council for Scientific and Industrial Research (CSIR) for funding this research and providing me with the opportunity to further my studies. I would like to sincerely thank my supervisors Prof. Graham Smith and Dr Peter Klein for their continuous support and guidance during the project. Finally, I would like to thank my parents (Shabbir and Aisha Sheik), grandparents (Mahomed Haniff and Haffiza Buckus), sisters (Fathima and Zaakira Sheik) and the rest of the family for their prayers, support and encouragement throughout my studies.

Abstract

According to the Department of Mineral Resources and Energy, the industrial sector in South Africa is the largest consumer of energy. Waste heat recovery can significantly reduce costs and carbon emissions in industry. In addition, energy supply does not always match demand and it is therefore necessary to investigate efficient ways of storing thermal energy. Sorption based thermochemical heat storage provides high energy densities while minimizing losses when utilised for long-term heat storage. To commercialize sorption storage systems, additional research and experimentation is required to validate numerical models of heat and mass transfer within the system to allow for accurate design calculations.

A lab-scale prototype was developed to analyse the thermal storage characteristics of zeolite 13X in an open (non-pressurized) sorption system. The test unit consists of a packed (pellet) bed reactor, heating system, blower, and humidifier. Thermocouples, humidity sensors, and mass-flow meters were used to determine the mass and energy balances in the system. The experiments that were conducted involved a reversible reaction between zeolite 13X and water vapour in air. During the charging (desorption) process, the zeolite pellets were dehydrated by hot air which was heated using an electric heater. During the discharging (adsorption) process, humidified ambient air was supplied to the reactor bed, which rehydrated the zeolite pellets, resulting in hot dry air exiting the reactor bed.

The packed bed was charged at three different temperatures (130 °C, 160 °C and 200 °C). It was discharged at three different values of relative humidity (25%, 70% and 100%,) and mass-flow rates (90 kg/h, 126 kg/h and 177 kg/h). The maximum amount of energy absorbed by the bed was 13.64 kWh (at 200 °C) and the maximum amount of energy released was 11.56 kWh at 100% relative humidity during discharging. This equates to a storage efficiency of 85% and an overall efficiency of 57% for the process. The highest temperature lift achieved was 107 °C during adsorption and the maximum energy storage density was 148 kWh/m³. By decreasing the regeneration temperature, the energy storage capacity was decreased and the desorption time was increased. A lower inlet humidity (during discharging) lowered the temperature lift and energy efficiency and increased the adsorption time. A lower flow rate also led to a lower efficiency and increased the adsorption time. The potential of zeolite 13X for long term storage was confirmed as a relatively high energy storage efficiency of 72% was achieved, for a period of 5 months between charging and discharging, in an open reactor.

The application of zeolite for drying processes in industry was demonstrated using ceramic casting moulds. An average drying rate (water removal) of 0.67 kg/h was achieved. The moisture adsorption capacity of zeolite 13X was also investigated and a maximum of 286 g_{water}/kg_{zeolite} was adsorbed at a relative humidity of 85%. The performance of the system was analysed by comparing the experimental results to calculations and models from previous studies. The next step is to develop and test a pilot-scale rig in a small-scale ceramic factory.

Table of Contents

Declaration 1 - Plagiarism	ii
Declaration 2 - Publications	iii
Publication 1: SASEC - 2021 (Published)	iii
Acknowledgements	iv
Abstract	v
List of Figures	x
List of Tables	xiii
Nomenclature	xiv
Symbols	xiv
Subscripts	xv
Abbreviations	xvi
Acronyms	xvi
1 Introduction	1
1.1 Background	1
1.2 Applications of Thermochemical Energy Storage	2
1.3 Aims and Objectives	4
1.4 Thesis outline	5
2 Literature Review	6
2.1 Thermal Energy Storage Technologies	6
2.1.1 Sensible Heat Storage	6
2.1.2 Latent Heat Storage	8
2.1.3 Thermochemical Energy Storage	10
2.2 Adsorption	11
2.3 Adsorbents: Zeolite	13
2.4 Open and Closed Adsorption Systems	15
2.5 Existing Studies and Systems Utilising Zeolite for Adsorption	16
2.5.1 ZAE Bayern	16
2.5.2 Diponegoro University/ Wageningen University	16
2.5.3 University of Stuttgart	18
2.5.4 University of Savoy Mont Blanc	19
2.5.5 ZAE Bayern: Mobile Storage	20
2.5.6 Eindhoven University of Technology	21
2.6 Conclusion	22
3 Experimental Design, Apparatus, and Method	23
3.1 Packed Bed Test Rig	23
3.2 Thermocouple Positions	26

3.3	Experimental Method.....	27
3.3.1	Determination of the effect of charging temperature.....	27
3.3.2	Determination of the effect of humidity.....	27
3.3.3	Determination of the effect of flow rate.....	27
3.4	Experimental Scope	27
3.4.1	Maximum temperature, variable humidity, maximum flow rate,	27
3.4.2	Maximum temperature, maximum humidity, variable flow rate	28
3.4.3	Variable temperature, maximum humidity, maximum flow rate.....	28
3.4.4	Prospect of long-term heat storage.....	28
3.4.5	Partial charge/discharge cycles	28
3.4.6	Industrial application of zeolite 13X.....	28
3.4.7	Moisture adsorption capacity of zeolite 13X	28
3.5	Experimental Analysis	28
4	Energy Analysis of an Open Sorption System.....	29
4.1	Conservation of mass principle.....	30
4.1.1	Charging cycle	30
4.1.2	Discharging cycle.....	30
4.2	Conservation of energy principle.....	31
4.2.1	Charging cycle	31
4.2.2	Discharging cycle.....	32
4.2.3	Overall Process	33
4.3	Energy Efficiency	33
4.3.1	Charging Process.....	33
4.3.2	Discharging Process.....	33
4.3.3	Overall Process	33
5	Experimental Results	34
5.1	Charging/ Regeneration Cycle Testing	34
5.1.1	Charging Cycles 1-3.....	35
5.2	Discharging Cycle Testing.....	40
5.2.1	Discharging Cycle 1: 100% RH.....	41
5.2.2	Discharging Cycles 2 and 3 (70% and 25% RH).....	45
5.2.3	Discharging Cycles 4 and 5 (70% and 50% Flowrate)	45
5.2.4	Discharging Cycles 6 and 7 (160 °C and 130 °C Regeneration Temperature).....	46
5.2.5	Discharging Cycle 8: 5 months after regeneration.....	48
5.3	Additional Charging/Discharging Results	50
5.3.1	Charging cycle after partial discharge.....	50
5.3.2	Discharging cycle including sensible heat	51

5.4	Drying Ceramic Casting Moulds	51
5.4.1	Apparatus and Method	51
5.4.2	Results: Controlling Kiln Temperature	53
5.4.3	Results: Drying Tests	55
5.5	Moisture Adsorption Capacity of Zeolite 13X at Different Relative Humidities	55
5.5.1	Apparatus and Method	55
5.5.2	Results	56
6	Performance Analysis of Experimental System	58
6.1	Energy Efficiency of System	58
6.1.1	Introduction	58
6.1.2	Calculations	58
6.1.3	Conclusion	61
6.2	Temperature Lift	61
6.2.1	Introduction	61
6.2.2	Calculations	61
6.2.3	Conclusion	64
6.3	Energy Storage Capacity	64
6.3.1	Introduction	64
6.3.2	Calculations	64
6.3.3	Conclusion	67
6.4	Moisture Adsorption Capacity	67
6.4.1	Introduction	67
6.4.2	Calculation	67
6.4.3	Conclusion	68
6.5	Sample Calculation	69
6.5.1	Introduction	69
6.5.2	Calculation	69
6.5.3	Conclusion	70
7	Conclusions and Recommendations	71
7.1	Experimental Testing	71
7.2	Performance Analysis	73
7.3	Recommendations for Future Work	74
	References	75
	Appendix A: Experimental Apparatus	79
	Equipment and Instrumentation Utilised	79
	Humidifier	79
	Electric Heater	79

Primary Blower	80
Secondary Blower	80
Data Logger	81
Conical Inlet for Air Flow Rate Measurement.....	81
Humidity Sensors.....	82
Pressure Transducers	84
Assembly of Rig	84
Appendix B: Detailed Experimental Results	89
Charging Cycle 2: 160 °C	89
Charging Cycle 3: 130 °C	91
Discharging Cycle 2: ~70% RH.....	93
Discharging Cycle 3: ~25% RH.....	96
Discharging Cycle 4: 70% Flow rate	99
Discharging Cycle 5: 50% Flow rate	102
Discharging Cycle 6: 160 °C Regeneration temperature	105
Discharging Cycle 7: 130 °C Regeneration temperature.....	108
Discharging Cycle 8: 5 months after regeneration.....	111
Appendix C: Sample Calculation for Energy Balance.....	114
Charging Cycle 1	114
Energy Supplied (Q_{in}).....	116
Energy Stored (Q_s)	116
Discharging Cycle 1.....	116
Energy Released/discharged (Q_d)	117
Energy Efficiencies of the System	117
Charging Efficiency (η_c)	117
Discharging/Storage Efficiency (η_d)	117
Overall Efficiency (η_o)	117
Appendix D: Zeolite 13X Properties and Supplier Details.....	118

List of Figures

Figure 1-1: SA DMRE Energy Balances, 2018 [1].....	1
Figure 1-2: WHR System Including Thermal Storage [4].....	2
Figure 1-3: Ceramic manufacturing process [14].....	3
Figure 1-4: Schematic of a Solar Thermal System with Integrated Thermochemical Storage [15].....	4
Figure 2-1: Thermal Storage Techniques [6].....	6
Figure 2-2: Phase transition profile of PCM [20].....	8
Figure 2-3: Volume required to store energy to meet annual needs of an average household [22].....	11
Figure 2-4: Graphic Representation Adsorption and Desorption Process [25].....	12
Figure 2-5: Primary Building Blocks of zeolite [32].....	14
Figure 2-6: Secondary Building Blocks of zeolite [33].....	14
Figure 2-7: Schematic of Open and Closed Adsorption System [36].....	15
Figure 2-8: Charging / discharging modes of TCES developed in Munich [37].....	16
Figure 2-9: Experimental set-up of zeolite-dryer rig [38].....	17
Figure 2-10: Test Rig [5].....	18
Figure 2-11: Schematic of test bed [15].....	20
Figure 2-12: Mobile Sorption reactors [31].....	21
Figure 2-13: Schematic view of system and reactor.....	21
Figure 3-1: Diagram of packed bed test facility (charging/ desorption configuration).....	24
Figure 3-2: Diagram of packed bed test facility (discharging/ adsorption configuration).....	24
Figure 3-3: CAD model of packed bed test facility.....	25
Figure 3-4: Full Assembly showing charging (left) and discharging (right) configuration.....	25
Figure 3-5: Thermocouples placed in reactor bed (left) and Thermocouple locations (right).....	26
Figure 4-1: Desorption/ Charging Process (left) and Adsorption/Discharging Process (right) [24].....	29
Figure 5-1: Axial temperature profiles at various bed depths (z) - Charging cycle 1.....	35
Figure 5-2: Humidity and Mass flow rate - Charging cycle 1.....	36
Figure 5-3: Radial temperature profiles at various bed depths (z) - Charging cycle 1.....	37
Figure 5-4: Packed bed inlet and outlet temperatures - Charging cycles 1- 3.....	38
Figure 5-5: Energy supplied (left) and energy stored (right) - Charging cycles 1- 3.....	39
Figure 5-6: The timewise cumulative percentage of energy absorbed from the total energy absorbed (left) and Percentage of energy absorbed from energy supplied (right).....	40
Figure 5-7: Axial temperature profiles at various bed depths (z) - Discharging cycle 1.....	42
Figure 5-8: Humidity and Mass flow rate - Discharging cycle 1.....	43
Figure 5-9: Radial temperature profiles at various bed depths (z) - Discharging cycle 1.....	43
Figure 5-10: Heat released - Discharging cycle 1.....	44
Figure 5-11: Packed bed inlet and outlet temperatures - Discharging cycles 1- 3.....	45

Figure 5-12: Packed bed inlet and outlet temperatures - Discharging cycles 2,4 and 5	46
Figure 5-13: Packed bed inlet and outlet temperatures - Discharging cycles 2 and 6	47
Figure 5-14: Packed bed inlet and outlet temperatures - Discharging cycles 3 and 7	48
Figure 5-15: Axial temperature profiles at various bed depths (z) - Discharging cycle 8	49
Figure 5-16: Heat released - Discharging cycle 8	49
Figure 5-17: Axial temperature profiles at various depths (z) – Charging after partial discharge.....	50
Figure 5-18: Axial temperature profiles at various depths (z) - Discharging following Charging.....	51
Figure 5-19: Kiln.....	52
Figure 5-20: Ceramic Moulds in Kiln.....	52
Figure 5-21: Butterfly Valve Temperature Control System	53
Figure 5-22: Axial temperature profiles at various bed depths (z) and inlet temperature of kiln	54
Figure 5-23: Humidity and Mass flow rate.....	54
Figure 5-24: Cumulative mass of water evaporated from ceramic casting moulds: Drying Test 1	55
Figure 5-25: kg Sample Test Section.....	56
Figure 5-26: Blower Placed in Humidity Chamber	56
Figure 5-27: Percentage of water adsorbed at different relative humidities	57
Figure 6-1: Storage Efficiencies for Cycles 1-7.....	59
Figure 6-2: Integral heat of adsorption [48].....	62
Figure 6-3: Experimental and calculated temperature increase of zeolite 13X at different humidities	64
Figure 6-4: Differential heat of adsorption [48].....	65
Figure 6-5: Experimental and calculated energy storage capacity of zeolite 13X [49]	67
Figure 6-6: Experimental and calculated water adsorption capacity of zeolite 13X [44].....	68
Figure 6-7: Block diagram of system.....	69
Figure A-1: Humidifier	79
Figure A-2: Leister LHS 61S Premium Heater.....	80
Figure A-3: Centrifugal Blower with Conical Inlet Attached.....	80
Figure A-4: ebm-papst centrifugal blower.....	80
Figure A-5: Thermocouples wired to Multiplexer.....	81
Figure A-6: Conical inlet geometry [50].....	81
Figure A-7: Conical inlet	82
Figure A-8: HTM2500LF Humidity Sensor	83
Figure A-9: Testo humidity sensor and measurement device	84
Figure A-10: Pressure transducers connected to Betz manometer.....	84
Figure A-11: Fine mesh and gasket placed on grating.....	85
Figure A-12: Reactor and Bottom Cone bolted together	85
Figure A-13: zeolite packed in reactor bed	86
Figure A-14: Insulated Reactor.....	86

Figure A-15: Full Assembly showing charging configuration	87
Figure A-16: Full Assembly showing discharging configuration.....	88
Figure B-1: Axial temperature profiles at various bed depths (z) - Charging cycle 2	89
Figure B-2: Humidity and Mass flow rate - Charging cycle 2.....	90
Figure B-3: Radial temperature profiles at various bed depths (z) - Charging cycle 2.....	90
Figure B-4: Axial temperature profiles at various bed depths (z) - Charging cycle 3	91
Figure B-5: Humidity and Mass flow rate - Charging cycle 3.....	92
Figure B-6: Radial temperature profiles at various bed depths (z) - Charging cycle 3.....	93
Figure B-7: Axial temperature profiles at various bed depths (z) - Discharging cycle 2.....	94
Figure B-8: Humidity and Mass flow rate - Discharging cycle 2	95
Figure B-9: Radial temperature profiles at various bed depths (z) - Discharging cycle 2	95
Figure B-10: Heat released - Discharging cycle 2	96
Figure B-11: Axial temperature profiles at various bed depths (z) - Discharging cycle 3.....	97
Figure B-12: Humidity and Mass flow rate - Discharging cycle 3	98
Figure B-13: Radial temperature profiles at various bed depths (z) - Discharging cycle 3	98
Figure B-14: Heat released - Discharging cycle 3	99
Figure B-15: Axial temperature profiles at various bed depths (z) - Discharging cycle 4.....	100
Figure B-16: Humidity and Mass flow rate - Discharging cycle 4	101
Figure B-17: Radial temperature profiles at various bed depths (z) - Discharging cycle 4.....	101
Figure B-18: Heat released - Discharging cycle 4	102
Figure B-19: Axial temperature profiles at various bed depths (z) - Discharging cycle 5.....	103
Figure B-20: Humidity and Mass flow rate - Discharging cycle 5	104
Figure B-21: Radial temperature profiles at various bed depths (z) - Discharging cycle 5	104
Figure B-22: Heat released - Discharging cycle 5	105
Figure B-23: Axial temperature profiles at various bed depths (z) - Discharging cycle 6.....	106
Figure B-24: Humidity and Mass flow rate - Discharging cycle 6	106
Figure B-25: Radial temperature profiles at various bed depths (z) - Discharging cycle 6.....	107
Figure B-26: Heat released - Discharging cycle 6	108
Figure B-27: Axial temperature profiles at various bed depths (z) - Discharging cycle 7.....	109
Figure B-28: Humidity and Mass flow rate - Discharging cycle 7	110
Figure B-29: Radial temperature profiles at various bed depths (z) - Discharging cycle 7	110
Figure B-30: Heat released - Discharging cycle 7	111
Figure B-31: Axial temperature profiles at various bed depths (z) - Discharging cycle 8.....	111
Figure B-32: Humidity and Mass flow rate - Discharging cycle 8	112
Figure B-33: Radial temperature profiles at various bed depths (z) - Discharging cycle 8.....	113
Figure B-34: Heat released - Discharging cycle 8	113

List of Tables

Table 2-1: Solid Media for Sensible Heat Storage [18].....	7
Table 2-2: Liquid Media for Sensible Heat Storage [19].....	7
Table 2-3: Organic PCMs and their respective properties [21]	9
Table 2-4: Inorganic and Eutectic PCMs and their respective properties [21]	10
Table 2-5: Overall energy efficiencies for different types of TES [24].....	11
Table 2-6: Classification of Pore Size [27].....	12
Table 2-7: Properties of Different types of Adsorbents for TES [6].....	13
Table 2-8: Properties of zeolite 13X beads/spheres [35]	15
Table 2-9: Change in Temperature vs Humidity [5].....	19
Table 3-1: Thermocouples at different axial and radial distances	26
Table 5-1: Charging/ regeneration cycle results	34
Table 5-2: Discharging cycle results.....	41
Table 6-1: Efficiencies from Charging and Discharging cycle results	58
Table 6-2: Overall efficiency with sensible heat included.....	60
Table 6-3: Langmuir-Freundlich model coefficients	62
Table 6-4: Comparison of calculated and experimental temperature lift.....	63
Table 6-5: Calculated and Experimental Energy Density.....	66
Table 6-6: Energy stored at different regeneration temperatures.....	66
Table 6-7: Design parameters	69
Table 6-8: Calculated system parameters	70
Table A-1: Humidity sensor wires	83
Table C-1: Data at three points in the system during charging cycle 1	114
Table C-2: Data at three points in the system during discharging cycle 1.....	116

Nomenclature

Symbols

C	Water content of zeolite [$\text{kg}_w/\text{kg}_{\text{zeolite}}$]
ΔC	Difference in the water content ratio of zeolite [$\text{kg}_w/\text{kg}_{\text{zeolite}}$]
C_{ads}	Water content of zeolite after adsorption [$\text{kg}_w/\text{kg}_{\text{zeolite}}$]
C_d	Discharge coefficient for conical inlet
C_{des}	Water content of zeolite after desorption [$\text{kg}_w/\text{kg}_{\text{zeolite}}$]
C_{eq}	Equilibrium loading of water during adsorption [$\text{kg}_w/\text{kg}_{\text{zeolite}}$]
c_{air}	Specific heat capacity of air constant pressure [$\text{J}/\text{kg}\cdot\text{K}$]
c_p	Specific heat capacity at constant pressure [$\text{J}/\text{kg}\cdot\text{K}$]
c_{pl}	Average specific heat of the liquid phase between T_m and T_f [$\text{J}/\text{kg}\cdot\text{K}$]
c_{ps}	Average specific heat of the solid phase between T_i and T_m [$\text{J}/\text{kg}\cdot\text{K}$]
$c_{\text{sorb,eff}}$	Effective heat capacity of zeolite 13X [$\text{J}/\text{kg}\cdot\text{K}$]
d_c	Conical inlet diameter [m]
f	Melt fraction
h	Enthalpy [J/kg]
ΔH_{ad}	Enthalpy change during adsorption [J]
ΔH_{ads}	Integrated differential heat of adsorption [$\text{J}/\text{kg}\cdot\text{K}$]
ΔH_{ds}	Enthalpy change during desorption [J]
ΔH_m	latent heat of fusion [J/kg]
$L(T)$	Heat of condensation/evaporation of water [kJ/kg_w]
l	Liquid phase
m	Mass [kg]
P	Pressure [Pa]
P_v	Partial pressure of water vapour [Pa]
Pr	Prandtl Number
ΔP_c	Pressure difference between conical inlet throat and ambient [Pa]
Q	Thermal energy [J]
Q_{bind}	Specific energy of binding [J]
Q_{cond}	Specific heat of condensation [J]
Q_d	Energy released during discharging [J]
Q_{in}	Energy input during the charging process [J]
Q_{loss}	Heat loss during the charging process [J]
Q_{loss}	Heat loss during the charging and discharging process

Q_{out}	Energy output during the charging process [J]
Q_s	Quantity of thermal energy stored during charging [J]
Q_{sens}	Sensible heat [J]
Re	Reynolds number
r	Radial bed coordinate [m]
s	Solid phase
T_f	Final Temperature [K]
T_i	Initial Temperature [K]
T_1	Inlet Temperature [K]
T_2	Outlet Temperature [K]
T_m	Melting Temperature [K]
ΔT	Change in Temperature [K]
t	Time [h]
U_w	Overall heat transfer coefficient [W/m^2K]
x	Humidity ratio or specific humidity [kg_w/kg_{da}]
Δx	Humidity difference between inlet and outlet or reactor [kg_w/kg_{da}]
z	axial bed coordinate [m]
η_c	Efficiency of charging process
η_d	Efficiency of discharging process
η_o	Efficiency of overall process
ρ	Density [kg/m^3]
φ	Relative Humidity

Subscripts

ads	Adsorption
amb	Ambient
da	Dry air
des	Desorption
w	Water
z	Zeolite

Abbreviations

amb	Ambient
avg	Average
max	Maximum
sys	System
temp	Temperature
wt	Weight

Acronyms

DMRE	Department of Mineral Resources and Energy
PCM	Phase change material
PLC	Programmable logic controller
RH	Relative Humidity
SA	South Africa
STP	Standard temperature and pressure
TC	Thermocouple
TCES	Thermochemical energy Storage
TCM	Thermochemical Material
TES	Thermal energy Storage
VSD	Variable Speed Drive
WHR	Waste heat recovery

1 Introduction

1.1 Background

According to the Department of Mineral Resources and Energy, the industrial sector is the largest consumer of energy in South Africa, accounting for 51 percent (refer to Figure 1-1) of final energy consumption in 2018 [1]. Approximately two-thirds of energy end-use in industry is for heat generation [2]. This arises since many industries require heat during manufacturing to transform raw materials into final products. Manufacturing processes are not always efficient and produce significant quantities of waste heat. It is estimated that between 20-50% of energy generated in industrial processes is vented to the atmosphere in the form of cooling water, heated surfaces and exhaust gases [3].

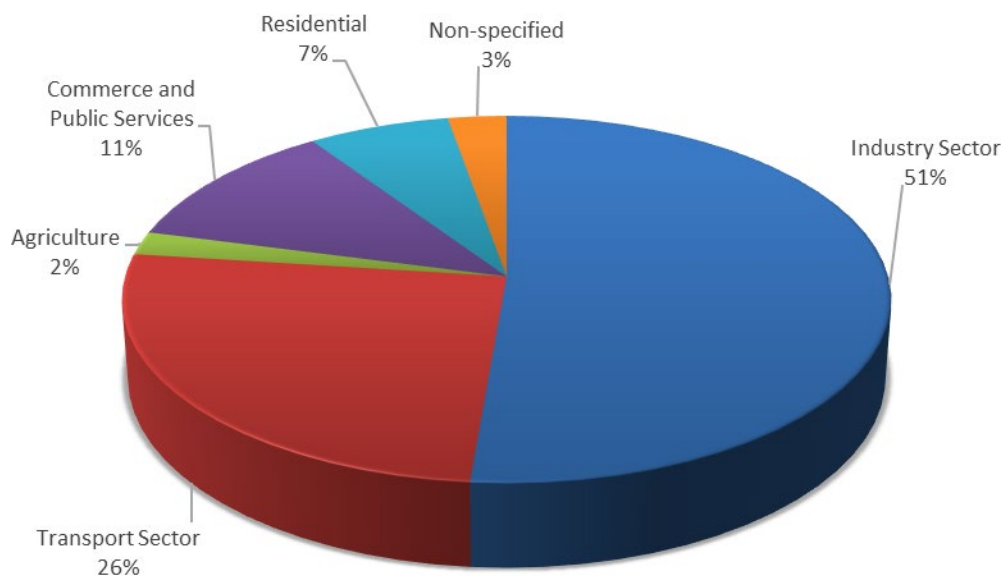


Figure 1-1: SA DMRE Energy Balances, 2018 [1]

With rising fuel prices, the prospect of fossil fuel depletion and the continuous global effort to minimise environmental impact, it is critical to recover and reuse energy wherever possible. However, supply does not always match demand especially in batch-wise processes. It is therefore necessary to develop efficient ways of storing thermal energy to ensure availability when required. The integration of thermal energy storage with waste heat recovery (WHR) technologies has the potential to provide constant heat output during periods where the supply varies. There are four critical components to a WHR system, which utilises thermal energy storage, as shown in Figure 1-2. This includes a suitable source, an efficient way to recover and then store the heat for the short/ long term, and an appropriate end-use for the recovered heat [4].

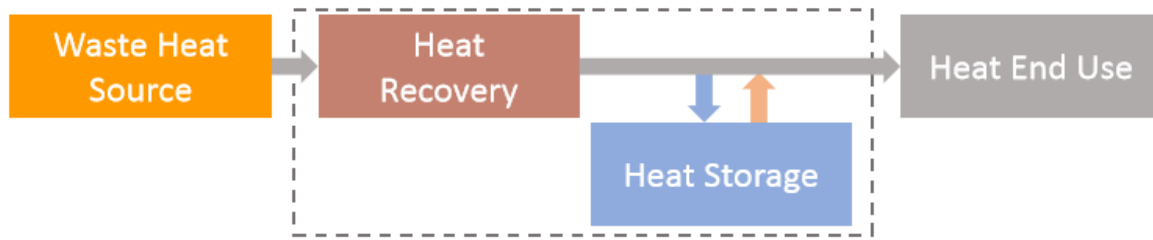


Figure 1-2: WHR System Including Thermal Storage [4]

Thermal energy can be stored in three main ways namely, sensible, latent and thermochemical heat form. Sensible heat is the simplest method to store thermal energy and depends on the temperature change, mass of storage medium and specific heat capacity of the medium. Latent heat storage systems utilise the latent heat of the phase change of the storage material. Both these methods store heat directly. In contrast, thermochemical energy storage stores heat indirectly by using physical and/or chemical reactions to store and release heat [5]. Due to this fact, thermochemical energy storage can store heat for long periods with minimal losses and achieve much higher energy storage densities compared to sensible and latent heat systems [6]. This thesis focuses on thermochemical energy storage, with zeolite 13X as the storage medium.

1.2 Applications of Thermochemical Energy Storage

In theory, thermochemical energy storage systems can store heat indefinitely. This will ensure that heat is readily available when required, especially for batch-wise processes. Thermochemical energy storage can be readily integrated into various industries to increase the efficiency of manufacturing processes. Since zeolites are suited to lower temperature applications and absorb moisture from air, they are excellent candidates for drying processes in industry [7]. Drying is energy intensive and accounts for 12-20% of the total energy consumed in the industrial sector [8]. It is used across a wide range of industries, including the ceramic, agricultural, chemical, paper and plastic sectors [9, 10]. For each kilogram of water that must be evaporated, approximately 0.63 kWh is required to overcome the latent heat of vaporisation of water [11]. Drying can be achieved by convection, conduction, radiation or microwaves [8]. Steam, natural gas, paraffin and electricity are commonly used as the energy sources for industrial dryers [12]. Many of the industrial processes in the aforementioned sectors, exhaust waste heat at high temperatures which can be recovered and reused for drying. This research was initiated to demonstrate the capability of zeolite to recover and store heat for drying applications in industry. One particular industry where batch-wise drying is required is the ceramics industry.

A typical ceramic manufacturing process is illustrated in Figure 1-3 with a detailed schematic of the slip casting process. At the beginning of the manufacturing process, raw materials such as clay and silica (in powder form) are mixed with water to create a slurry referred to as a slip. The slip is then cast in a Plaster of Paris mould. Since the mould is porous, it absorbs some water from the slip

resulting in a solid formation along the internal surface of the mould. The excess slurry is then drained, and the solid product is removed from the mould. The product is then allowed to dry completely before being sintered. During the sintering process, the product is subjected to high temperatures which removes structural water and organic binders. This adds strength and rigidity to the product. Finishing processes such as machining and glazing are then applied to achieve the final product [13].

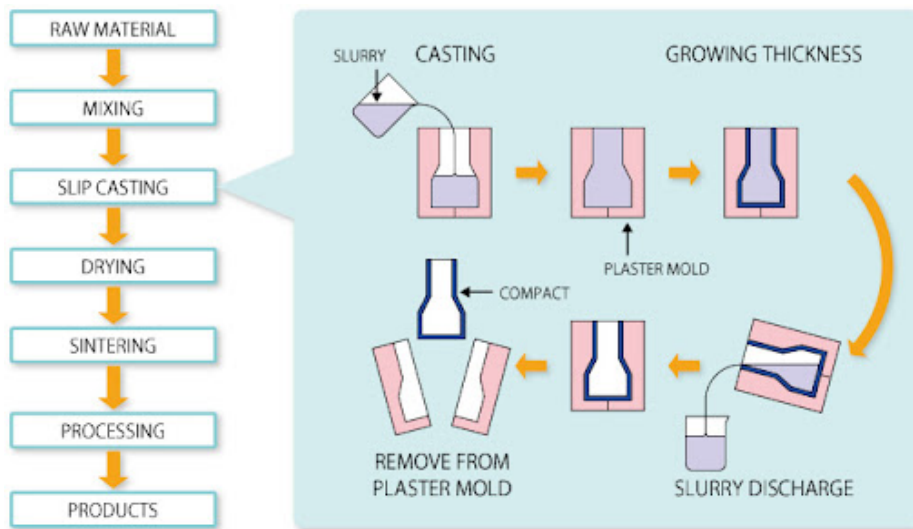


Figure 1-3: Ceramic manufacturing process [14]

In order to demonstrate the potential of zeolite 13X for waste heat recovery and drying, an industrial company was approached. The company specialises in the manufacture and supply of engineering ceramics. The company operates high temperature electric kilns for the sintering of ceramics at temperatures exceeding 1000 °C. Once a firing cycle is complete, natural convection and thereafter forced convection cooling is utilised to reduce the temperature of the kiln contents. This generates an exhaust air stream with a temperature that is initially above 800 °C, which steadily decreases over time as the contents of the high temperature kiln cool to ambient temperature. This exhaust air stream is a valuable energy source that can be utilised, however it is commonly vented to the atmosphere. During the production process the Plaster of Paris moulds (used for slip casting) are reused and therefore must be dried in order to repeat the production process. Currently the company uses electric ovens for drying the moulds which are very inefficient. The moulds are dried at temperatures of approximately 60 °C which can be easily achieved from the waste heat exhaust stream from the high temperature kilns. However, since the processes are batch-wise, the exhaust heat will not always be readily available and therefore the heat should be stored to ensure availability. The deployment of a zeolite waste heat recovery (WHR) system with integrated thermal energy storage (TES) has the potential to reduce electricity consumption and hence reduce costs and carbon emissions in the

factory. Ceramic casting moulds were supplied by the company, for preliminary drying testing, which is discussed in Section 5.4.

Thermal energy storage can also be combined with renewable energy technologies (especially solar thermal energy) to maximise efficiency of these systems. Due to the inconsistency between sunny periods and high thermal demand periods, solar systems are not very reliable. Thermal energy storage can significantly improve the performance of solar energy systems. This concept is illustrated in Figure 1-4. The system shown uses thermochemical energy storage with zeolite as the storage medium. The principle of operation is simple. On hot sunny days heat is stored in the zeolite and on cold days the heat is released for space heating [15].

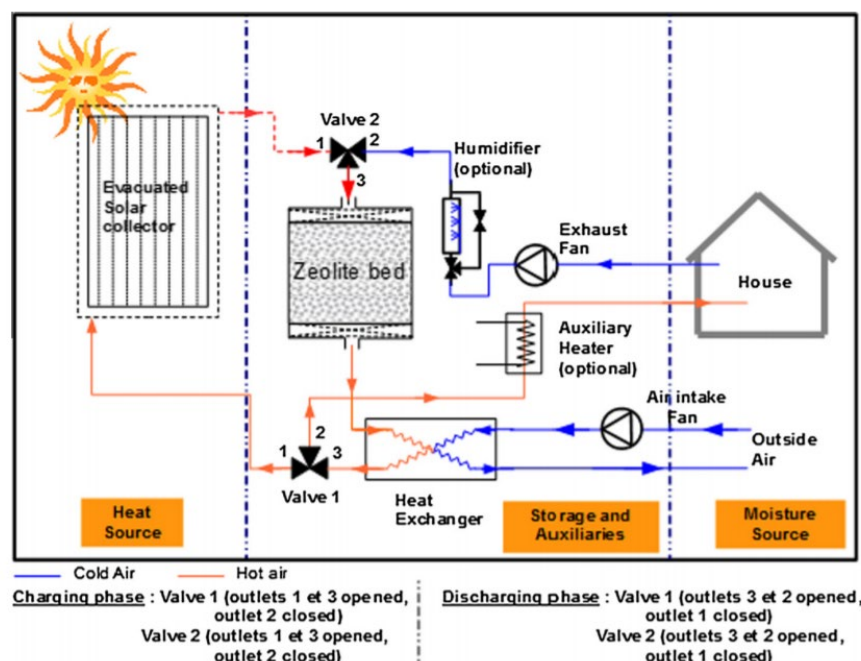


Figure 1-4: Schematic of a Solar Thermal System with Integrated Thermochemical Storage [15]

1.3 Aims and Objectives

The aim of this research was to investigate the performance of a zeolite TES for waste heat recovery and thermal energy storage in the South African industrial sector.

The objectives of this work were to:

- Conduct research on thermal storage and compile a literature review of previous studies
- Design and manufacture a lab-scale packed bed testing facility
- Setup multiple experiments to analyse the thermal characteristics of zeolite 13X
- Measure the flowrate of air through the system and the temperature and humidity at the inlet and outlet of the reactor

- Vary the humidity, flow rate and regeneration temperature to determine the impact on the performance of the system
- Test the system for drying ceramic casting moulds
- Measure the amount of water that can be adsorbed by zeolite 13X
- Determine the energy efficiency of the system
- Analyse the performance of the experimental system with theoretical calculations and/or previous studies

1.4 Thesis outline

The current chapter gives a brief overview of thermal storage and the need for thermal storage integration to improve the efficiency of current systems and reduce environmental impact. Possible applications of thermochemical heat storage are discussed, such as storing waste heat and solar energy and utilising it for industrial drying processes and space heating.

Chapter 2 discusses the different thermal storage techniques with the focus on thermochemical storage and adsorption in particular. The properties of the thermochemical material of interest (zeolite 13X) are presented and explained. Previous studies and their findings are mentioned.

Chapter 3 details the apparatus used for experimentation. This includes a detailed description of the design, apparatus and methodology used for experimentation.

Chapter 4 gives an overview of the energy balance in the system and a method of calculating the energy efficiencies of an open sorption system.

Chapter 5 presents and discusses the results from experiments. The temperature, humidity and mass flow rates measured are presented for the charging and discharging cycles. Based on the enthalpy, the energy absorbed/ released are plotted for each cycle. The experimental results from the drying tests (on ceramic casting moulds) and moisture adsorption capacity (of zeolite 13X) are also presented and discussed.

Chapter 6 analyses the performance of the experimental system by comparing the experimental results with calculated/ theoretical values and results from previous studies. The parameters that were evaluated are the energy efficiency, temperature lift, thermal coefficient of performance, energy storage capacity and moisture adsorption capacity.

Chapter 7 presents the main conclusions of the research conducted with suggestions for development and implementation in industries.

2 Literature Review

2.1 Thermal Energy Storage Technologies

Thermal energy storage is one of the fundamental technologies which can be readily integrated with existing energy systems as well as renewable energy systems to maximise efficiency. There are three primary methods of storing thermal energy which are sensible, latent and thermochemical heat storage as illustrated in Figure 2-1 [6].

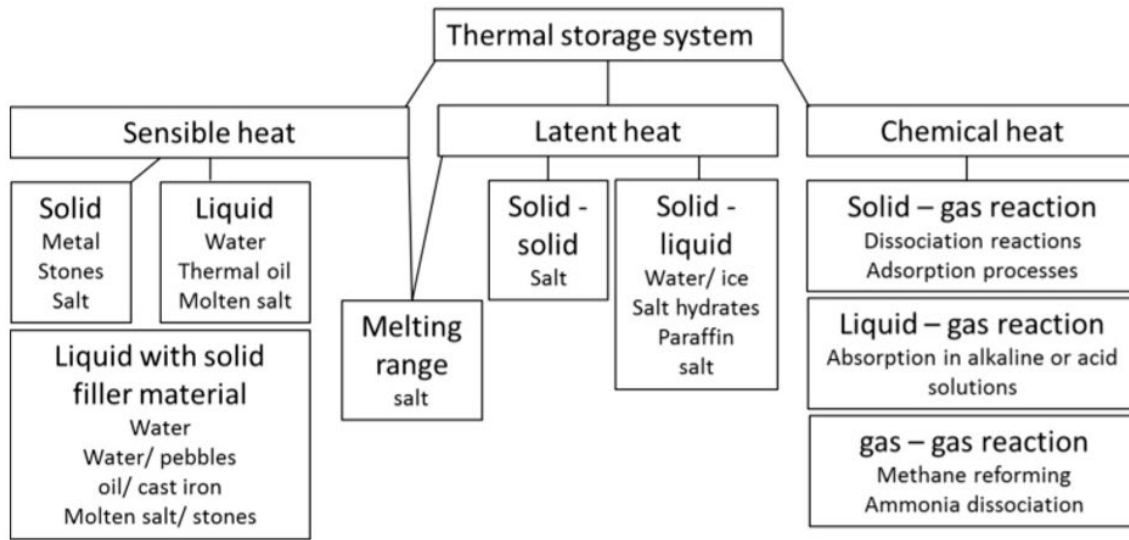


Figure 2-1: Thermal Storage Techniques [6]

2.1.1 Sensible Heat Storage

Sensible heat is the simplest way to store thermal energy and is used in a wide range of applications. Sensible heat can be separated into two categories i.e., solid media (e.g., rock, sand and metals) and liquid media (hot water storage, molten salts and oil-based fluids) [16]. Hot water storage is the most common due to the fact that water is inexpensive and has a high specific heat capacity. Many industrial and residential applications currently utilise water for heat storage. However, water can only be used for temperatures below 100 °C if a 1 bar pressure limit is prescribed. Liquid metals, molten salts and thermal oils can be used for temperatures above 100 °C [17]. Table 2-1 and Table 2-2 summarise a variety of different types of sensible heat materials and their respective properties.

Table 2-1: Solid Media for Sensible Heat Storage [18]

Medium	Working temperature (°C)	Density (kg/m³)	Thermal conductivity (W/m.K)	Specific heat (J/kg.K)
Sand-rock minerals	200-300	1700	1.0	1300
Reinforced concrete	200-400	2200	1.5	850
Cast iron	200-400	7200	37.0	560
NaCl	200-500	2160	7.0	850
Cast steel	200-700	7800	40.0	600
Silica fire bricks	200-700	1820	1.5	1000
Magnesia fire bricks	200-1200	3000	5.0	1150
Dry bricks	200-800	1800	0.5	840
Soil (gravelly)	-	2040	0.59	1840
Soil (clay)	-	1450	1.28	880

Table 2-2: Liquid Media for Sensible Heat Storage [19]

Medium	Working Temperature (°C)	Density (kg/m³)	Thermal Conductivity (W/m.K)	Specific Heat (J/kg.K)
Water	0 to 100	1000	0.63 at 38 °C	4190
Water-Ethylene Glycol 50/50	-	1050	-	3470
Caloria HT43	-10 to 315	-	-	2300
Dowtherms	12 to 260	867	0.112 at 260 °C	2200
Therminol 55	-18 to 315	-	-	2400
Therminol 66	-9 to 343	750	0.106 at 343 °C	2100
Ethylene Glycol	-	1116	0.249 at 20 °C	2382
Hitec	141 to 540	1680	0.61	1560
Engine oil	Up to 160	888	0.145	1880
Draw salt	220 to 540	1733	0.57	1550
Lithium	180 to 1300	510	38.1	4190
Sodium	100 to 760	960	67.5	1300
Ethanol	Up to 78	790	-	2400
Propanol	Up to 97	800	-	2500
Butanol	Up to 118	809	-	2400
Isobuthanol	Up to 100	808	-	3000
Isopentanol	Up to 148	831	-	2200
Octane	Up to 126	704	-	2400

The quantity of heat stored in sensible heat storage system depends on temperature change, heat capacity of the storage medium and the mass of the material and can be calculated as follows [17]:

$$Q_s = \int_{T_i}^{T_f} mc_p dT \quad (2-1)$$

Although sensible heat storage systems are economical and easy to implement, they provide low energy densities and hence require very large storage volumes. If the heat is to be stored for a long period of time, costly insulation is required to minimise heat losses to the environment. Due to these factors sensible heat storage may not always be the most efficient method for thermal storage, especially when low temperature change and long-term heat storage is required [16].

2.1.2 Latent Heat Storage

Latent heat is stored or released from a system when the storage material, known as a phase change material (PCM), melts or solidifies. PCMs initially behave like sensible heat material until the phase transition temperature. During the phase change the chemical bonds break, allowing the PCM to absorb large amounts of energy at a constant temperature as shown in Figure 2-2 [20].

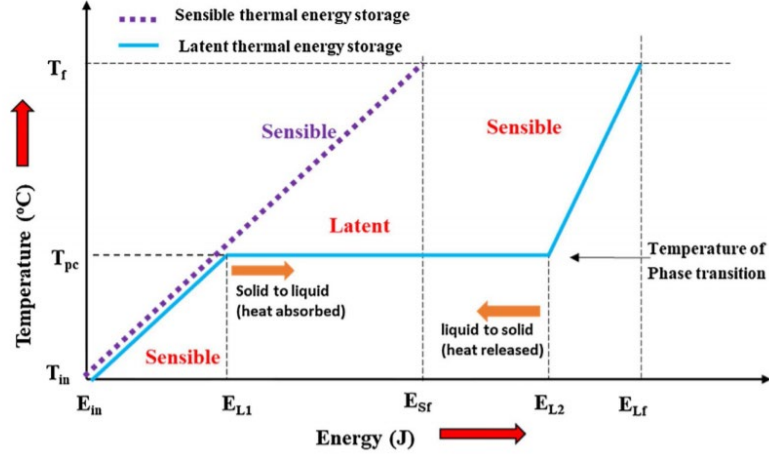


Figure 2-2: Phase transition profile of PCM [20]

The amount of heat that can be stored in a latent heat storage system is given as [17]:

$$Q_s = \int_{T_i}^{T_m} mc_p dT + mf\Delta H_m + \int_{T_m}^{T_f} mc_p dT \quad (2-2)$$

There are three components to the equations above. The first component comprises of the sensible heat storage in the solid phase, the second component depicts the latent heat of fusion, and the last part of the equation describes the sensible heat stored in the liquid phase [20].

Phase change materials can be classified as organic, inorganic or eutectic [21]. Water is one of the most common materials for latent heat storage, at low temperatures, due to its high latent heat of fusion [16]. Other common PCMs and their properties are presented in Table 2-3 and Table 2-4 [21].

PCMs can be encapsulated to support the material and limit interaction with the external environment. It also increases the heat transfer area and prevents leakage. There are two main ways to encapsulate the PCM, which are macro-encapsulation and micro-encapsulation. Macro-encapsulation involves containing the PCM in structures such as tubes or shell. It is easy to implement, however, it is not very efficient in terms of heat transfer and may be susceptible to leaks. Micro-encapsulation is the preferred method and involves coating the PCM with a thin film of impervious material [21].

Latent heat storage systems have the potential to provide higher energy storage densities than sensible heat storage systems in the order 5-14 times more [16]. This is due to high enthalpy change during the phase transition. However, it may be difficult to contain the PCM within the system. The resulting pressure increase if vapour forms is one concern. In addition, there could be chemical instability of the PCM, and high costs involved with the design and implementation of latent heat storage systems [16].

Table 2-3: Organic PCMs and their respective properties [21]

Material	Melting point (°C)	Latent heat storage (kJ/kg)	Sensible heat storage (kJ/kg)	Thermal conductivity (W/m.K)	Density (kg/m ³)
Organic PCM					
Stearic acid	64.5	196	2.27[l], 1.76[s]	1.60[s]	940
Palmitic acid	61-63	204-212	2.20 [40 °C]	0.162 [68.4 °C, l]	942
Polyethylene glycol [PEG]/ silicon dioxide [SiO ₂] composite	60	179	-	-	-
Polyurethane Polymer	29.8	191	-	-	-
Paraffin wax	54	184	-	-	-
Malic acid	51.5-53.6	190-204.5	-	0.17[s]	860
RT5	7	158.3	-	-	-
Capric acid	31.3-31.6	163	-	0.16[s]	878[l], 1004[s]
Lauric acid	41-44	183-212	1.76 [25 °C]	0.16[s]	862
Erythritol	118	339.8	2.61[l], 2.25[s]	0.326[l], 0.733[s]	1480[s], 1300[l]
Hydroquinone	168-173	205	-	-	-
Acetamide	82	263	-	-	1159
Acetanilide	118	222	1.94	-	-
Dimethyl Sulphoxide	16.5	85.7	-	-	1009[l]
Hexadecane	18.1	236	-	-	770 [20 °C]
Polyglycol E 600	12.5	129.1	2.22 [l]	0.189 [38.6 °C, l] 0.187 [67 °C, l]	1126 [25 °C, l] 1232 [4 °C, s]

Table 2-4: Inorganic and Eutectic PCMs and their respective properties [21]

Material	Melting point (°C)	Latent heat storage (kJ/kg)	Sensible heat storage (kJ/kg)	Thermal conductivity (W/m.K)	Density (kg/m³)
Inorganic PCM					
Na ₂ CO ₃ – 10H ₂ O	33-36	247	-	-	1485
CaCl ₂ – 6H ₂ O	30	170-192	-	1.08[s], 0.56[l]	1710
Na ₂ SO ₄ – 10H ₂ O	32	251	1.4[s], 2.1[l]	0.15[l], 0.3[s]	1464
MgCl ₂ – 6H ₂ O	117	168.6	2.61[l], 2.25[s]	0.570 [120 °C, l] 0.694 [90 °C, s]	1450 [120 °C, l] 1569 [20 °C, s]
Na ₂ HPO ₄ – 12H ₂ O	35-45	279.6	-	0.476[l], 0.514[s]	1520
Manganese [II] Nitrate Hexahydrate	89.3-89.9	167-175	-	0.57 [120 °C]	-
K – 4H ₂ O	18.5	231	1.84 [s], 239 [l]	-	-
Mg [NO ₃] ₂ .6H ₂ O	80	150	-	-	-
Eutectic					
Palmitic acid [64.2%] + stearic acid [35.8%]	52.3	182	-	-	-
Lauric acid [75.5%] + stearic acid [24.5%]	37	183	-	-	-
Capric lauric acid	18-19	120	-	-	-
Paraffins	-	-	-	-	-
Capric acid-Palmitic acid	22.5	173	2.0[s], 2.3[l]	0.14	870[s], 790[l]

2.1.3 Thermochemical Energy Storage

Thermochemical energy storage (TCES) comprises of sorption processes (i.e., adsorption and absorption) and chemical reactions [22]. The principle of operation is based on reversible chemical reactions in contrast to sensible and latent heat storage which store heat only as a function of temperature difference. During the charging process heat is required (endothermic reaction) to separate the product (AB as shown in Equation 2-4) into separate reactants. During discharging, the reactants A and B are brought together, resulting in the formation of AB and heat is liberated (exothermic reaction) [23].



Theoretically TCES is able to achieve significantly higher energy storage densities compared to sensible and latent heat storage systems (refer to Figure 2-3). According to [22], sorption systems will occupy approximately one-third of the volume that would be required for a sensible heat storage system when using water as the storage medium. Chemical reactions are able to achieve even higher storage densities than sorption systems. However, they may require a catalyst for the reaction to

proceed [16]. Table 2-5 compares the overall energy efficiencies of the different types of thermal storage techniques. From Figure 2-3 and Table 2-5, it can be deduced that TCES systems can achieve similar performance as sensible and latent heat storage systems but are more compact. The focus of this research was on adsorption based TCES.

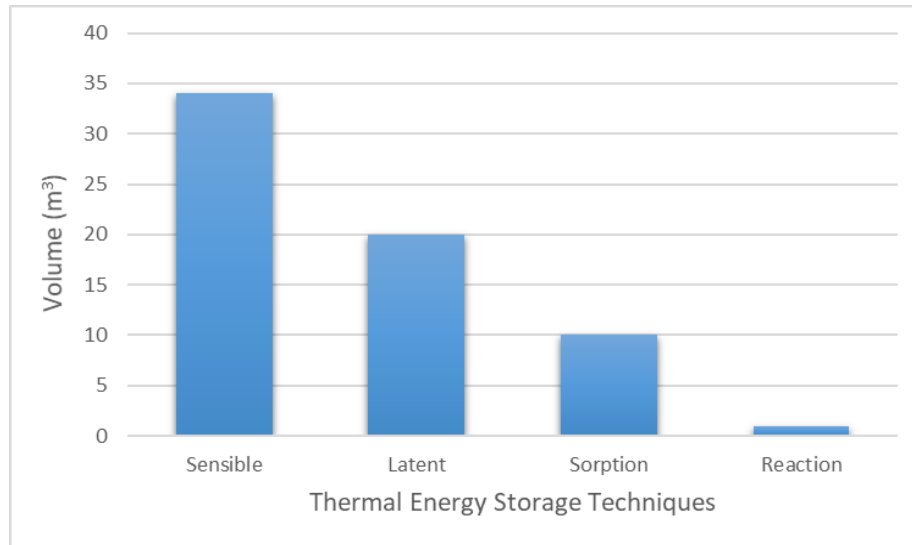


Figure 2-3: Volume required to store energy to meet the annual needs of an average household [22]

Table 2-5: Overall energy efficiencies for different types of TES [24]

TES Type	System Type	Overall efficiency (%)	Medium
Sensible	-	70	Aquifer TES
Latent	-	50	CaCl ₂ ·6H ₂ O as PCM
Thermochemical	Open TCES	69	Zeolite 13X as TCM
	Closed TCES	50	SrBr ₂ ·6H ₂ O as TCM

2.2 Adsorption

Adsorption refers to the attachment of a gas or liquid molecules to the surface of a solid [25]. The substance that is adsorbed by the adsorbent is called the adsorbate. The adsorbate is trapped by the adsorbent (solid) and diffuses into the pores of the adsorbent where it is adsorbed, and energy is released (refer to Figure 2-4). Once the adsorbent is completely saturated, no further energy is released and regeneration/desorption of the adsorbent is required which removes the adsorbate from the adsorbent. This is achieved by supplying heat to the adsorbent which is greater than the heat of vaporisation/ condensation of the adsorbate [22]. Regeneration can also be achieved by reducing the pressure in the reactor. When regeneration is complete, the adsorption process can be repeated [25].

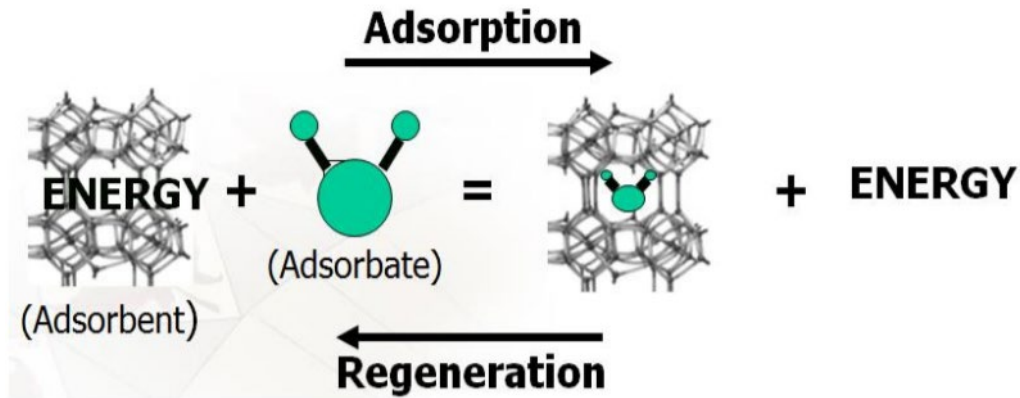


Figure 2-4: Graphic Representation Adsorption and Desorption Process [25]

Adsorption can be either physical (physisorption) or chemical (chemisorption). Physisorption occurs due to Van der Waals forces and could also include electrostatic forces. Chemisorption involves valence electrons which leads to the formation of a new chemical compound. This is due to a chemical bond which forms between the adsorbent and adsorbate by transferring and sharing electrons at the outer layer of the adsorbent. Physisorption has lower heats of adsorption than chemisorption. However, physisorption is reversible which is not always possible with chemisorption [26].

Adsorbent materials are porous in nature which results in a very large surface area. This enables the material to store large quantities of energy. Adsorbents can be categorised according to their pore size, pore volume and surface area. Categorisation according to pore size is presented in Table 2-6 [27].

Table 2-6: Classification of Pore Size [27]

Classification	Pore Size
Micropores	≤ 2 nm
Mesopores	2-50 nm
Macropores	> 50 nm

The adsorbent material is the main component of the energy storage system. Some of the desirable characteristics of the material include [28]:

- High energy storage capacity
- Low regeneration/desorption temperature
- Thermal stability during operation
- High uptake of adsorbate
- Suitable heat and mass transfer properties to obtain power output required
- Non-toxic – safe to handle
- Economical

Common adsorbents include silica gel, activated carbon, aluminophosphates, metal organic frameworks (MOFs) and zeolites [27, 29]. The typical properties of these adsorbents are summarised in Table 2-7 [6]. Silica gel has large surface areas ranging from 600 m²/g to 800 m²/g and can be regenerated at temperatures as low as 120 °C. However, it has a low heat of adsorption which limits its application as a heat storage medium [30]. Activated carbon is widely used in industrial processes to purify gas. However, due to its low affinity for water vapour, it is not widely used for heat storage [30]. Aluminophosphates and MOFs provide good water uptake and high energy densities (at 0.86 and 1.6 GJ/m³ respectively) but have low adsorption temperatures (30–40 °C) and are relatively expensive [31]. Previous studies show that zeolites are good candidates for heat storage [30, 31]. More information on zeolites will be provided in the next section.

Table 2-7: Properties of Different types of Adsorbents for TES [6]

Adsorbent	Adsorption heat (kJ/kg)	Typical desorption temp. (°C)	Density (kg/m³)	Specific heat (kJ/kg.K)	Thermal conductivity (W/m.K)	Uptake of adsorbate (g/g)
Silica Gels	160-180	50-80	650-700	0.8-0.9	0.15-0.20	0.03-0.10
Activated Carbons	45-900	80-200	700-750	0.8-1.5	0.15-0.75	0.15-0.60
ALPO ₈ /SAPO ₅	250-300	60-90	800-900	0.85-0.95	0.15-0.25	Up to 0.25
MOFs	20-200	60-150	1000-2000	0.8-1.2	0.10-0.15	0.16-0.40
Zeolites	50-300	70-350	650-900	0.85-0.95	0.15-0.25	Up to 0.2

2.3 Adsorbents: Zeolite

Zeolites are microporous and primarily contain aluminium, silicon and oxygen atoms. They have large surface areas ranging from 800 to 1000 m²/g (1 g occupies approximately 1.64 ml) which makes them excellent materials for adsorption processes. The pore size of zeolites ranges from 3-10 angstroms. They have the ability to adsorb polar/ nonpolar molecules under suitable conditions. Water vapour can be adsorbed with a high heat of adsorption even at low concentrations [26].

There are over 40 types of naturally occurring zeolites and more than 150 types of synthesized zeolites. zeolites contain at least one silicon atom for every aluminium atom and they occur as hydrates. zeolites have a three-dimensional crystalline structure which is formed from a framework of (SiO₄) and (AlO₄) tetrahedra linked together. This can be referred to as the primary building blocks of zeolite and is illustrated in Figure 2-5. These tetrahedra link to each other resulting in the formation of cages/rings which can be referred to as the secondary building blocks (refer to Figure 2-6). The secondary building blocks link to each other which leads to the formation of the final structure [26].

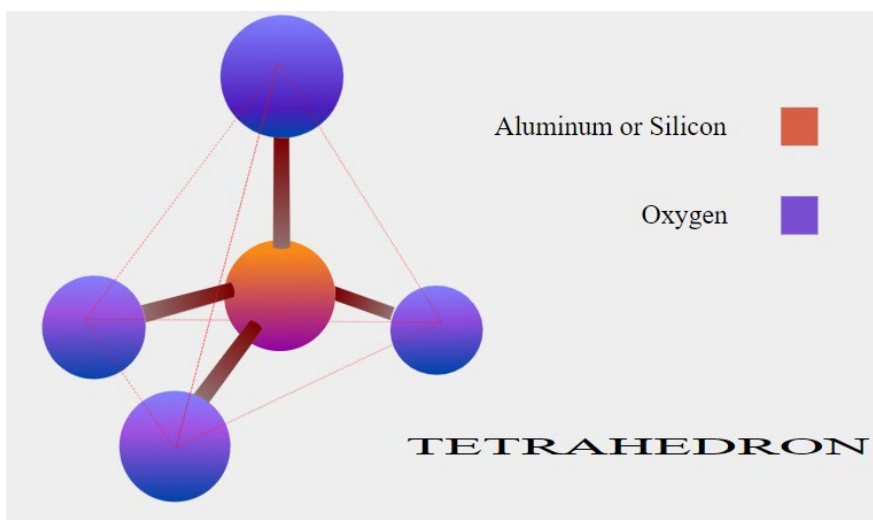


Figure 2-5: Primary Building Blocks of zeolite [32]

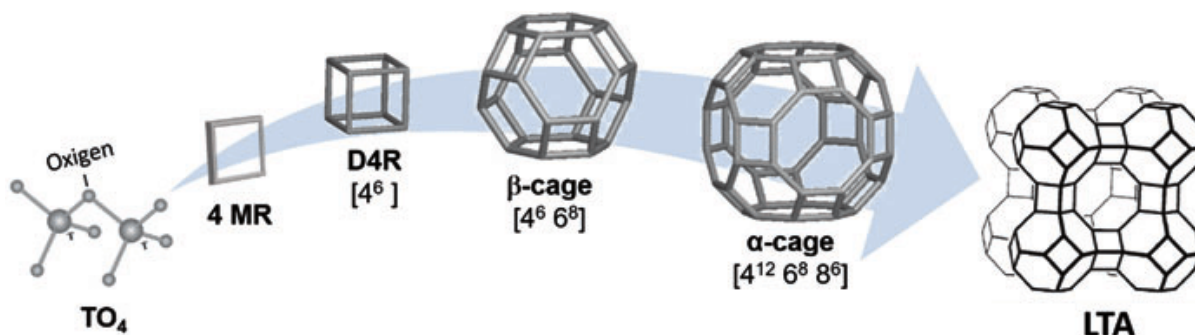


Figure 2-6: Secondary Building Blocks of zeolite [33]

Synthetic zeolites generally exhibit better properties than natural zeolites for heat storage [30]. Common synthetic zeolites are type A, X and Y. Type X and Y zeolites have larger pores than type A and therefore have better mass transfer characteristics than type A [30]. Between type X and Y, X has a stronger affinity for water vapour than type Y [30]. The type of zeolite used in this research is zeolite 13X. It has fast adsorption kinetics and high water uptake as reported by [5, 22]. The pore size is approximately 9 angstroms which enables the adsorption of molecules with critical diameters of up to 8 angstroms. It therefore has a very strong affinity for water molecules which was the adsorbate used in the experiments conducted. Water is one of the most common adsorbates since it is safe to use and readily available [30]. It is important to note that zeolite 13X becomes hydrothermally unstable at temperatures above 200 °C [5, 34]. Additional properties of the zeolite 13X (used for experiments) are summarised in Table 2-8 [35].

Table 2-8: Properties of zeolite 13X beads/spheres [35]

Property	Value
Supplier	Zantech
Diameter (mm)	3-5
Bulk Density (kg/m ³)	≥610
Crush Strength (N)	≥60
Static Water Absorption (wt%)	28.5
Attrition (wt%)	≤0.1

2.4 Open and Closed Adsorption Systems

Adsorption TCES systems can be categorized as open or closed systems (refer to Figure 2-7). An open system is in contact with the surrounding environment and therefore operates under atmospheric pressure. This means that the adsorbate, which is water vapour in most instances, is extracted from ambient air for adsorption and exhausted to the atmosphere during desorption. However, in a closed TCES the adsorbate flows in a hermetically closed loop which is usually under negative pressure. The evaporation and condensation of the adsorbate must be controlled by special devices, and an additional storage tank is required.

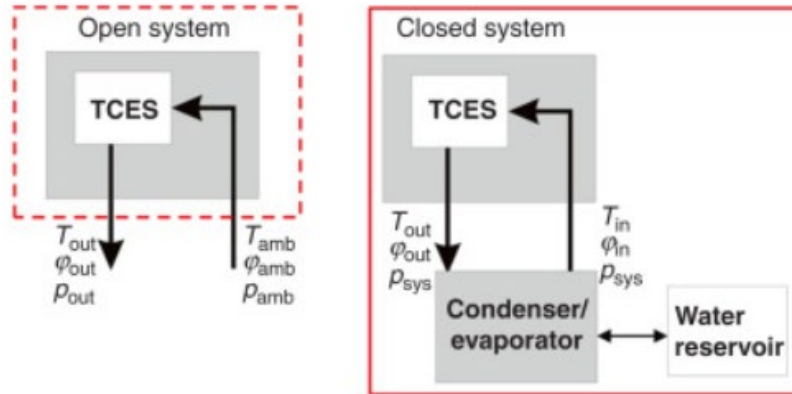


Figure 2-7: Schematic of Open and Closed Adsorption System [36]

With respect to design, the open system is much simpler since it does not require a condenser, evaporator and reservoir. Furthermore, it operates at ambient pressure and the process control is simpler [36]. This leads to lower cost involved in the manufacture of open systems. Since open systems are more practical to implement [22], the focus of this research was on open sorption systems.

2.5 Existing Studies and Systems Utilising Zeolite for Adsorption

2.5.1 ZAE Bayern

One of the earliest prototypes was developed by ZAE Bayern in Munich in 1997. The system uses zeolite 13X/water as the adsorbent/adsorbate pair. It was designed to provide heat to a school in winter and cooling to a nightclub in summer. The amount of energy required by the school was 130 kW while the club required 50 kW. Figure 2-8 illustrates the charging and discharging modes of the system. During peak demand periods (i.e., during the day) the heat was discharged and during low demand periods the 7-ton zeolite bed was charged by extracting heat, from steam generated by the district heating system, which is in the order of 130-180 °C [37].

During the cooling of the club, the air was dehumidified (i.e., latent cooling) and the system was able to lower the air temperature by approximately 4 °C at the club. A discharge temperature of approximately 80 °C during cooling showed the best system performance. It was estimated that it would take 7-8 years to payback the cost of the system installation. This was based on the assumption that the system generates 40% and 60% reduction in cost during winter and summer respectively and a minimum of 100 yearly heating and cooling cycles are run [31].

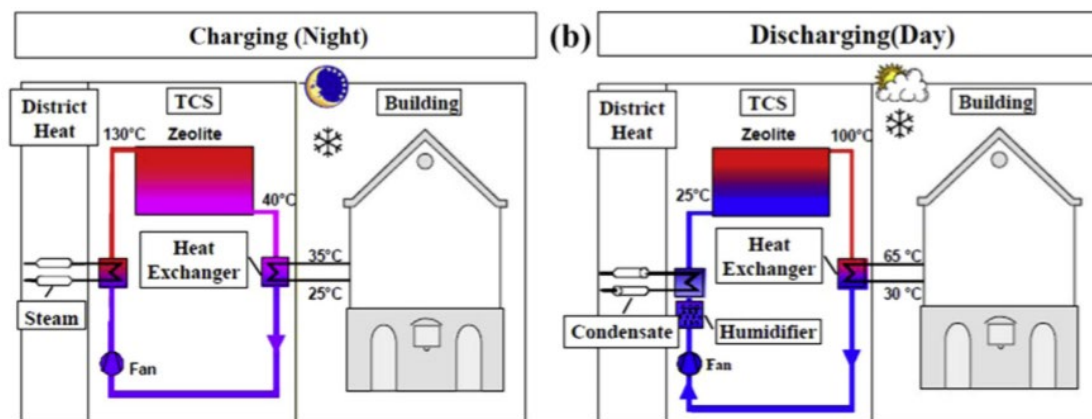


Figure 2-8: Charging / discharging modes of TCES developed in Munich [37]

2.5.2 Diponegoro University/ Wageningen University

An experiment was conducted by Djaeni et al [38] to investigate the energy efficiency for a single-stage dryer using zeolite to dehumidify and heat the air for drying. The experimental setup is illustrated in Figure 2-9. The system consists of a fan and two columns packed with 2.5 kg of zeolite. The columns (A & B) are 0.15 m (ID) and 0.4 m in height. 4 three-way (V1 – V4) valves are utilised simultaneously to change the function of the columns i.e., the columns either act as adsorber or regenerator. All pipes in the system have a 0.05 m internal diameter and the pipe and columns are insulated with insulation wool of 0.03 m thickness. The type of synthetic zeolite used was 4A also referred to as siliporite 4A. It has an adsorption capacity of up to 0.22 kg_w/kg_{zeolite}. An electric heater

(HE01) is used for regeneration. A non-insulated buffer (B01) is used to equalise temperature differences when alternating between adsorber and regenerator function. An additional heater (HE02) is placed before the drying tray (D01) to obtain the temperature required to dry the wet products. Sponges were used for the purposes of this experiment [38].

Ambient air is passed through the pipes by means of a fan. The air is separated into 2 streams which is then supplied to the adsorber and regenerator. During the adsorption process, heat is released therefore the air leaving the adsorber is at a higher temperature than the air entering. The air then passes through the HE02 for further heating and thereafter it enters D01 for the drying process. HE01 is used to heat the air above 110 °C for regeneration. The hot air entering the regenerator, causes the water to evaporate from the saturated zeolite which results in a temperature drop across the regenerator. The air from the regenerator is then released and the heat recovery potential is determined from the temperature of the exhaust gas. The process is then switched and hence the adsorber becomes the regenerator and vice versa. Thermocouples (TH1-TH5), humidity sensors (T-RH1 – T-RH3) and air velocity sensors (F1 and F2) were used to measure the temperature, humidity and flow rates respectively. VF1 and VF2 are regulating valves to control the flow rate through the system [38].

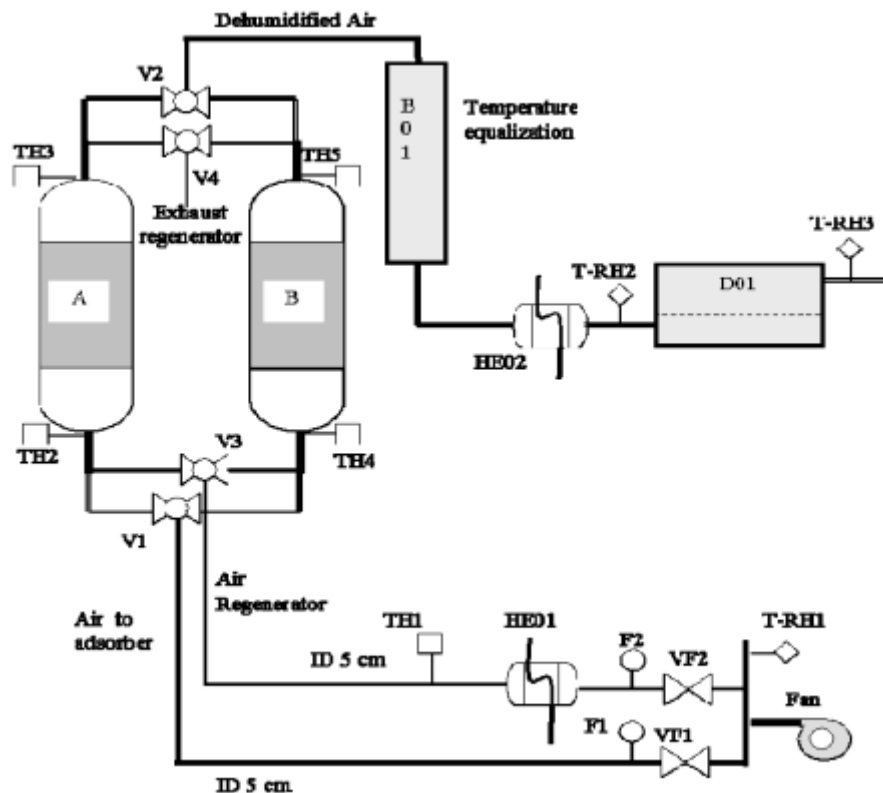


Figure 2-9: Experimental set-up of zeolite-dryer rig [38]

The main conclusions from the study were as follows [38]:

- The saturation time for zeolite is shorter when air is supplied at higher humidity. However, the total amount of energy released is the same hence the inlet humidity has little impact on the energy efficiency of the system.
- The system yielded overall energy efficiencies between 50-55% which is approximately 20% higher than a conventional dryer.

2.5.3 University of Stuttgart

The adsorption kinetics of zeolites were investigated by Mette et al [5]. A packed bed reactor, with a height of 140 mm and a diameter of 50 mm, was designed and developed (refer to Figure 2-10). The central part of the reactor was packed with zeolite 13X beads. The temperature was measured by thermocouples across the radius in four different axial positions.

A digital mass flow controller was used to measure and control the mass flow rate of the air. A humidifier was utilised to ensure that the required adsorption humidity was attained. An electrically heated pipe was used to obtain the desired temperature. Dew point sensors were placed at the inlet and outlet of the reactor to measure the humidity of the air whilst the reactor was insulated with mineral wool to minimise losses to the surroundings. The desorption process involved the use of electrical heating cables connected to the reactor wall which ensures uniform temperature distribution [5].

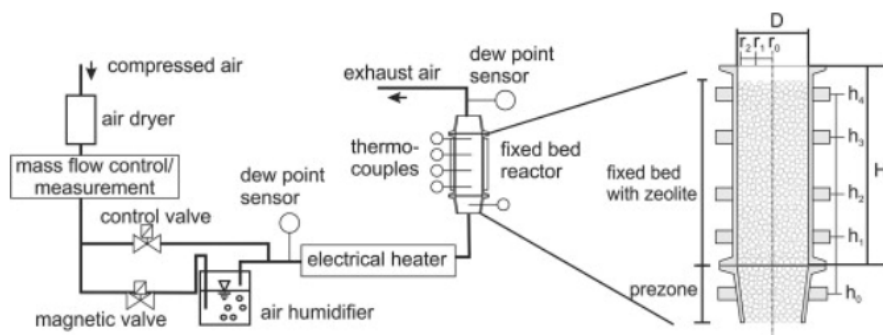


Figure 2-10: Test Rig [5]

The main conclusions that were made from the study are as follows [5]:

- Since the porosity is higher in the wall regions, the adsorption process occurs much faster.
- The heat transfer coefficient calculated was $h_R=1.4 \text{ W}/(\text{m}^2\text{K})$. There was a strong correlation between this value and the thermal conductivity of the zeolite.
- The temperature lift across the reactor was a significant function of the humidity of the airflow. The results are summarised in Table 2-9.

Table 2-9: Change in Temperature vs Humidity [5]

Humidity (g_w/kg_{da})	Change in Temperature (K)
3.1	11
9.5	38
19.2	78

2.5.4 University of Savoy Mont Blanc

Tatsidjodoung et al [15] investigated the potential of zeolite 13X for providing thermal energy for space heating an average sized house. The system developed can deliver approximately 2 kW of thermal energy at an air flow rate of 180 m³/h. The temperature of the air entering the reactor was 20 °C with a specific humidity of 10 g_w/kg_{da}. The test rig consists of two vessels of 0.14 m³ containing 2 mm (diameter) zeolite particles. To enable testing under different conditions, three different operating modes were investigated. These modes were controlled by valves as shown in Figure 2-11 [15]:

- One vessel: e.g., M1 where V1, V2 and V5 are open while the rest are closed.
- Series configuration: V3 and V5 are closed and the rest are open.
- Parallel configuration: V4 is closed and the rest are open.

The upstream and downstream temperatures of each vessel was monitored using K-type thermocouples and the pressure was measured by differential pressure sensors. Ultrasonic flow meters were used to measure the flow rate through the system. The humidity of the airflow was measured by a chilled mirror hygrometer [15].

During the 8-hour discharging cycle, the average temperature increase across the reactor was 38 °C. There was a strong correlation between temperature increase and the specific humidity of the inlet airflow. Furthermore, temperatures in the range 120–180°C were adequate to regenerate the zeolite [15].

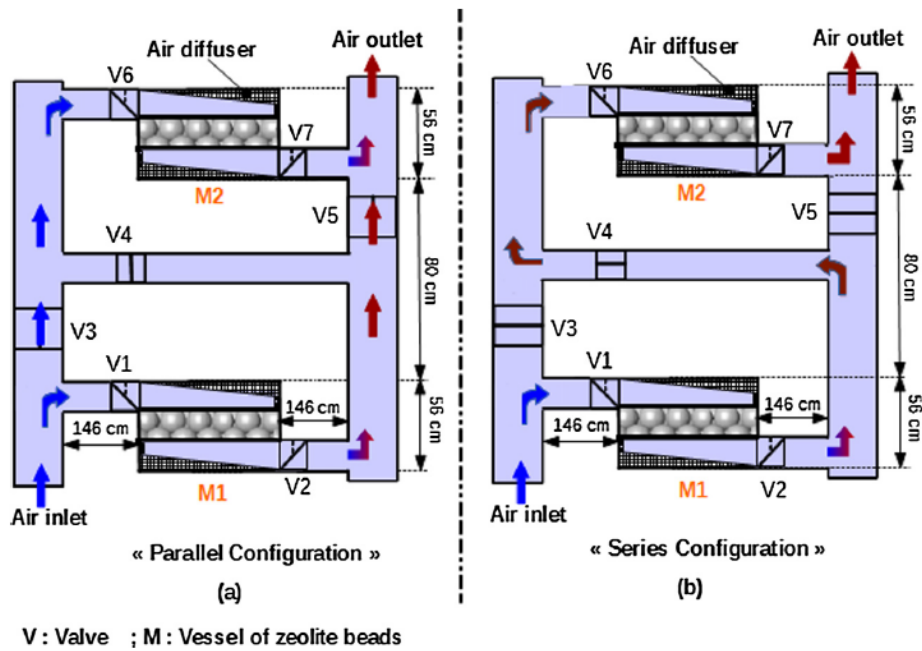


Figure 2-11: Schematic of test bed [15]

2.5.5 ZAE Bayern: Mobile Storage

ZAE Bayern developed two mobile sorption thermal storage systems with a mass of 14 tons [31]. The storages of zeolite 13X were regenerated at a temperature of 130 °C utilising ‘waste heat from an incineration plant’ turbine, by means of a steam/air heat exchanger [31]. The storages were then transported for approximately 7 km to another industry (Refer to Figure 2-12) to be utilised for a drying process. The air exiting the drying chamber (at a temperature of 60 °C and a humidity of 90 g_w/kg_{da}) was supplied to the inlet of the zeolite reactor. An outlet temperature of approximately 160 °C (i.e., a temperature lift of 100 °C) was achieved at the outlet of the zeolite reactor and returned to the drying chamber. The energy storage capacity measured was 2.3 MWh for 14 tons, which equates to 0.6 MJ/kg dry zeolite. According to calculations, the CO₂ production was reduced by 616 kg for each drying cycle. It should be noted that after 99 cycles, no material degradation as a result of mechanical stresses was observed [39].



Figure 2-12: Mobile Sorption reactors [31]

2.5.6 Eindhoven University of Technology

Gaeini et al [40] developed a system to validate a numerical model. The reactor contains 2 mm zeolite beads and is 0.1 m in height and 0.07 m in diameter. The system is divided into three stages as shown in Figure 2-13. The first section controls the humidity and flow rate of the air. This was done by a GFC (Gas Flow Controller) and a Controlled Evaporator Mixer (CEM). For hydration, the air passed through the CEM where it mixes with water supplied from the water vessel which was controlled by the Liquid Flow Controller (LFC). For the dehydration process, dry air passed through a heater and was then fed to the reactor. At the start of the experiment, time was required for system stabilisation. During this time, the airflow was released to the atmosphere via a blow-off pipe [40].

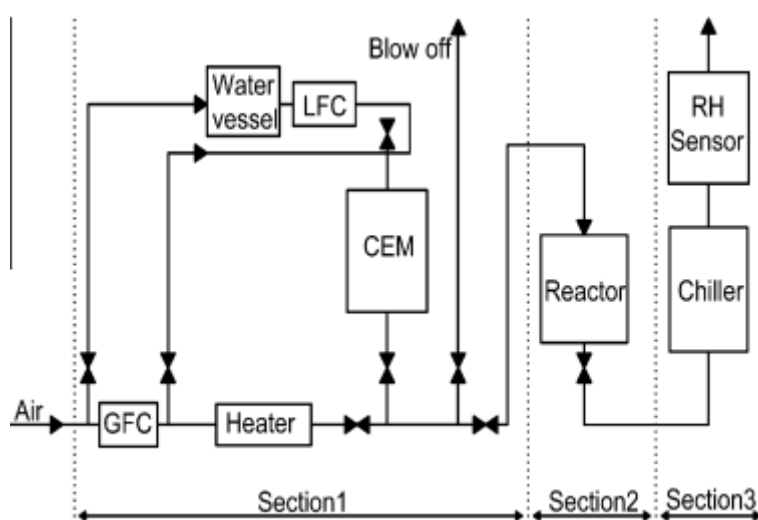


Figure 2-13: Schematic view of system and reactor

The second section contains the packed bed reactor. The outer body of the reactor was manufactured from stainless steel while the inner was made from Teflon due to its low thermal conductivity. In the third section, the temperature and relative humidity is measured at the outlet of the system. Based on the measurements obtained from the temperature and RH sensor, the absolute humidity can be determined. Since significant errors can occur when calculating absolute humidity from RH at temperatures above 100 °C, the sensors are positioned after a chiller.

The temperature increase across the reactor was approximately 18 °C during hydration/ discharging. The inlet temperature was 14 °C with a relative humidity of 25% (approximately 2.46 g_w/kg_{da}). The flow rate of air through the system was 1 l/s (4.41 kg/h) and the time taken for adsorption was approximately 5 hours.

The kinetics coefficient was determined from the thermodynamics correction factor. The impact of the kinetics coefficient on the efficiency of a large-scale system was investigated. From the numerical model it was deduced that a lower adsorption rate reduces the power and the efficiency of the reactor. However, this was only noticeable at lower values of the kinetics coefficient. It was also discovered that there is an optimal flow rate for different reactor sizes [41].

2.6 Conclusion

This section details the three main thermal storage technologies with focus on thermochemical energy storage systems. Thermochemical energy storage systems theoretically provide much higher energy storage densities compared to sensible and latent heat storage systems. The process of adsorption was explained and different types of adsorbents were discussed. The reason for choosing zeolite 13X over other adsorbents is because of its fast adsorption kinetics and high water uptake [5, 22]. Furthermore, zeolite 13X has a strong affinity for water molecules, water vapour was the adsorbate used in the experiments conducted. In addition, water is safe to use and readily available [30]. It was discovered that zeolite 13X becomes hydrothermally unstable at temperatures above 200 °C [5, 34]. The maximum regeneration temperature was therefore limited to 200 °C during experimentation.

The principle of operation of open and closed adsorption systems was discussed. Open systems are less complex than closed systems and are more efficient according to calculations done by [24]. Finally previous studies utilising zeolite as the TCM were provided. From the previous studies it was determined that the main factors, that affect the adsorption process, are humidity, mass flow rate and regeneration temperature. Therefore, these parameters were chosen to be varied during experimentation to determine the impact made on the system performance in South African climatic conditions.

3 Experimental Design, Apparatus, and Method

A packed bed testing facility was developed at the CSIR's Thermal Laboratory to analyse zeolite 13X for thermal storage under South African environmental conditions. Zeolite 13X has not been tested previously in South Africa for TES. Since ambient temperature and humidity affect the performance of zeolite 13X, it is important to evaluate (at lab-scale) if this type of system is feasible before implementation in industry. This section details the design of the packed bed testing facility, the apparatus used for experimentation and the method followed during testing.

3.1 Packed Bed Test Rig

The packed bed test rig consists of a blower, electric heater, humidifier and zeolite reactor (refer to Appendix A). The packed zeolite bed employs two separate configurations i.e., for charging (Figure 3-1) and discharging (Figure 3-2) the packed bed. The setup designated by the area within the dashed lines changes from the charging to discharging cycle.

During the charging cycle, ambient air is drawn into the blower through a conical inlet flowmeter (refer to Appendix A for details) to measure the differential pressure and calculate the mass flow rate through the system. The air is then transferred to the electric heater where it is heated to approximately 200 °C, with the blue and red arrows (in Figure 3-1) indicating the flow path of the air through the system. Blue indicates cold/ambient air while red indicates air that is heated. The hot and relatively dry air, expelled from the heater, passes through the reactor and releases the water trapped in the zeolite by breaking the chemical bonds between the adsorbent (zeolite 13X) and adsorbate (water). After passing through the bed, the warm humid air is exhausted to the atmosphere

The reactor comprises of a cylindrical test section that is 620 mm long and 400 mm in diameter, constituting an active volume of 0.078 m³. The mass of zeolite in the reactor is approximately 47.5 kg based on the bulk density of 610 kg/m³ in Table 2-8. A diffuser is placed at the inlet of the reactor to lower the velocity and to ensure a more even distribution of air through the packed bed. A nozzle is placed at the exit of the reactor to enable a smooth flow through the system with a raised velocity to facilitate the use of economically sized piping in the exhaust ducting. The reactor contains 18 thermocouple ports to measure the temperature distribution through the bed both at different radii and axial positions as defined in Section 3.2. Humidity sensors (refer to appendix A) were placed close to the conical inlet as well as at the inlet and outlet of the reactor to record the temperature and relative humidity in the system. The reactor is insulated using 75 mm thick ceramic fibre blanket to minimise heat losses to atmosphere.

The heater is removed from the main air stream and connected to the humidifier for the discharging cycle (refer to Figure 3-2). A secondary blower is introduced which supplies air to the heater. The humidifier produces steam, which is added to the air entering the reactor, to increase the level of water

vapour supplied to the packed bed for testing under different humidities. As before, the flow path of the air through the reactor and humidifier is represented by blue and red arrows as shown in Figure 3-2. It is important to note that the humidifier was manually controlled, in terms of temperature and water level. This proved to be challenging in maintaining a constant level of moisture entering the reactor during discharging.

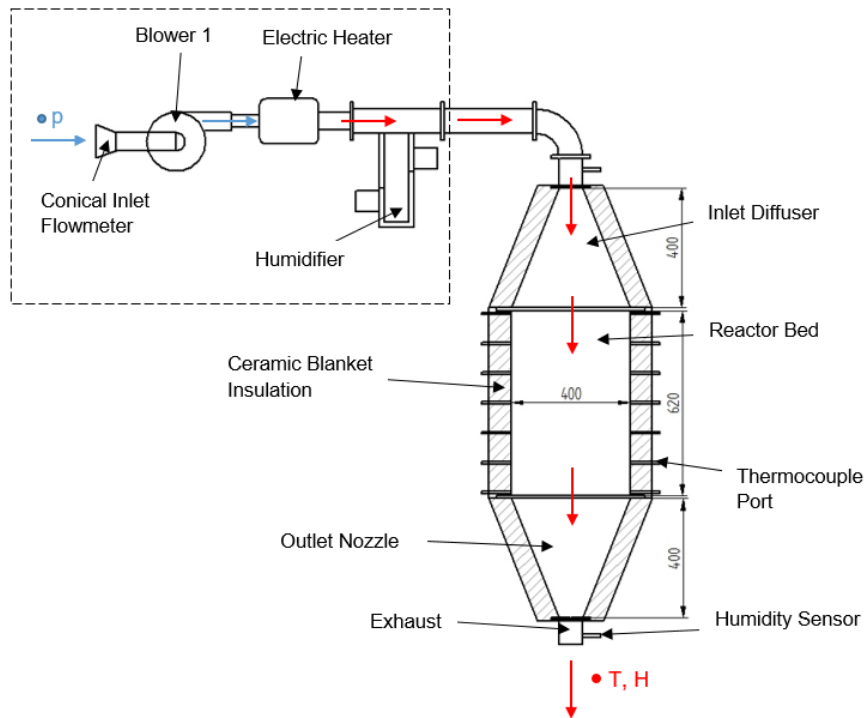


Figure 3-1: Diagram of packed bed test facility (charging/ desorption configuration)

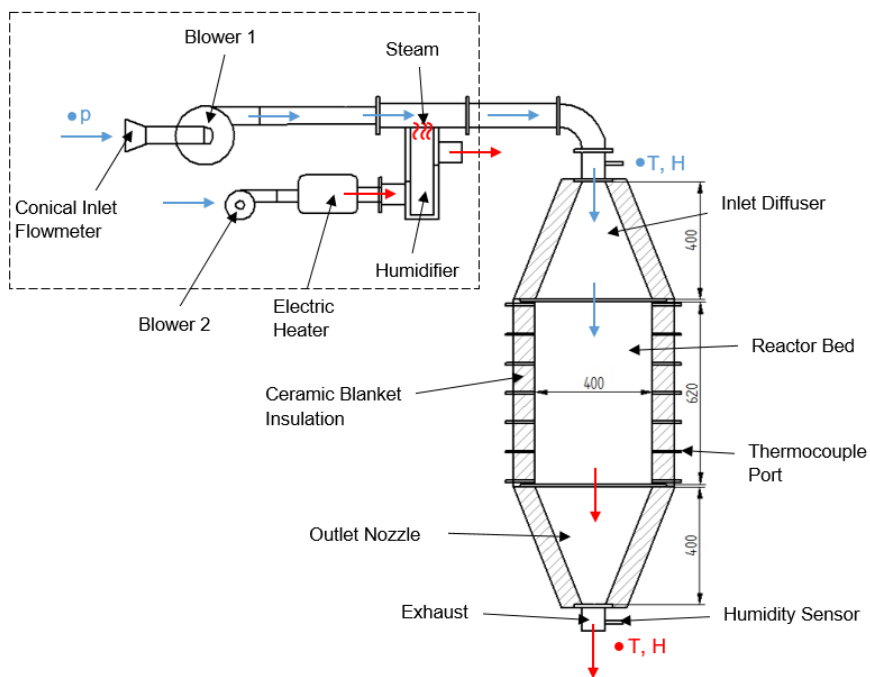


Figure 3-2: Diagram of packed bed test facility (discharging/ adsorption configuration)

The CAD model of the rig, which was designed in Solid Edge, is presented in Figure 3-3. A grating was designed, for the base of the reactor, to support the zeolite beads. A fine stainless-steel mesh (2 mm) was placed over the grating to further support the zeolite spheres (3-5mm diameter) while minimising the obstruction to the air flowing through the reactor.

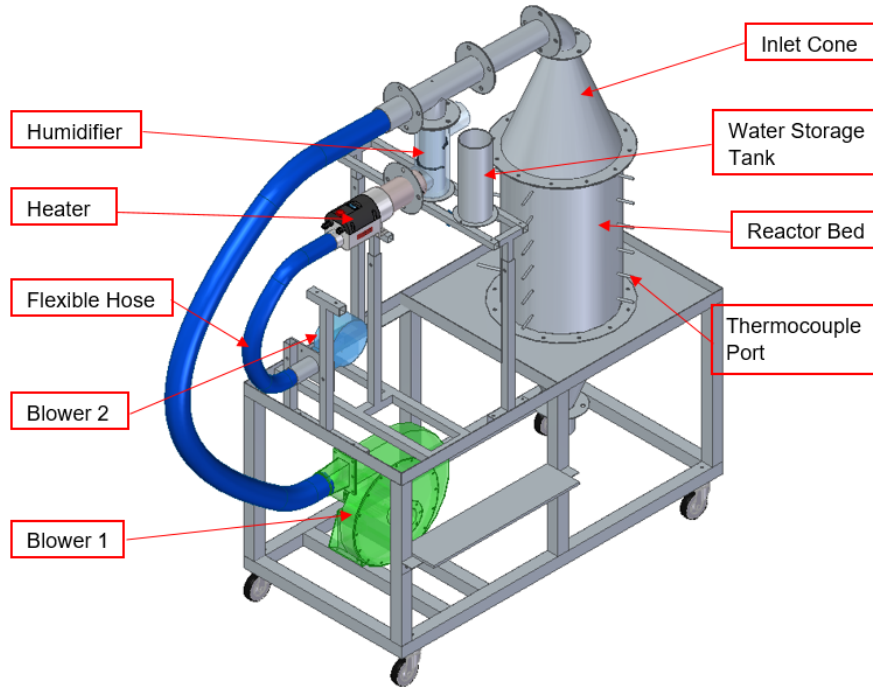


Figure 3-3: CAD model of packed bed test facility

A picture of the final assembly, showing the charging and discharging configuration, is shown in Figure 3-4. The orange hose (refer to left image in Figure 3-4) at the bottom/outlet of the reactor conveys the warm exhaust air to the atmosphere.



Figure 3-4: Full Assembly showing charging (left) and discharging (right) configuration

3.2 Thermocouple Positions

Eighteen type-K thermocouples were placed axially, at 100 mm increments along the 620 mm high axis of the reactor, and radially ($r = 100 \text{ mm}$ and $r = 195 \text{ mm}$) at certain axial locations. Figure 3-5 (left) shows three thermocouples, placed at the centre of the bed, at $r = 100 \text{ mm}$ and $r = 195 \text{ mm}$ (to measure the approximate wall temperature) at one axial level. Figure 3-5 (right) gives a visual layout of the thermocouples distributed throughout the reactor. Table 3-1 presents the exact position of the thermocouples, within the packed bed, with respect to axial and radial distance.

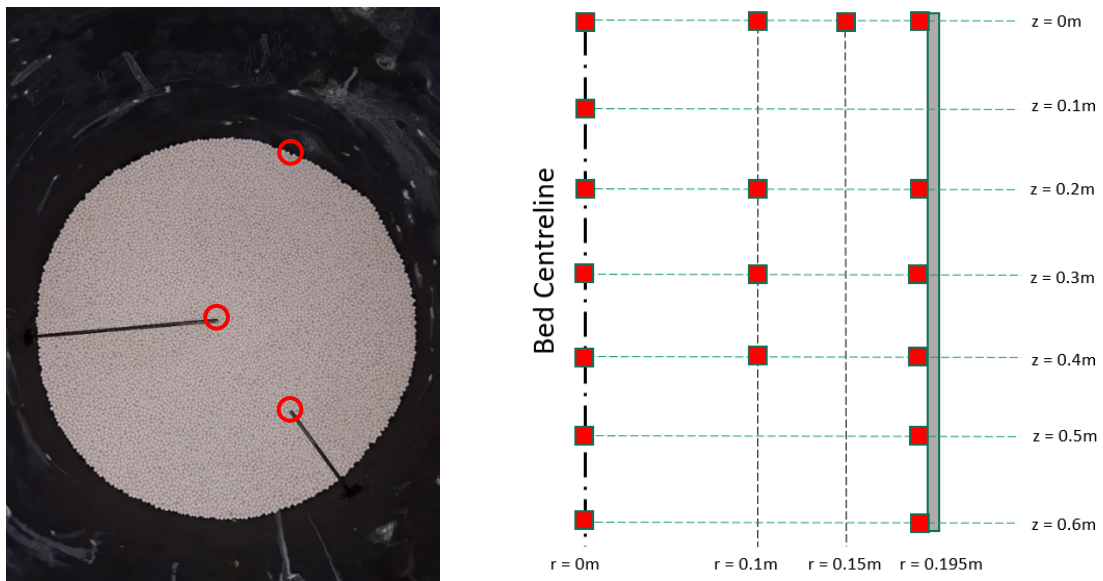


Figure 3-5: Thermocouples placed in reactor bed (left) and Thermocouple locations (right)

Table 3-1: Thermocouples at different axial and radial distances

	Radial Distance (r)			
Axial Distance from Inlet (z)	0 mm	100 mm	195 mm	150 mm
0 mm	TC15	TC17	TC16	TC18
110 mm	TC14	-	-	-
210 mm	TC11	TC13	TC12	
310 mm	TC8	TC10	TC9	
410 mm	TC5	TC7	TC6	
510 mm	TC3	-	TC4	
620 mm	TC1	-	TC2	

3.3 Experimental Method

The aim of this research was to investigate the performance of a zeolite TES for waste heat recovery and thermal energy storage in the South African industrial sector. In a waste heat stream, the temperature typically varies as observed in the ceramic manufacturing process (described in Section 1.2). The sintering kiln generates an exhaust temperature above 800 °C initially, which decreases over time as the contents of the kiln cool to ambient temperature.

3.3.1 Determination of the effect of charging temperature

As mentioned in Section 2.2, zeolite 13X becomes hydrothermally unstable at temperatures above 200 °C. It was therefore decided to limit the temperature to 200 °C. By diluting the sintering kiln exhaust with ambient air, 200 °C can be easily achieved. However, as the contents of the kiln cool, it will be difficult to maintain the temperature at 200 °C. It was therefore decided to also regenerate the zeolite at lower temperatures to determine the impact on system performance, especially in defining the heat storage capacity of the zeolite bed. This would allow the user to estimate the amount of energy that will be stored and what could be recovered at a later stage in order to feed a particular industrial process.

3.3.2 Determination of the effect of humidity

Another important factor (as mentioned in literature) is the humidity during discharging. The humidity significantly affects the temperature lift as noted in previous work. Humidity cannot be easily controlled as it depends on ambient conditions. In an industrial setting, the system would be operational throughout the year. It was therefore decided to test the system under different humidities to predict how it would perform in different seasons and areas.

3.3.3 Determination of the effect of flow rate

Finally, the flow rate through the system depends on various factors and will be different for each application. It is therefore imperative to determine the impact of the flow rate on the system performance.

3.4 Experimental Scope

3.4.1 Maximum temperature, variable humidity, maximum flow rate,

Numerous tests were conducted of which the best eight were chosen to be included in this thesis. A regeneration temperature of 200 °C was chosen for the first three cycles. After regeneration/charging, the bed was allowed to cool to ambient temperature. By allowing the sensible heat to be lost, the thermochemical component of the heat storage could be identified in isolation. During discharging the flow rate was kept at the maximum (achievable by the blower) and the humidity was varied for the first three cycles. The specific humidity was expected to impact the temperature lift as seen in previous studies

3.4.2 Maximum temperature, maximum humidity, variable flow rate

For the next two runs (cycle 4 and 5) the flow rate was lowered with the regeneration temperature and humidity at the maximum value achievable by the humidifier. Lower flow rates should increase the discharging cycle time as the mass transfer and hence adsorption rate is lower

3.4.3 Variable temperature, maximum humidity, maximum flow rate

For cycle 6 and 7, the regeneration temperature was lowered (i.e. to 160 °C and 130 °C) with the flow rate and humidity at the maximum (which depends strongly on ambient humidity)

3.4.4 Prospect of long-term heat storage

The final test (cycle 8) was included to highlight the fact that zeolite can store heat indefinitely with minimal losses. A period of five months lapsed between the charging and discharging cycles due to the national Covid-19 lockdown.

3.4.5 Partial charge/discharge cycles

In an industrial setting, the packed bed may be partially discharged or discharged immediately after regeneration if the stored heat is required. Therefore, two additional sets of results were presented to indicate how the system would behave, during regeneration, if partially discharged or if discharged immediately after regeneration with the sensible heat included.

3.4.6 Industrial application of zeolite 13X

After generating decent results from the charging and discharging cycles, it was important to demonstrate how this system could be utilised in industry. Ceramic casting moulds were obtained from the company (described in Section 1.2) and dried using heat from the packed bed reactor.

3.4.7 Moisture adsorption capacity of zeolite 13X

Lastly, the water content of the zeolite before and after adsorption is necessary for calculations such as the temperature lift and energy storage capacity. It was therefore decided to perform tests on 1 kg samples of zeolite 13X to determine the impact of relative humidity on the water adsorption capacity of zeolite 13X

3.5 Experimental Analysis

The results were then evaluated to determine the performance of the system i.e. the energy efficiencies, temperature lift, storage capacity and moisture adsorption capacity for the eight complete discharge cycles. The next section provides a detailed overview of the equations used to calculate the energy supplied, stored and released as well as the equations used to calculate the energy efficiency of the system.

4 Energy Analysis of an Open Sorption System

This chapter presents the method used to calculate the energy supplied, stored and released as well as the equations used to calculate the efficiencies of the system. It is convenient for defining the energy balance of the overall open system to break it down into the two constituent processes, namely charging and discharging, and to analyse the mass and energy balances for these two processes.

A typical charging or regeneration process is illustrated at the left of Figure 4-1. This process requires a heat input which can be obtained from waste heat or solar energy to reduce environmental impact [16]. In the case of zeolite 13X and water this requires a temperature exceeding the evaporation temperature of water. Therefore, hot relatively dry air is supplied to the adsorbent which dehydrates the adsorbent; an endothermic reaction. This results in a humid air stream leaving the reactor at a lower temperature [24]. During discharging (refer to the right of Figure 4-1), cool ambient air with adequate humidity is supplied to the adsorbent. Water is adsorbed by the adsorbent and the exothermic heat of adsorption is released [24].

To analyse the mass and energy balance in this particular system, it will be divided into three sections with three different mass flow rates and enthalpies (refer to Figure 4-1). The first point of interest is at the inlet of the system, where air is sucked in, through the conical inlet flow meter. The second and third sections are the inlet and outlet of the zeolite reactor respectively.

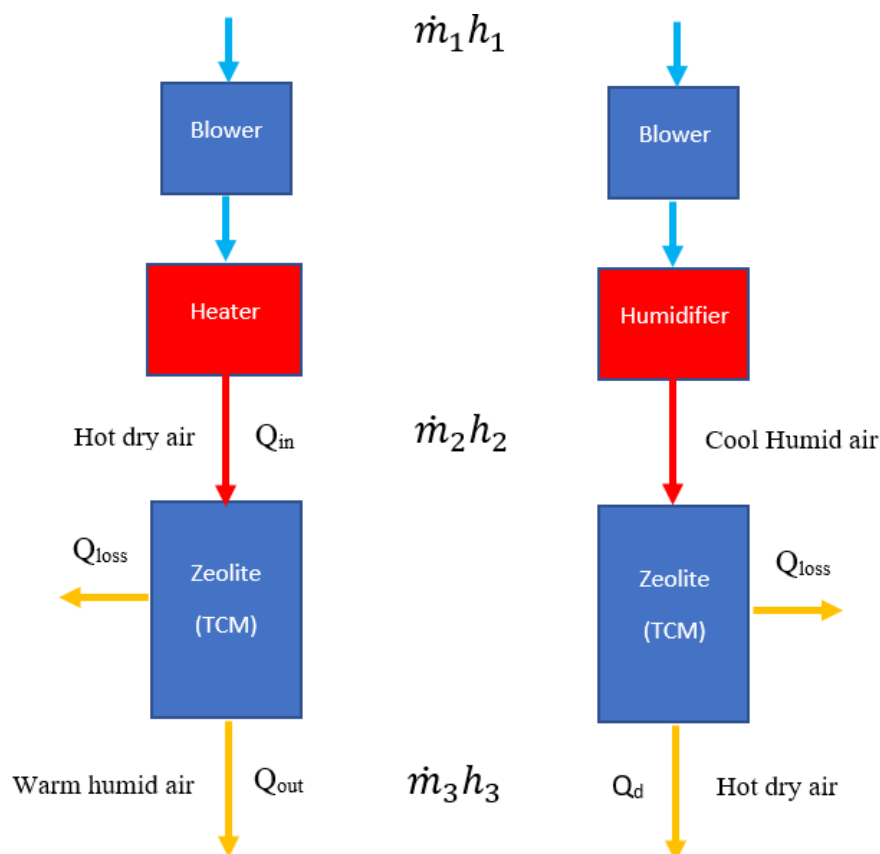


Figure 4-1: Desorption/ Charging Process (left) and Adsorption/Discharging Process (right) [24]

4.1 Conservation of mass principle

During charging and discharging, the mass flow rate of dry air (\dot{m}_{da}) through the system remains constant and hence does not require a numerical subscript as indicated in equation (4-1):

$$\dot{m}_{1,da} = \dot{m}_{2,da} = \dot{m}_{3,da} = \dot{m}_{da} \quad (4-1)$$

The mass flow rate of water vapour, however, changes through the system for both the charging and discharging cycles.

4.1.1 Charging cycle

During charging (between point 1 and 2), the water content remains the same (i.e., $x_1 = x_2$) since only heat is added to the system. The mass flow rate of water vapour (\dot{m}_w) can be calculated from the product of the humidity ratio (x : kg_w/kg_{da}) and the mass flow rate of dry air through the system for each point:

$$\dot{m}_{1,w} = x_1 \dot{m}_{da} = x_2 \dot{m}_{da} \quad (4-2)$$

Between point 2 and 3 water is released or desorbed (\dot{m}_{des}) from the zeolite effectively adding to the flow entering the reactor (at point 2) in order to produce an increased mass flow at 3:

$$x_2 \dot{m}_{da} + \dot{m}_{des} = x_3 \dot{m}_{da} \rightarrow \dot{m}_{des} = \dot{m}_{da}(x_3 - x_2) \quad (4-3)$$

The total mass flow rate entering the reactor (i.e., water vapour and dry air) can be calculated as follows:

$$\dot{m}_1 = \dot{m}_2 = \dot{m}_{da} + x_2 \dot{m}_{da} \quad (4-4)$$

The total mass flow rate leaving the reactor can be calculated as follows:

$$\dot{m}_3 = \dot{m}_2 + \dot{m}_{des} \quad (4-5)$$

4.1.2 Discharging cycle

During the discharging cycle (between 1 and 2) steam (\dot{m}_{steam}) is added to the inlet air (from the humidifier). The mass flow rate of water vapour changes as follows:

$$x_1 \dot{m}_{da} + \dot{m}_{steam} = x_2 \dot{m}_{da} \rightarrow \dot{m}_{steam} = \dot{m}_{da}(x_2 - x_1) \quad (4-6)$$

$$\dot{m}_1 = \dot{m}_{da} + x_1 \dot{m}_{da} \quad (4-7)$$

$$\dot{m}_2 = \dot{m}_1 + \dot{m}_{steam} \quad (4-8)$$

Between 2 and 3, the water entering (at point 2) is adsorbed by the zeolite and dry air leaves the system therefore:

$$\dot{m}_3 = \dot{m}_{da} \quad (4-9)$$

Evaluating the mass flow rates thus requires measurements of the humidities at various points in the flow circuit as mentioned in Section 3.1.

4.2 Conservation of energy principle

For low velocity flows, the kinetic energy can be neglected [42] as it much lower than the enthalpy values. Similarly, the potential energy can also be neglected as the difference in height between the inlet and outlet of the reactor is relatively small. The focus was therefore placed on the heat transfer through the system. Furthermore, if the bed of zeolite is allowed to lose all its sensible heat before discharge is initiated then the internal energy is that of the exothermic reaction alone, since the sensible heat stored has been eliminated.

The energy balance for the process can be expressed in the following equation, where the difference between the energy entering the system (Q_{in}) and leaving the system (Q_{out}) equates to the change in the internal energy of the system (ΔQ_{system}) [42].

$$Q_{in} - Q_{out} = \Delta Q_{system} \quad (4-10)$$

4.2.1 Charging cycle

During the charging cycle, heat (Q_{in}) is supplied to the system and can be calculated from the following equation where $Q_{loss,1-2}$ is the heat lost through the piping between the heater and the inlet of the reactor:

$$Q_{in} = Q_2 - Q_1 + Q_{loss,1-2} \quad (4-11)$$

$$\dot{Q}_{in} = \dot{m}_2 h_2 - \dot{m}_1 h_1 + Q_{loss,1-2} \quad (4-12)$$

Since the pipe between the heater and reactor inlet (point 2) was well insulated and relatively short (approximately 0.6 m), the losses can be neglected. Furthermore, the net amount of energy supplied at the reactor inlet is required to evaluate the energy efficiencies of the zeolite in the reactor. As mentioned, during charging $x_1 = x_2$ and therefore $\dot{m}_1 = \dot{m}_2$ and Q_{in} becomes:

$$\dot{Q}_{in} = \dot{m}_1(h_2 - h_1) \quad (4-13)$$

The amount of energy stored (Q_s) in the zeolite can be calculated from the following equations, where $Q_{loss,2-3}$ is the heat losses through the wall of the reactor:

$$Q_s = Q_2 - Q_3 - Q_{loss,2-3} \quad (4-14)$$

$$\dot{Q}_s = \dot{m}_2 h_2 - \dot{m}_3 h_3 - \dot{Q}_{loss,2-3} \quad (4-15)$$

According to Ismail [43], the overall heat transfer coefficient (U_w) for losses through the wall of the reactor can be calculated as follows:

$$U_w = \frac{1}{\frac{1}{A_0 h_w} + \frac{\ln[(r_0 + e)/r_0]}{2\pi L k_{iso}} + \frac{1}{A_x h_x}} \quad (4-16)$$

Where h_w is the heat transfer coefficient between the fluid and wall; A_0 is the cross-sectional area of the reactor; L is the height of the reactor; k_{iso} is the thermal conductivity of the insulating material; h_x is the heat transfer coefficient between the insulation and the surrounding air and A_x is the surface area of the insulation.

$$h_x = 1.42 \left(\frac{\Delta T}{L} \right)^{1/4} \quad (4-17)$$

$$h_w = \left(\frac{k_f}{2d_p} \right) [2.576 Re^{1/3} Pr^{1/3} + 0.0936 Re^{0.8} Pr^{0.4}] \quad (4-18)$$

Where k_f is the thermal conductivity of the fluid (air), d_p is the diameter of the zeolite particle and ΔT is the temperature difference between the air in the reactor and ambient. The losses through the reactor wall can be calculated from the following equation:

$$Q_{loss,2-3} = U_w A_w \Delta T \quad (4-19)$$

4.2.2 Discharging cycle

The amount of energy discharged (Q_d) from the zeolite can be calculated from the following equations, where $Q_{loss,2-3}$ is the heat losses through the wall of the reactor:

$$Q_d = Q_3 - Q_2 + Q_{loss,2-3} \quad (4-20)$$

$$\dot{Q}_d = \dot{m}_3 h_3 - \dot{m}_2 h_2 + \dot{Q}_{loss,2-3} \quad (4-21)$$

4.2.3 Overall Process

The overall energy balance can be written as follows where Q_{in} is the energy supplied during charging, Q_{out} is the energy that leaves the reactor during charging, Q_d is the energy released during discharging and Q_{loss} is the combined heat losses through the reactor wall during charging and discharging:

$$Q_{in} - Q_{out} = Q_d + Q_{loss} \quad (4-22)$$

4.3 Energy Efficiency

The equations to calculate the efficiencies for the charging, discharging and overall process are described in the next sections.

4.3.1 Charging Process

The efficiency of the system during charging can be calculated from the ratio of the amount of energy actually stored (Q_s) and the amount of energy supplied during charging (Q_{in}) [24]:

$$\eta_c = \frac{Q_s}{Q_{in}} \quad (4-23)$$

4.3.2 Discharging Process

The discharging efficiency can be calculated from the ratio of the heat released during discharging (Q_d) and the amount of energy stored (Q_s) [24]:

$$\eta_d = \frac{Q_d}{Q_s} \quad (4-24)$$

4.3.3 Overall Process

The overall energy efficiency can be calculated by dividing the heat released during discharging (Q_d) by the amount of energy supplied during charging (Q_{in}) [24]:

$$\eta_o = \frac{Q_d}{Q_{in}} \quad (4-25)$$

5 Experimental Results

The purpose of this research was to demonstrate the potential of zeolite 13X for thermal storage in the South African climate. The three main parameters (i.e., regeneration temperature, flow rate and humidity) were chosen to be varied during experimentation. The intention was to analyse the impact that these three parameters have on the energy efficiency of an open TCES using zeolite 13X-water as the adsorbent-adsorbate pair. At higher regeneration temperatures zeolite 13X would be expected to be drier and therefore able to store more heat during desorption and release more heat during adsorption. The specific humidity was expected to impact the temperature lift as seen in previous studies. Lower flow rates should increase the adsorption cycle time as the mass transfer and hence adsorption rate is lower. To determine the behaviour of the reactor, the temperature was monitored at different axial and radial positions. Furthermore, the prospect of long-term energy storage (for TCES) was investigated and the impact on the energy released from the system was determined. The experimental results from three complete charging/ regeneration and eight complete discharging cycles are presented in this section. One complete charging and discharging cycle are discussed in detail while the others can be found in Appendix B. The axial and radial temperatures, humidity, mass flow rate and the heat stored/ released are presented and discussed for each of these cycles. Some important additional results from charging/ discharging cycles are also included in this section. The potential of zeolite 13X, for drying processes in industry, was demonstrated by controlling the packed bed outlet temperature and testing the drying rate of ceramic casting moulds. Tests were also performed on 1 kg samples of zeolite 13X to determine the impact of relative humidity on the water adsorption capacity of zeolite 13X. It is expected that higher relative humidities will lead to a higher mass of water being adsorbed as seen in [44].

5.1 Charging/ Regeneration Cycle Testing

The charging/ regeneration cycle results are presented in this section. The packed bed was regenerated at three different temperatures i.e., 130 °C, 160 °C and 200 °C. The results are summarised in Table 5-1.

Table 5-1: Charging/ regeneration cycle results

Cycle no.	Inlet temp. (°C)	Avg. inlet humidity (g _w /kg _{da})	Max. outlet humidity (g _w /kg _{da})	Avg. mass flow rate (kg/h)	Cycle duration (h)	Q _{in} (kWh)	Q _s (kWh)
1	200	13	46	135	3.5	20.45	13.64
2	160	7	34	139	4.5	22.45	11.99
3	130	7	30	142	6	24.69	10.47

5.1.1 Charging Cycles 1-3

The axial temperature profiles for charging cycle 1 are presented in Figure 5-1. The temperatures were measured using K-type thermocouples, which were calibrated by ‘Repair and Metrology Service (Pty) Ltd,’ with a maximum deviation of 0.2 °C. The results were consistent with those achieved by Tatsidjodoung [15] in terms of the shape of the temperature profiles. The temperature of the air, entering the reactor, was raised to 200 °C by the electric heater. At the beginning of the cycle (between $t = 0$ h and $t = 0.2$ h), the upper layers of zeolite 13X were heated by the inlet air stream, resulting in the desorption of water vapour. This warm water vapour condensed on the cooler zeolite particles at lower levels (from $z = 0.11$ m to $z = 0.62$ m) in the packed bed resulting in an increase in temperature from ambient temperature to 45 °C. The temperature remains at 45 °C until the desorption front reaches that particular layer leading to a further increase in temperature as the water is evaporated. Once desorption is completed on that particular layer the temperature rises to 200 °C. As the thermocline moved through the bed subsequent layers of zeolite underwent the desorption of water vapour, until eventually the entire packed bed was regenerated, and the exit temperature ($z = 0.62$ m) was raised to 200 °C. The regeneration cycle lasted for approximately 3.5 hours.

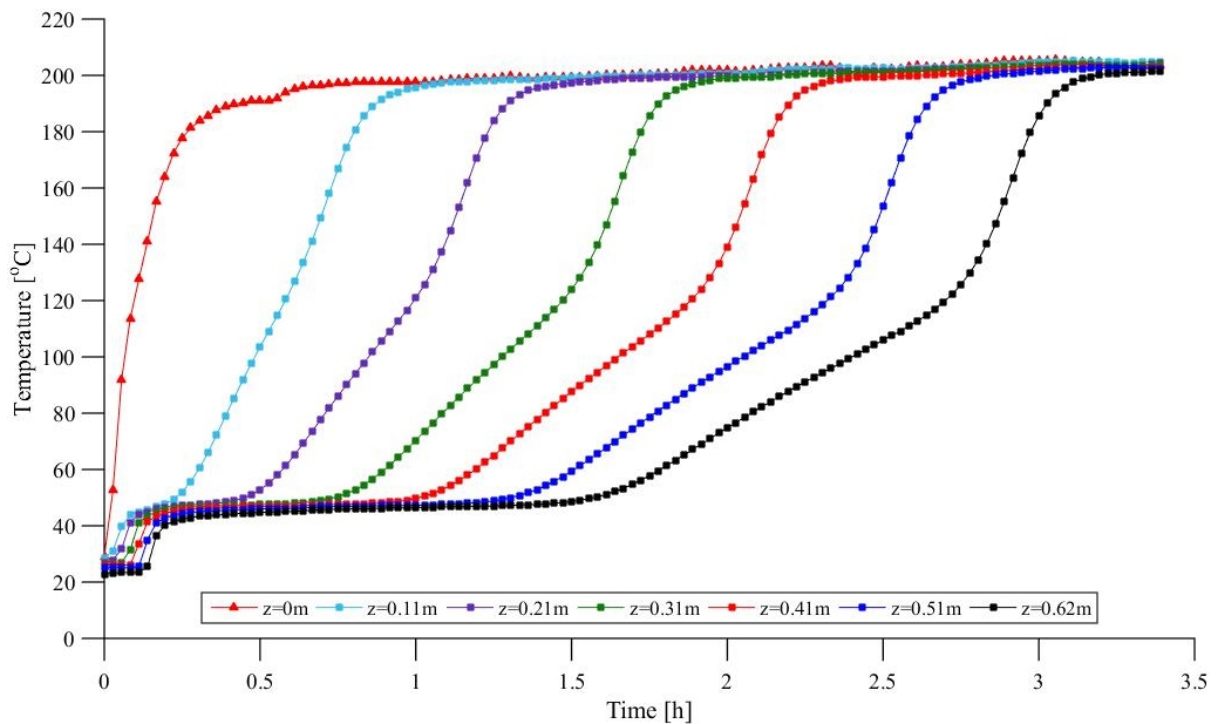


Figure 5-1: Axial temperature profiles at various bed depths (z) - Charging cycle 1

The humidity was recorded at the outlet of the rig for the entire cycle using the Testo high temperature probe. The maximum humidity at the outlet was 45 $\text{g}_w/\text{kg}_{\text{da}}$ which was achieved after 30 minutes. The humidity started to decrease from 90 minutes, since approximately half the bed is dry, and continued to decrease to 27 $\text{g}_w/\text{kg}_{\text{da}}$ around the 3-hour mark. Thereafter it started to increase before levelling off at around 33 $\text{g}_w/\text{kg}_{\text{da}}$ towards the end of the test. The outlet humidity should

continue to decrease (from 90 minutes) as the bed dries and should agree with the inlet humidity at the end of the test as no more water is being desorbed. However, the relative humidity sensor becomes less accurate as the temperature increases above 100 °C. The Testo RH sensor used for experimentation was calibrated by ‘Montech Calibration Services’ with a maximum deviation of 2.2% RH. According to [45], an instrument with a 2% RH accuracy will only indicate a $\pm 34\%$ accuracy of the actual/ specific humidity in the air at a temperature of 200 °C. This can be observed clearly since the outlet temperature starts to rapidly increase around the 3-hour mark and at the same time the outlet humidity starts to increase instead of decreasing. The inlet humidity was measured using the HTM2500LF humidity sensor (refer to Appendix A) which measured the ambient humidity (approximately 13 $\text{g}_w/\text{kg}_{da}$) entering the blower. The average mass flow rate achieved was 135 kg/h (refer to Figure 5-2). The flowrate varied by 2% during the cycle. The mass flow rate is a function of the density of air (which depends on temperature), and therefore decreases slightly as the bed heats up. Slight expansions in the zeolite pellets may result in a higher pressure drop across the packed bed, thus further contributing to a decrease in flow rate as the bed is heated.

The radial temperature profiles at various bed depths are presented in Figure 5-3. The results show that the temperature in the vicinity of the bed wall is up to 30 °C lower than the peak axial temperature. This is due to heat losses through the walls of the test rig, as well as through the metal mesh at the base of the test rig. There appears to be some channelling that is exhibited in the packed bed, since the temperature at a 0.1 m radius rose faster than at the centre of the bed.

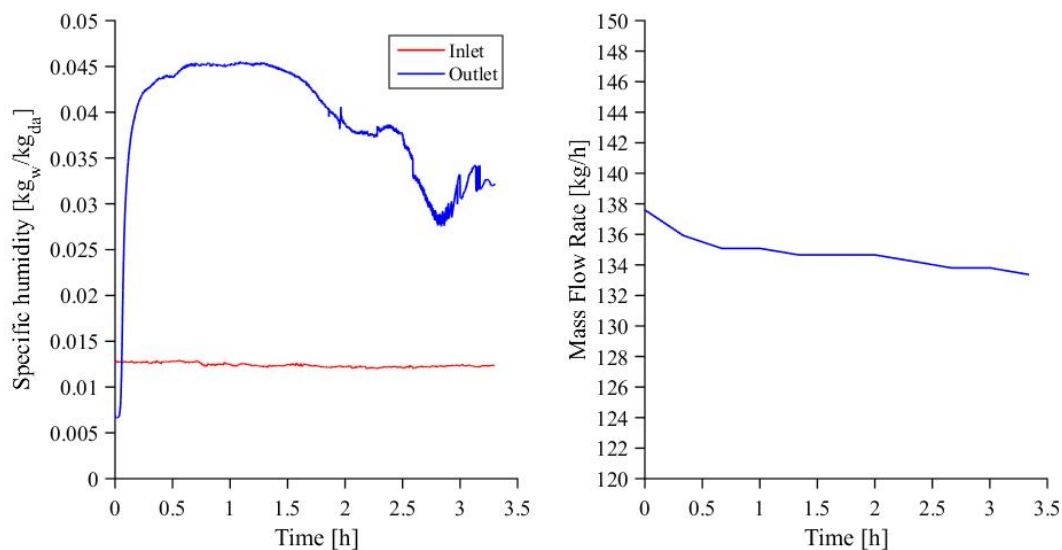


Figure 5-2: Humidity and Mass flow rate - Charging cycle 1

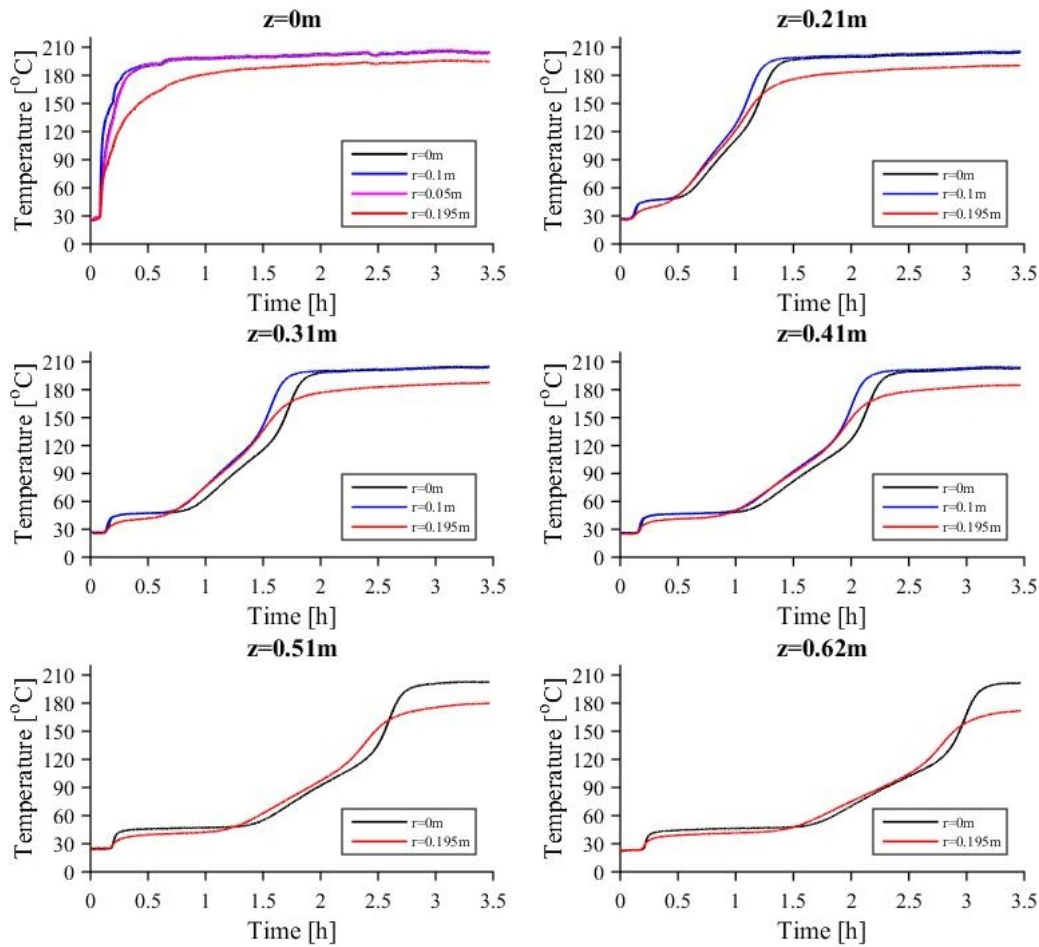


Figure 5-3: Radial temperature profiles at various bed depths (z) - Charging cycle 1

Two further charging tests were performed at the lower temperatures of 160 °C and 130 °C. To compare these tests with the 200 °C cycle, the inlet and outlet temperatures for all three cycles are plotted on one axis in Figure 5-4. The detailed explanation for the 160 °C and 130 °C tests are presented in Appendix B. These results, as expected and confirmed in Table 5-1 and Figure 5-4, return much slower charging times; 4.5 h and 6 h respectively compared to the 200 °C charge cycle of 3.5 hrs. Other than this difference the curves follow very similar trends of temperature versus time at the various depths within the bed. As a consequence, the explanations of the charging performance at 200 °C also applies essentially to the performance at lower charging temperatures. Thus, the data summarized in Table 5-1 gives an adequate overall indication of performance whilst the appendix can be accessed for more detail. It should be noted that more water is released at higher temperatures (per unit time) as the max outlet humidity is 46 g_w/kg_{da}, 34 g_w/kg_{da} and 30 g_w/kg_{da} for the 200 °C, 160 °C and 130 °C charge cycles respectively.

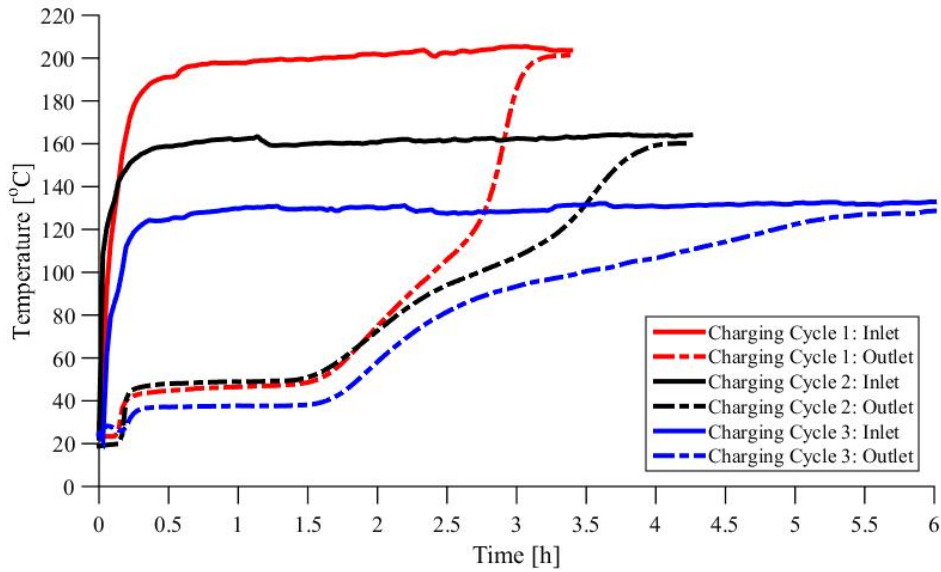


Figure 5-4: Packed bed inlet and outlet temperatures - Charging cycles 1- 3

The energy supplied (Q_{in}) to the packed bed and the energy stored (Q_s) during charging cycles 1-3 is presented in Figure 5-5. The method used to calculate the energy input is discussed in Section 4.1.1 and a sample calculation is presented in Appendix C. The energy supplied increases as the temperature of the air (entering the packed bed) rises to the regeneration temperature and thereafter remains almost constant until the end of the cycle. By integrating the curves, the total amount of energy supplied to the packed bed was 20.45 kWh, 22.45 kWh and 24.69 kWh for charging cycle 1, 2 and 3 respectively. This result is discussed in detail below.

The energy stored (Figure 5-5) during charging was calculated based on the equations presented in Section 4.2.1. A maximum of 5.8 kW was absorbed during charging cycle 1 (200 °C). By integrating the curve, the total amount of energy stored by the packed bed equates to 13.64 kWh. A maximum of 4.9 kW was absorbed during charging cycle 2 (160 °C) while the total energy absorbed by the packed bed was 11.99 kWh; a reduction of 12.1% when compared to charging cycle 1. For this cycle (2) the temperature lift at the inlet (refer to Figure 5-4) was very steep at the beginning of the cycle with the maximum temperature being reached sooner than the other two cycles. This resulted in a peak in energy at $t = 0.2$ h since the outlet temperature of the packed bed had not increased at that point and hence the difference in enthalpy (between inlet and outlet) was greater. Once the outlet temperature increased, the energy stored decreased slightly before stabilising for a period of time as seen in charging cycle 1. The increase in outlet temperature occurred at approximately $t = 0.25$ h (refer to Figure 5-4). Finally, a maximum of 3.7 kW was absorbed during charging cycle 3 and 10.47 kWh was stored in the packed bed which was a reduction of 23.2% compared to the 200 °C charging cycle.

The energy supplied to the packed bed was the highest (24.69 kWh) for charging cycle 3 (130 °C) although this was the lowest regeneration temperature and the least amount of energy was absorbed/ stored. By comparing the inlet and outlet temperatures for the three charging cycles (refer to Figure 5-4), it is observed that the outlet temperature rises at approximately 1.5 h for all cycles regardless of regeneration temperature. Once the outlet temperature rises, energy is lost to the atmosphere. Since the outlet temperature (for charging cycle 3) increases very gradually, a large percentage of the energy supplied from $t = 1.5$ h to $t = 6$ h is wasted. Therefore, charging cycle 3 accounts for the largest amount of energy supplied during charging. The energy supplied to the bed during charging cycle 2 (22.45 kWh) was also higher than charging cycle 1 (20.45 kWh) due to the same reasoning. To minimise heat losses to the environment, it is important to evaluate the amount of energy absorbed before and after $t = 1.5$ h.

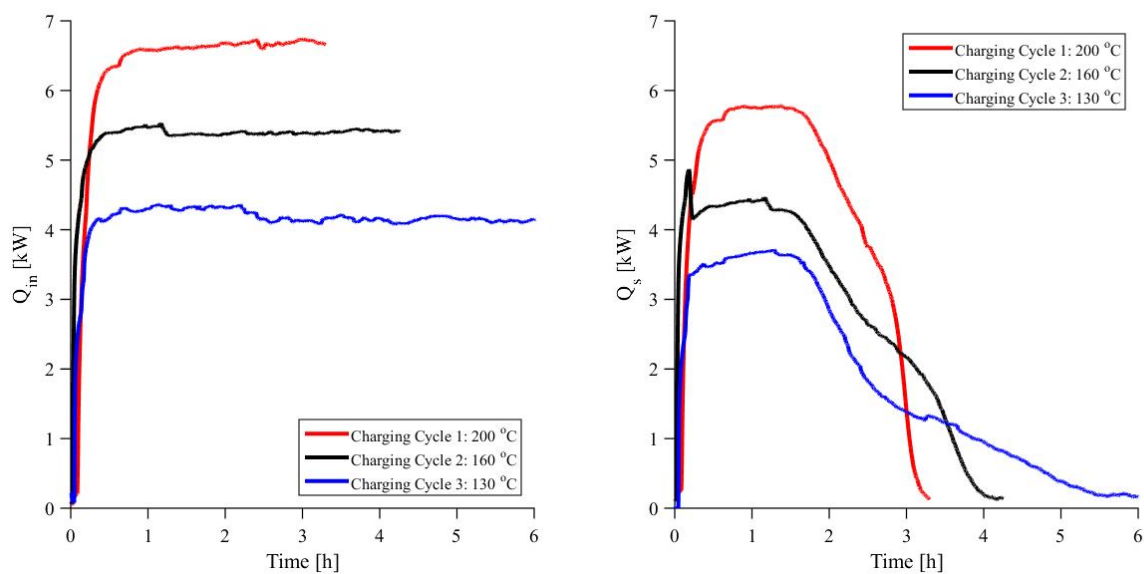


Figure 5-5: Energy supplied (left) and energy stored (right) - Charging cycles 1- 3

The timewise cumulative percentage of energy absorbed from the total energy absorbed is shown on the left in Figure 5-6. Between $t = 0$ and $t = 1.5$ h, 54%, 52% and 47% of the total energy stored is absorbed for charging cycles 1, 2 and 3 respectively. Between $t = 0$ and $t = 3$ h, 98%, 90% and 80% of the total energy stored is absorbed for charging cycles 1,2 and 3 respectively. In Figure 5-6 (right) the percentage of energy stored as a fraction of the energy supplied is plotted. It is interesting to note that between $t = 0$ and $t = 1.5$ h approximately 75-90% of the energy supplied is actually absorbed by the bed. By $t = 3$ h charging cycle 1 is almost complete and the other two cycles are only absorbing 30% of the energy input to the packed bed. From these graphs it would be wise to make the storage larger than required and to not dehydrate the reactor completely. The charging should be stopped when the percentage energy absorbed, from a source of heat supply, drops to below 50% which is between 2-3 h.

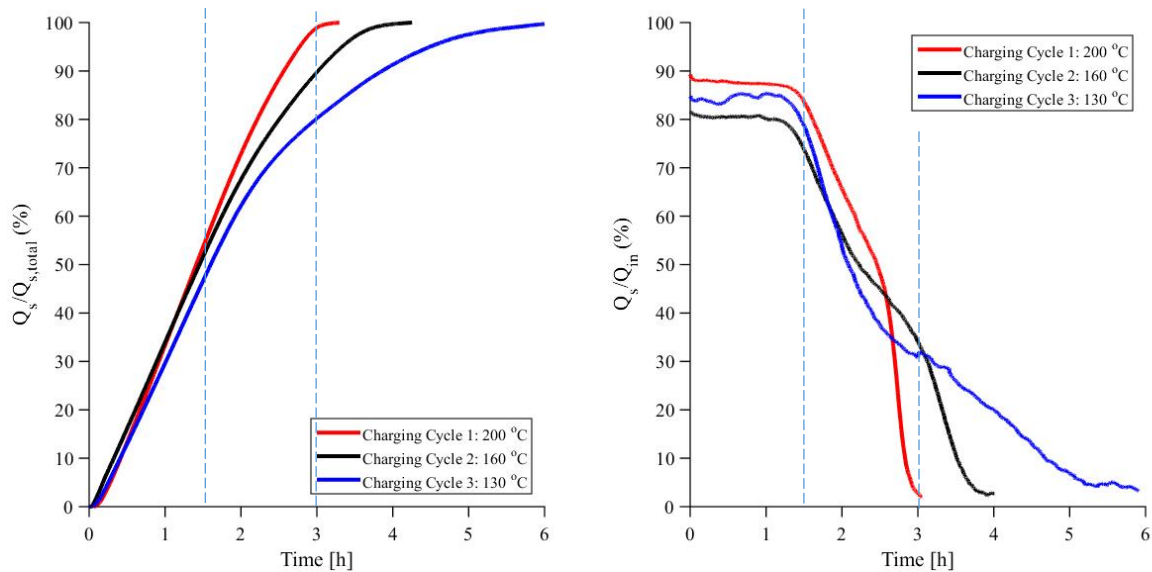


Figure 5-6: The timewise cumulative percentage of energy absorbed from the total energy absorbed (left) and Percentage of energy absorbed from energy supplied (right)

5.2 Discharging Cycle Testing

Eight discharging tests were conducted at different humidities, flow rates and regeneration temperatures using the test procedure outlined in Section 3.4. The results are summarised in Table 5-2. For the first 3 cycles the packed bed was regenerated at 200 °C and discharged at different inlet humidities (25%, 70% and 100% RH). The blower was run at full speed (50 Hz) producing a flow rate between 168-178 kg/h. For discharge cycle 4 and 5 the packed bed was also regenerated at 200 °C before discharging. However, the blower was run at 35 Hz (126 kg/h) and 25 Hz (90 kg/h) respectively with the inlet humidity at approximately 70% RH. Discharge cycles 6 and 7 were performed after charging the packed bed to 160 °C and 130 °C respectively. For the final test presented (cycle 8), the reactor was discharged after a period of 5 months after regeneration due to Covid- 19 lockdown restrictions and the reactor was not sealed allowing the outer layers to adsorb water from the atmosphere. The previous cycles (1-7) were, on the other hand, discharged within a few days after regeneration. However, it should be noted that all the discharging cycles were performed once the packed bed had cooled to ambient after charging. This implies that all the sensible heat from the charging cycle was lost to ambient and was not included in the energy released during discharging. The values in red font (in Table 5-2) indicates the parameter which was varied.

Table 5-2: Discharging cycle results

Cycle no.	Charging temp. (°C)	Avg. inlet humidity (g _w /kg _{da})	Inlet temp. (°C)	Max. outlet temp. (°C)	Max. ΔT (°C)	Avg. mass flow rate (kg/h)	Cycle duration (h)	Energy released (kWh)
1	200	34	31	138	107	177	3	11.56
2	200	26	32	108	75	177	4	11.50
3	200	12	39	76	38	171	7	10.20
4	200	23	30	95	65	126	6	10.19
5	200	24	30	90	60	90	9	10.48
6	160	19	24	83	58	181	4.5	10.73
7	130	7	33	61	28	164	7.5	7.50
8	200	20	27	80	53	172	5	9.83

5.2.1 Discharging Cycle 1: 100% RH

The temperature profiles at the centre of the bed are presented in Figure 5-7. This test was performed on a very humid day. Ambient air was supplied to the inlet of the reactor at approximately 31 °C. The upper layers heated up rapidly, as indicated by the thermocouple at $z = 0.11$ m, due to the heat of adsorption. The heat of adsorption causes the zeolite particles to heat up and therefore there is an element of sensible heat in the storage system. This sensible heat was then transferred from the upper layers to the lower layers of the bed until it reached the lowest layer at the outlet. The adsorption process occurred at the upper layers of zeolite first before proceeding to the next layer below it. Once adsorption was complete on a certain layer and all the sensible heat had been transferred to the air stream, that layer cooled down to ambient temperature. This can be clearly seen on the graph as the bed cooled down to ambient at different times indicating that adsorption was complete on that particular layer. It takes approximately 30 min for the layer at the outlet of the bed to heat up due to sensible heat that was transferred from the upper layers until finally the adsorption reaches the lowest layer, i.e., closest to the outlet. Once adsorption was complete on the lowest layer, and all the sensible heat had been transferred to the air stream, the outlet cooled down to ambient indicating that all the heat stored has been discharged. The maximum temperature achieved at the outlet was 138 °C which is a temperature increase of approximately 107 °C. The cycle lasted for approximately 3 hours.

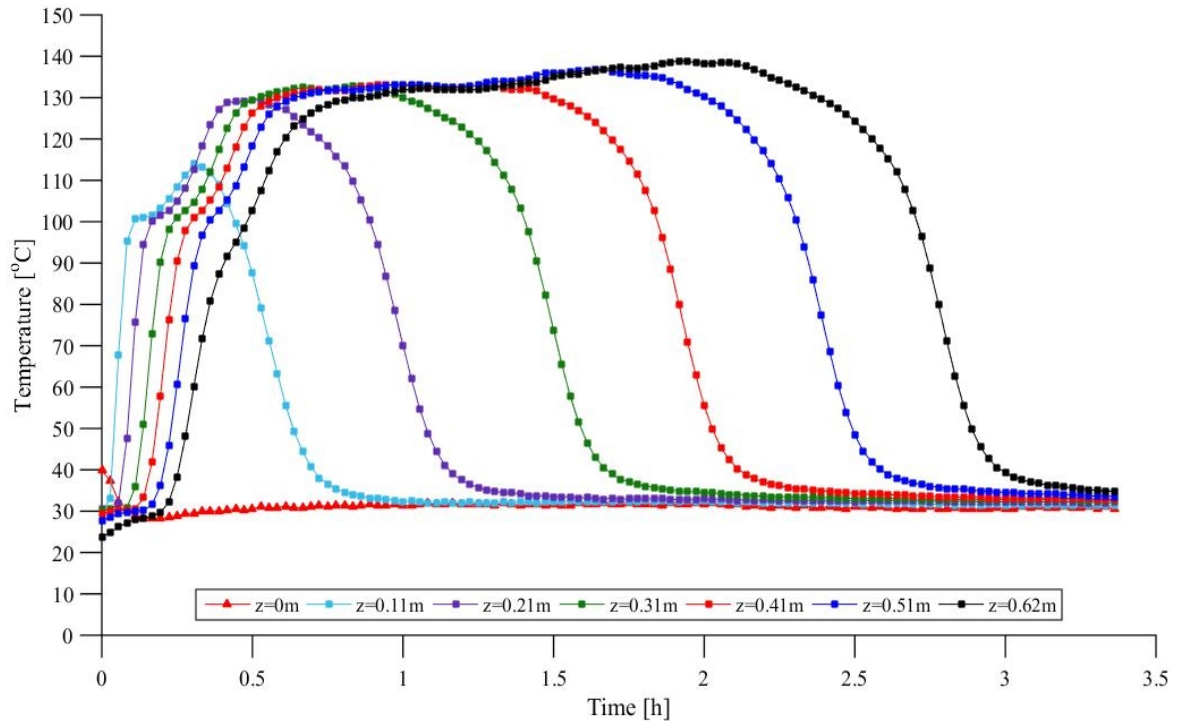


Figure 5-7: Axial temperature profiles at various bed depths (z) - Discharging cycle 1

The humidity at the inlet of the reactor, which was measured by the Testo humidity sensor (refer to Appendix A), at the start of the cycle was approximately $24 \text{ g}_w/\text{kg}_{da}$, before rising and remaining constant at approximately $34 \text{ g}_w/\text{kg}_{da}$ for the rest of the cycle (refer to Figure 5-8). The initial rise in humidity could be due to the water (in the humidifier) not being at the boiling point at the start of the cycle. The humidity of $34 \text{ g}_w/\text{kg}_{da}$ was the highest humidity achieved during testing due to the high ambient humidity. According to the Testo humidity sensor, the relative humidity of the air at the inlet of the reactor was 100% for most of the cycle. The humidity at the outlet was approximately 0%, according to the HTM2500LF humidity sensor (refer to Appendix A), which implies that all the water supplied to the bed was adsorbed by the zeolite. The sensor was removed from the rig once the outlet temperature approached $85 \text{ }^\circ\text{C}$ which is the maximum rated temperature for that sensor. The maximum mass flow rate was 179 kg/h (refer to Figure 5-8). The flow rate varied within 2% during the cycle. Variations in the mass flow rate are due to changes in the air density as the bed heats up.

The temperature profiles at the wall and radial positions at different bed depths (z) are presented in Figure 5-9. The influence of the reactor wall can be clearly seen as the temperature in the wall region ($r = 0.195 \text{ m}$) was lower than the centre of the reactor ($r = 0 \text{ m}$). The temperature also drops significantly faster than the axial temperature due to the adsorption process occurring much faster near the wall region because of the increased porosity and hence fluid velocity near the wall. Furthermore, channelling through the packed bed may have contributed to the adsorption process occurring faster at a radial position of 0.1 m .

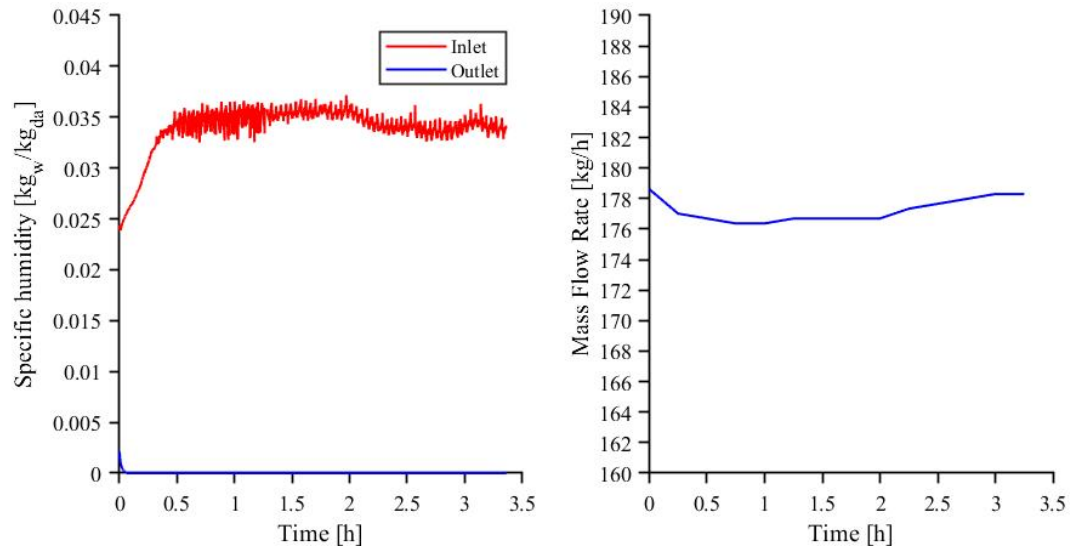


Figure 5-8: Humidity and Mass flow rate - Discharging cycle 1

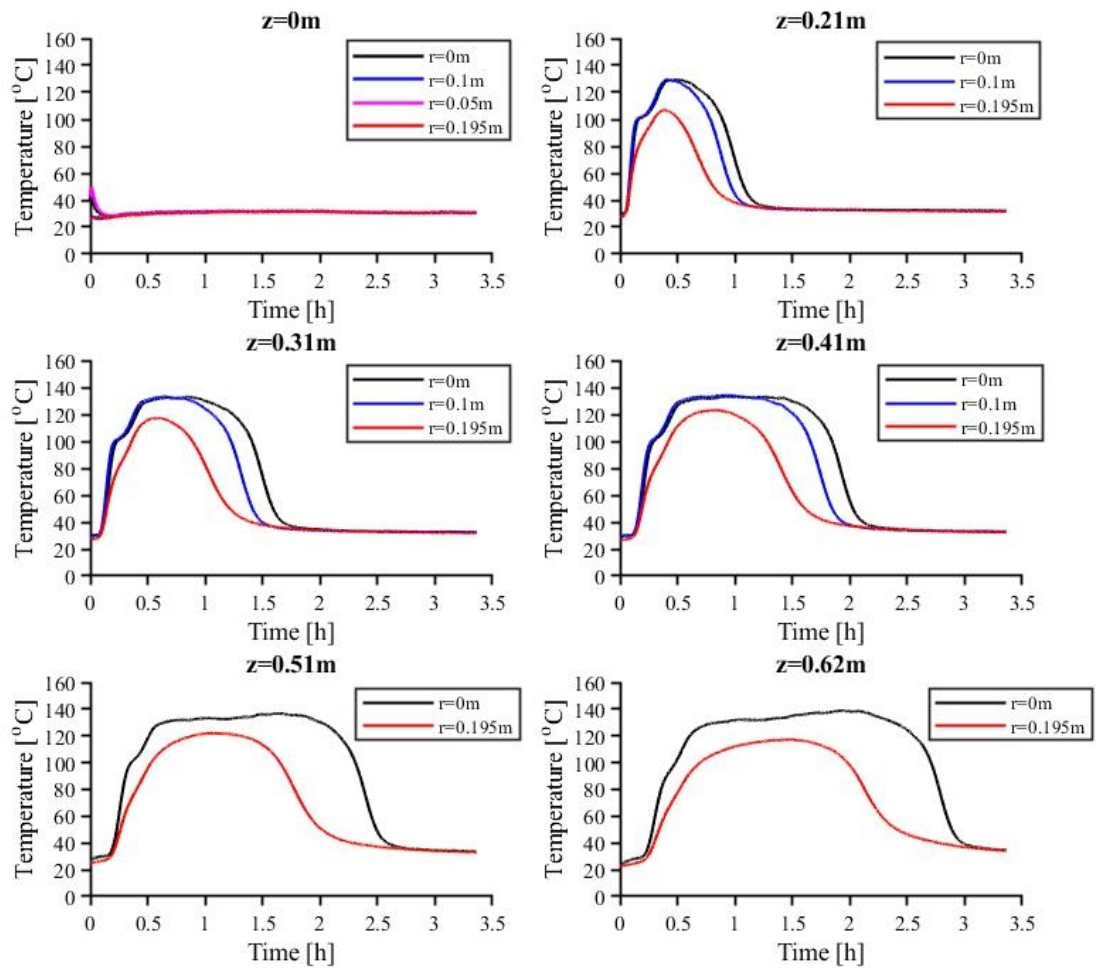


Figure 5-9: Radial temperature profiles at various bed depths (z) - Discharging cycle 1

The energy released during discharging cycle 1 is presented in Figure 5-10. The curve can be split into 4 regions as shown in Figure 5-10.

First region

Between $t = 0$ h and $t = 0.4$ h no energy was released from the bed since the adsorption front was at top of the bed and the sensible heat transferred to the air stream was used to heat up the zeolite layers below it.

Second region

Between $t = 0.4$ h and $t = 0.8$ h energy started being released but the zeolite layers at the lower layers of the packed bed were still being heated by the sensible heat from the upper layers undergoing adsorption.

Third region

Between $t = 0.8$ h and $t = 2.6$ h the entire packed bed was heated and therefore most of the heat released, from the layer undergoing adsorption, was transferred to the air stream. This resulted in almost a constant energy release from the bed during this period.

Fourth region

Between $t = 2.6$ and $t = 3.3$ h, the adsorption process neared completion and the heat transfer to the air stream was mainly due to the sensible heat at the lower layers of the packed bed. However, the energy steadily decreased, since the incoming air was cold, until the lowest layer cooled. A maximum of 5.3 kW was released during discharging cycle 1. By integrating the curve, the total energy discharged was 11.56 kWh.

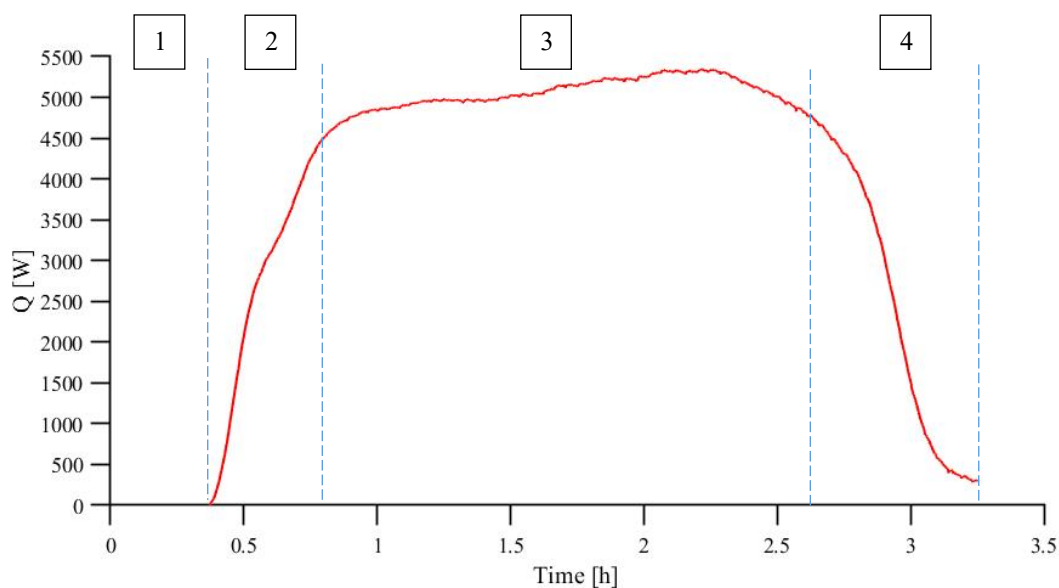


Figure 5-10: Heat released - Discharging cycle 1

5.2.2 Discharging Cycles 2 and 3 (70% and 25% RH)

Discharging cycles 2 and 3 were performed at lower values of relative humidity compared to discharging cycle 1 i.e., 70% and 25% RH compared to 100% RH in discharging cycle 1. The inlet and outlet temperatures for the first 3 discharging cycles are plotted on the same axis (in Figure 5-11) to clearly illustrate the effect of inlet humidity on the adsorption/ discharging cycle. It was observed that the temperature lift (from inlet to outlet) is directly impacted by the specific humidity of the inlet air. Furthermore, the time cycle duration is extended at lower values of RH. This is due the lower moisture content in the air which increases the time taken to completely saturate the zeolite. It should be noted that very low humidities also affect the amount of energy released from the packed bed. The data for discharging cycles 1 to 3 is summarized in Table 5-2 whilst Appendix B can be accessed for more detail. However, the curves follow very similar trends of temperature versus time at the various depths within the bed and therefore, the explanations for discharging cycle 1 also applies essentially to the performance of the other discharging cycles.

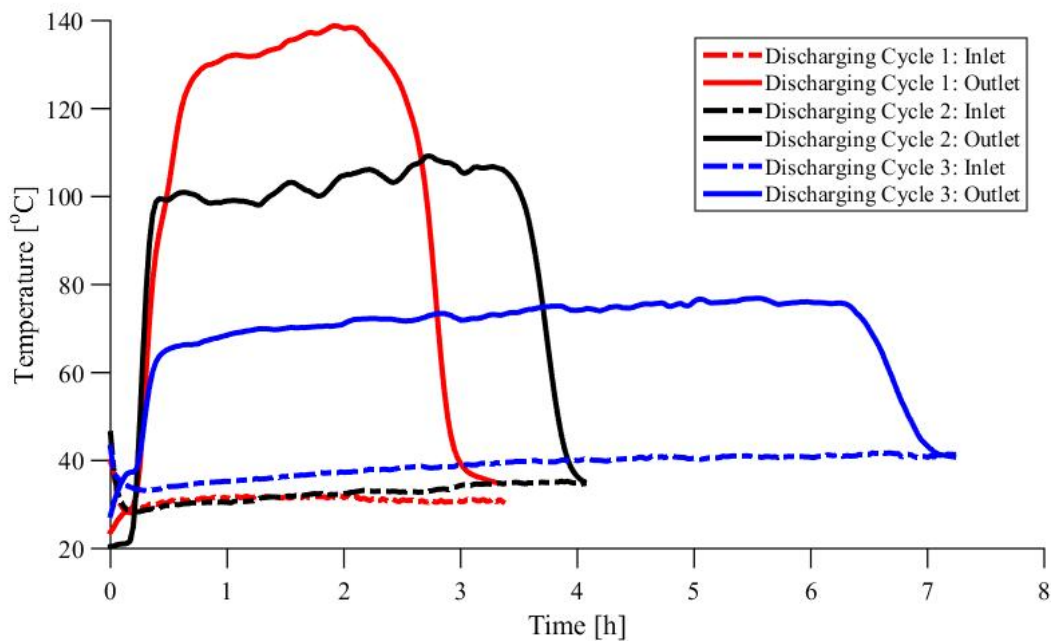


Figure 5-11: Packed bed inlet and outlet temperatures - Discharging cycles 1- 3

5.2.3 Discharging Cycles 4 and 5 (70% and 50% Flowrate)

For discharging cycles 4 and 5 the flowrate was lowered to 70% and 50% (of the maximum) respectively. Since the inlet humidity for discharging cycle 2 was similar, it was decided to compare discharging cycles 4 and 5 to discharging cycle 2. The inlet and outlet temperatures for these 3 tests are plotted in Figure 5-12. As expected, the lower flow rate increases the cycle time since the adsorption rate is lower i.e., less water is being adsorbed by the bed per unit time. The temperature lift

is noticeably higher for discharging cycle 2. This can be attributed to the slightly higher humidity of 26 g_w/kg_{da} compared to 23 g_w/kg_{da} and 24 g_w/kg_{da} for discharging cycle 4 and 5, respectively. However, when comparing discharge discharging cycle 4 and 5, the temperature lift for discharge cycle 4 is higher although the specific humidity for discharge cycle 5 is higher. This implies that the flow rate does affect the temperature lift slightly. The results also indicate that a lower flow rate influences the time taken for the outlet temperature to increase. This is because the flow rate affects the rate at which the thermocline moves along the height of the reactor. It should be noted that difficulties were experienced in controlling the humidity during discharging cycle 5 which was due to a significant change in ambient humidity during the cycle. This has resulted in a significant drop in temperature between t = 1.5 h and t = 4 h. The lower flow rates also affected the amount of energy released from the packed bed as only 10.19 and 10.48 kWh were released for discharging cycles 4 and 5 compared to 11.50 kWh for discharging cycle 2.

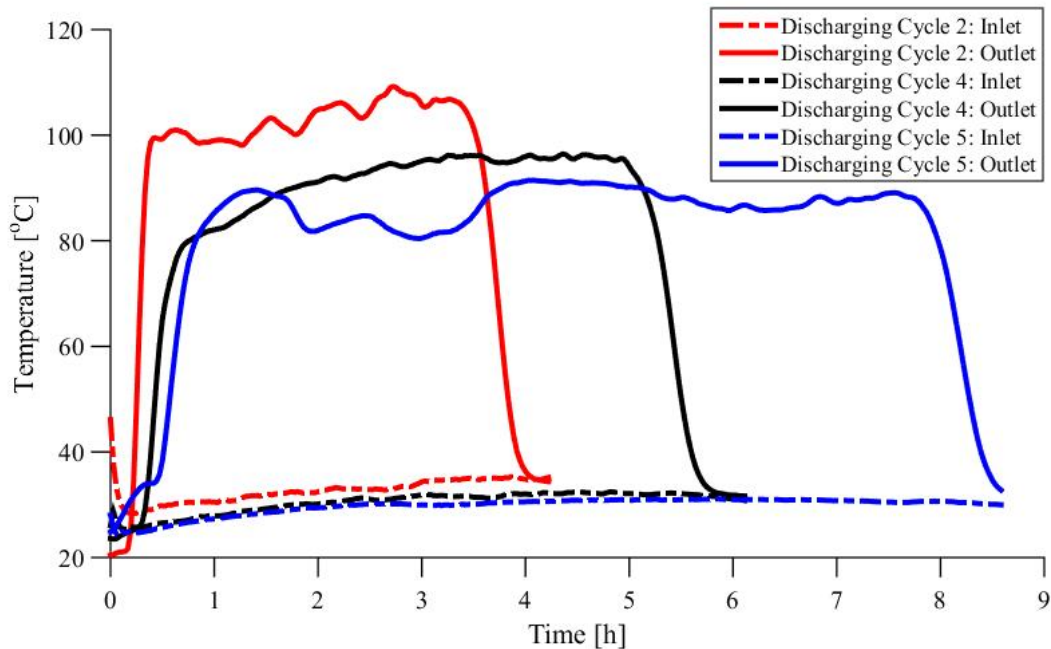


Figure 5-12: Packed bed inlet and outlet temperatures - Discharging cycles 2,4 and 5

5.2.4 Discharging Cycles 6 and 7 (160 °C and 130 °C Regeneration Temperature)

Discharging cycles 6 and 7 were performed after the packed bed was regenerated at 160 °C and 130 °C respectively compared to 200 °C in the previous 5 tests. Since the humidity was different for discharging cycles 6 and 7 it was decided to compare each of these tests with the cycle that had a regeneration temperature of 200 °C but with similar humidity, flow rate and cycle time. Therefore, discharging cycle 6 was compared with cycle 2 (refer to Figure 5-13) and discharging cycle 7 was compared to cycle 3 (Figure 5-14).

For cycle 6 the temperature lift was 58 °C (average humidity of 19 g_w/kg_{da}) compared to 75 °C (average humidity of 26 g_w/kg_{da}) for cycle 2. This matches the trend seen in discharging cycles 1 to 3

where the temperature lift during discharging was strongly influenced by the humidity in the incoming air. Similarly, for cycle 6 the temperature lift was 28 °C (average humidity of 7 g_w/kg_{da}) compared to 38 °C (average humidity of 12 g_w/kg_{da}) for cycle 2. However, a lower humidity should increase the cycle time noticeably which is not observed in both these cases. This implies that more heat is released when the packed bed is regenerated at higher temperatures. This is further supported by the amount of energy released i.e., 11.50 kWh and 10.73 kWh for discharging cycles 2 and 6 respectively; and 10.20 kWh and 7.50 kWh for discharging cycles 3 and 7 respectively. Therefore, higher charging/ regeneration temperatures make the packed bed drier, which allows more water vapour to be adsorbed during discharging and hence more energy is released.

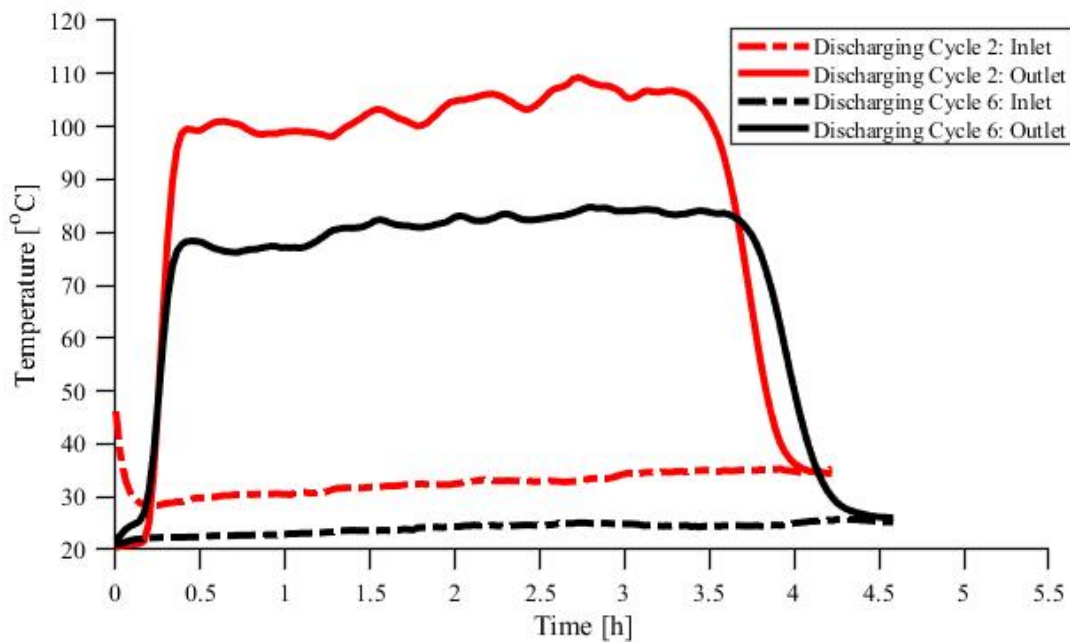


Figure 5-13: Packed bed inlet and outlet temperatures - Discharging cycles 2 and 6

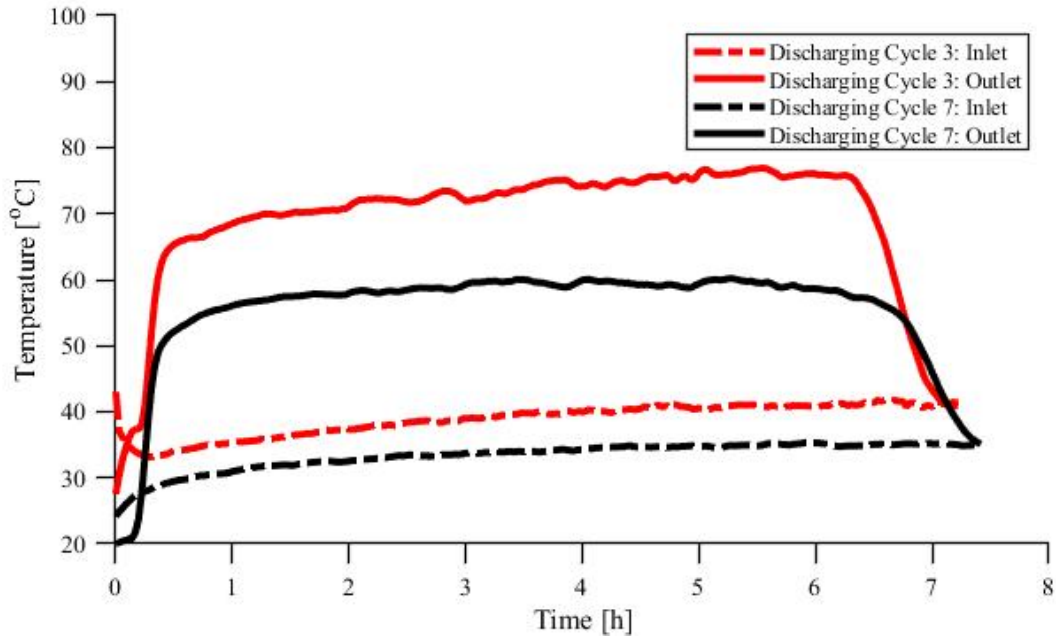


Figure 5-14: Packed bed inlet and outlet temperatures - Discharging cycles 3 and 7

5.2.5 Discharging Cycle 8: 5 months after regeneration

This test was conducted just after the national Covid-19 lockdown was eased. The bed was charged approximately 5 months prior to this test and the zeolite was left standing in the reactor which is an open sorption system i.e., the upper and lower layers of zeolite were exposed to the surrounding air and would have adsorbed water vapour. The temperature profiles at the centre of the reactor are presented in Figure 5-15. The maximum temperature realised across the reactor was 80 °C which is a temperature increase of 52 °C which is significantly high considering that the energy was stored for 5 months. The cycle lasted for 5 hours which was consistent with other tests with similar humidity. The slight dip in temperature at $t = 2.2$ h was due to a decrease in humidity, at the inlet, caused by the humidifier water level dropping too low before being refilled. The water level in the humidifier was controlled manually.

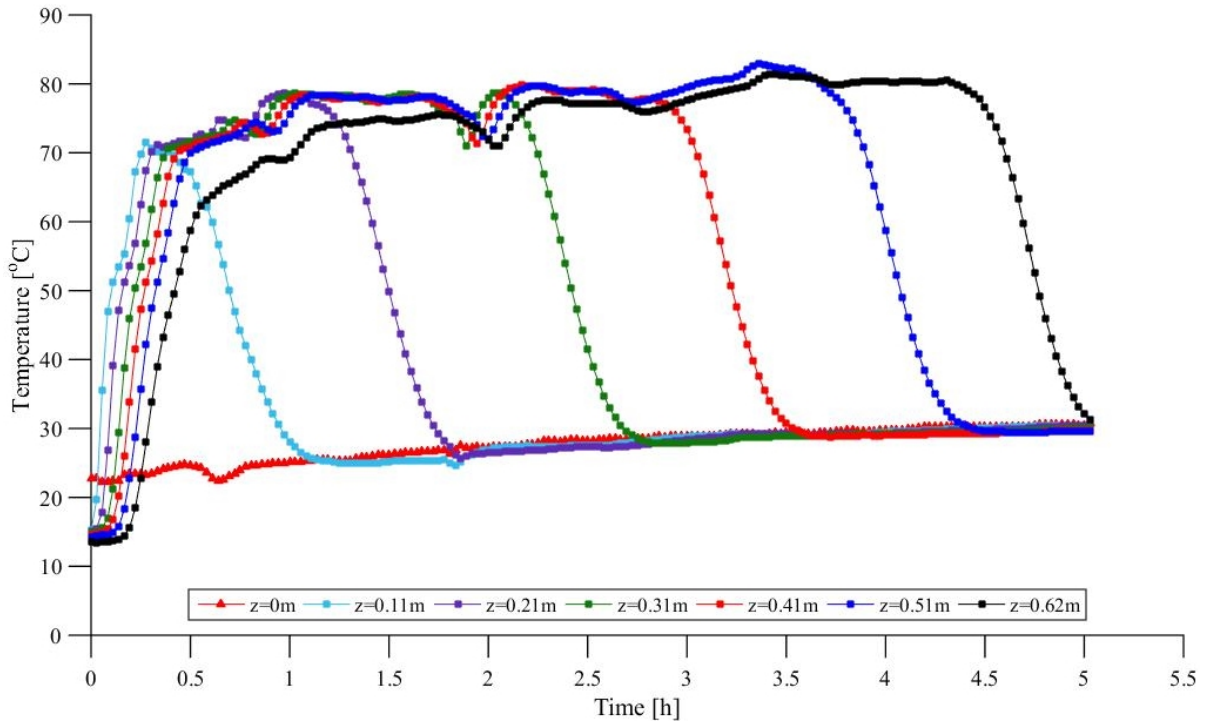


Figure 5-15: Axial temperature profiles at various bed depths (z) - Discharging cycle 8

The energy released during discharging cycle 8 is presented in Figure 5-16. A maximum of 2.3 kW was released during discharging cycle 8. The total energy discharged was 9.83 kWh which is noteworthy. This is 85% of the maximum amount of energy released (during discharging cycle 1). This implies that zeolite 13X can store heat for the long term with minimal losses.

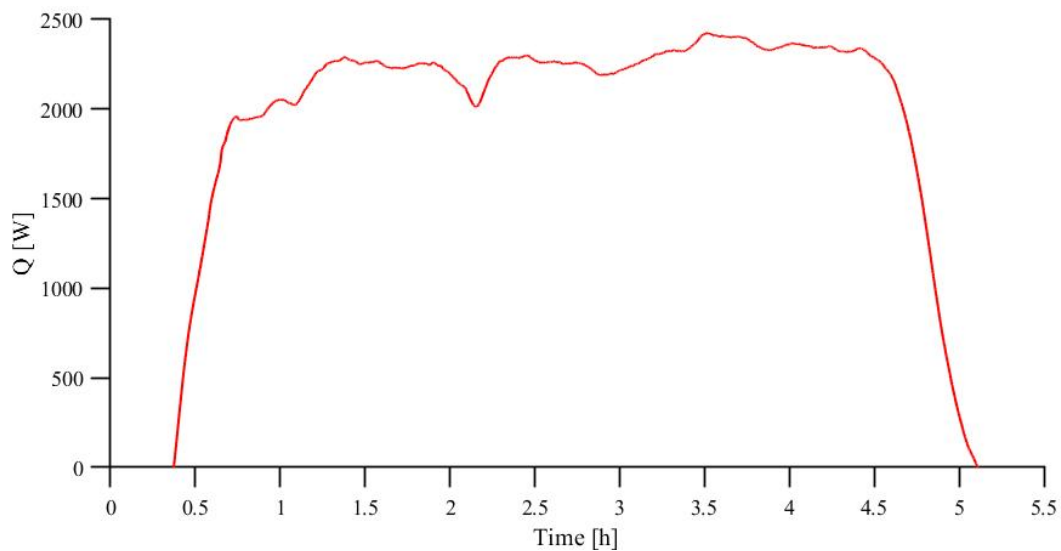


Figure 5-16: Heat released - Discharging cycle 8

5.3 Additional Charging/Discharging Results

5.3.1 Charging cycle after partial discharge

The axial temperature profiles for a charging cycle, that was done after the bed was partially discharged/ saturated in the previous test, are presented in Figure 5-17. It appears that the last 2 layers of the packed bed were dry (from 0.51 m to 0.62 m) since the temperature initially reached 180 °C at the start of the test. This is due to water released from the upper layers being adsorbed by these 2 layers and hence energy being released. Once these 2 layers were saturated (and adsorption process completed) their temperature decreased to 45 °C. After desorption was completed on the upper layers, the lower layers were eventually dehydrated and the charging cycle was completed. The cycle lasted approximately 3.5 hours like the previous tests. This showed that no significant time is saved if the bed is partially saturated since the layers that are dry will undergo adsorption/saturation, during the charging cycle, and will still require dehydration. However, this is due to the current setup where charging and discharging occur in the same direction. The flow direction should be reversed for discharging to prevent this problem. Since the bottom 2 layers undergo adsorption, this test also shows that temperatures close to the regeneration temperature are attainable (during discharging) at very high specific humidities.

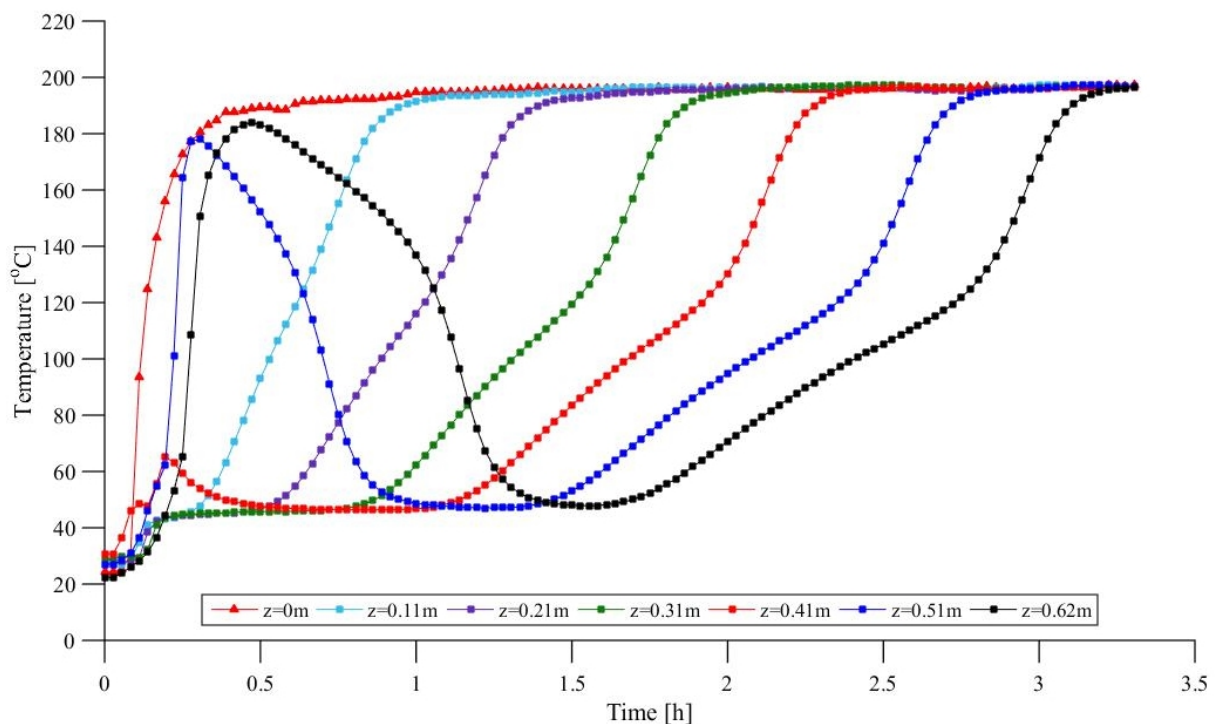


Figure 5-17: Axial temperature profiles at various depths (z) – Charging after partial discharge

5.3.2 Discharging cycle including sensible heat

The axial temperature profiles for a charging cycle, followed by an immediate discharging cycle, are presented in Figure 5-18. Due to an interruption in power supply, data from the entire cycle is not available. However, this test was included to illustrate what happens when discharging immediately follows the charging process. The temperature of the packed bed inlet ($z = 0$ m) immediately starts to decrease (at $t = 1.75$ h), when the charging process is completed and the discharging process starts, due to an inflow of cool/ ambient air. Initially the energy released is the sensible heat from the charging cycle. As the sensible heat from the charging process is lost to the air stream, adsorption begins on the upper layers and subsequent layers start to cool until the adsorption temperature is reached (approximately 80 °C in this case). The adsorption process maintains the outlet temperature at 80 °C until all the energy is released from the packed bed and the outlet ($z = 0.62$ m) cools to ambient temperature.

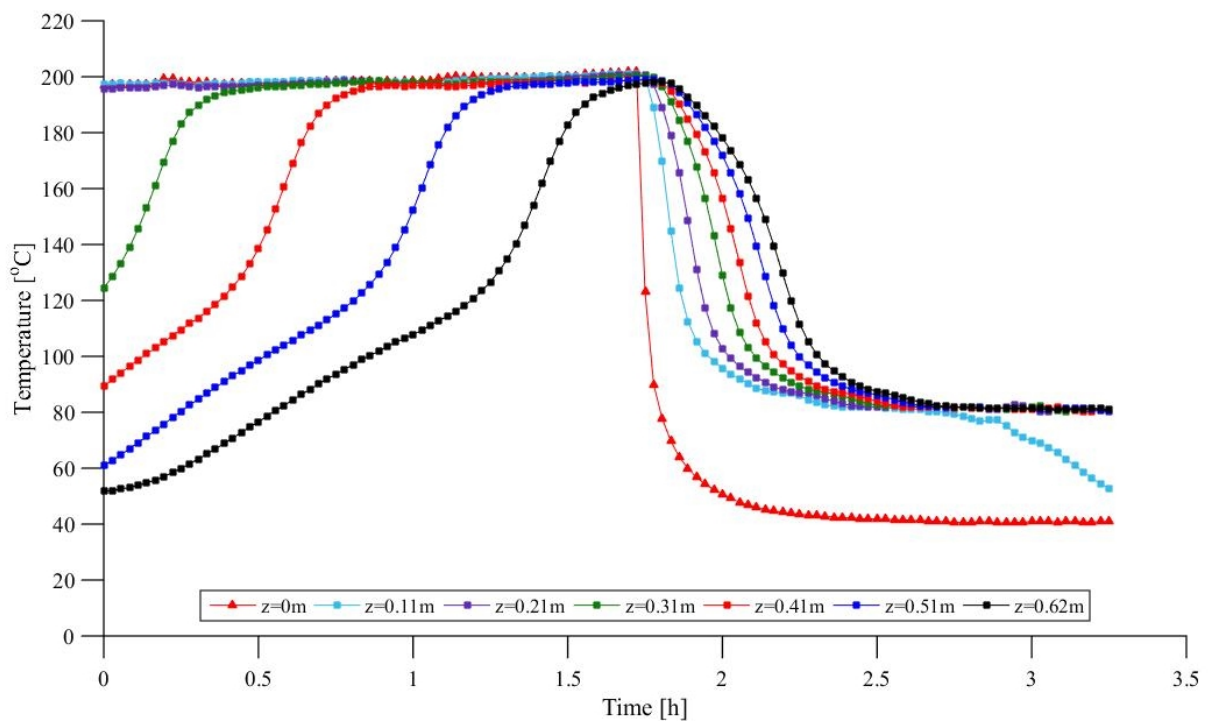


Figure 5-18: Axial temperature profiles at various depths (z) - Discharging following Charging

5.4 Drying Ceramic Casting Moulds

This section describes the apparatus and method used to test the drying rate of ceramic casting moulds using the hot air exiting the zeolite reactor. The results are presented and discussed.

5.4.1 Apparatus and Method

A subsystem was added to the zeolite test facility which consists of a kiln (refer to Figure 5-19) and a butterfly valve to control the temperature of the air going into the kiln to dry the ceramic. The kiln

was modified to include a support with holes (refer to Figure 5-20), to allow air to flow around the moulds, to increase the drying rate. The support was placed on a mass balance to record the change in mass of the ceramic casting moulds.



Figure 5-19: Kiln



Figure 5-20: Ceramic Moulds in Kiln

The air exiting the packed bed is usually greater in temperature than the required 60 °C (depending on the specific humidity at the inlet of the packed bed) for drying the ceramic moulds. To lower and precisely control the temperature of the air entering the kiln, a butterfly valve was used to add ambient air to the air exiting the zeolite reactor. The butterfly valve was designed and manufactured at CSIR.

A geared motor was attached to the valve to control its opening and closing. Temperature transmitters were used to convert the temperature reading in the kiln into an electrical signal proportional to the temperature. This was then read by a PLC and used to adjust the opening of the butterfly valve by the geared motor to maintain the desired temperature in the kiln. A graphic representation of the system is shown in Figure 5-21 .

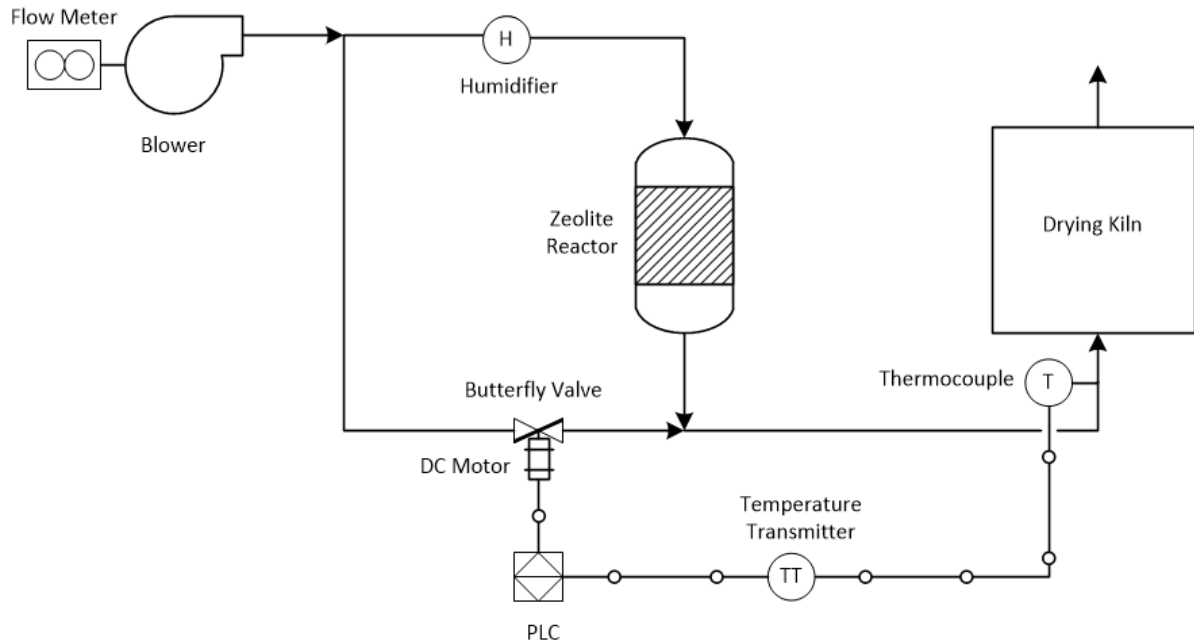


Figure 5-21: Butterfly Valve Temperature Control System

5.4.2 Results: Controlling Kiln Temperature

The temperature profiles at the centre of the bed and the inlet of the kiln are presented in Figure 5-22. The butterfly valve was successful in maintaining the temperature of the kiln at 60 °C. The reactor also contained enough energy for the kiln to be operated for approximately 7.5 hours at this temperature.

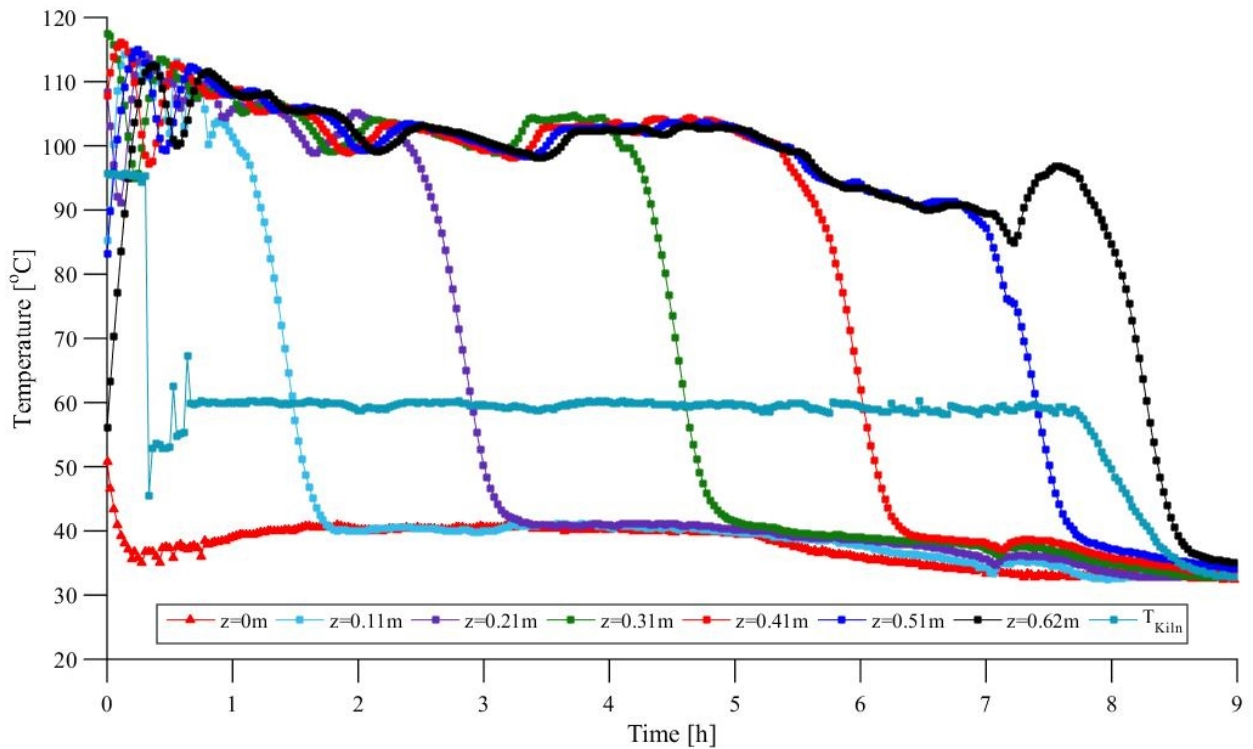


Figure 5-22: Axial temperature profiles at various bed depths (z) and inlet temperature of kiln

The humidity and mass flow rate were recorded and presented in Figure 5-23. The inlet humidity was approximately $23 \text{ g}_w/\text{kg}_{\text{da}}$. The humidity at the outlet of the reactor (inlet to the kiln) was approximately $2 \text{ g}_w/\text{kg}_{\text{da}}$. This is suitable for drying the moulds since Plaster of Paris is porous and may crack at extremely low humidities [46]. The mass flow rate was approximately 174 kg/h for the cycle although not all the mass flow goes through the packed bed. A large fraction of the air bypasses through the control valve to maintain the temperature at $60 \text{ }^\circ\text{C}$.

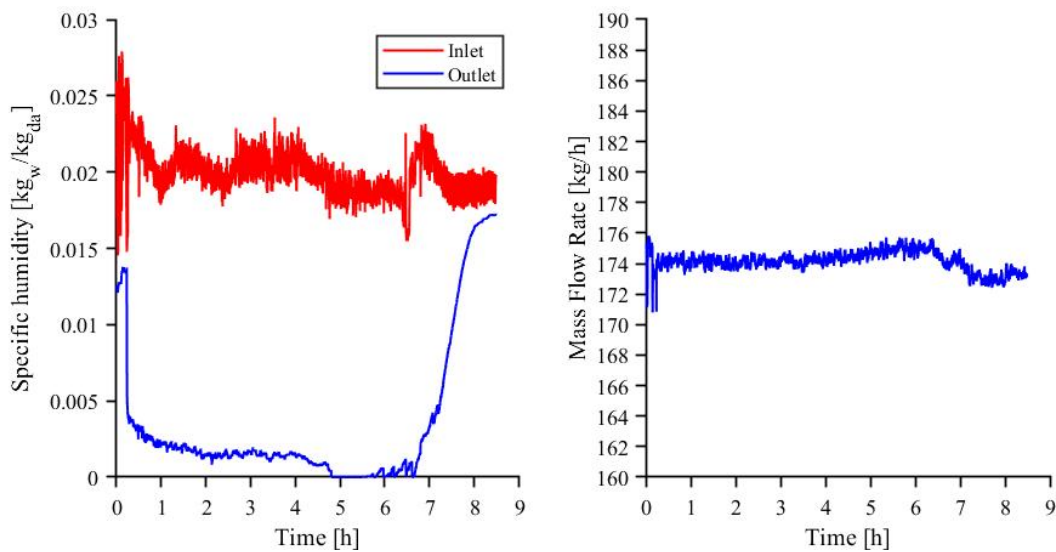


Figure 5-23: Humidity and Mass flow rate

5.4.3 Results: Drying Tests

The cumulative mass of water evaporated, from the casting moulds, for the two drying tests are shown in Figure 5-24 . Fifteen ceramic casting moulds were used and 300 ml of water was poured into each mould. The total mass of water was therefore 4.5 kg. For the first test, approximately 0.784 kg of water was evaporated after 5.5 hours. This equates to an average drying rate of 0.261 kg/h. To improve the drying rate, an axial fan was installed inside the kiln to swirl the air flow around the moulds for the second test. After 3 hours, approximately 2 kg of water was evaporated. This equates to an average drying rate of 0.667 kg/h. The drying rate improved by almost 3 times after introducing the axial fan to swirl the flow.

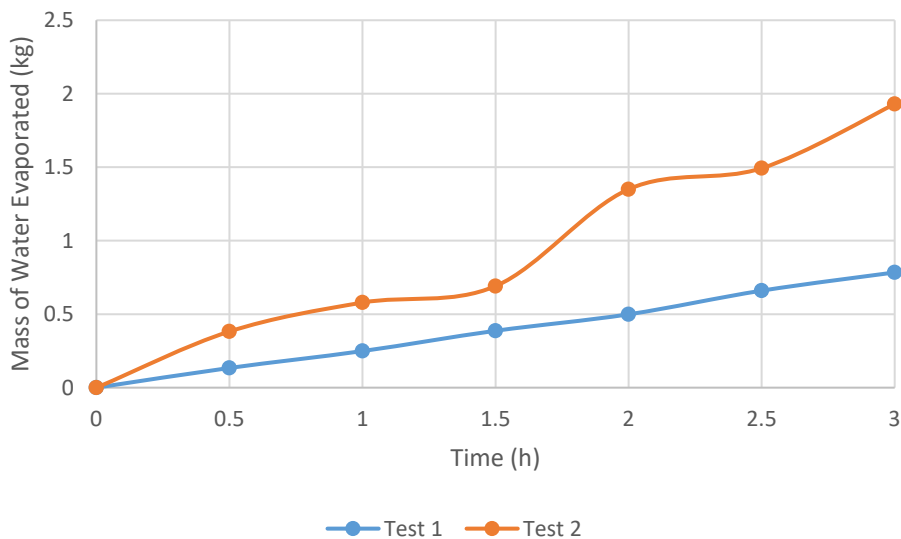


Figure 5-24: Cumulative mass of water evaporated from ceramic casting moulds: Drying Test 1

5.5 Moisture Adsorption Capacity of Zeolite 13X at Different Relative Humidities

This section describes the apparatus and method used to determine the amount of water that can be absorbed by zeolite 13X at different relative humidities. The results are presented and discussed.

5.5.1 Apparatus and Method

A small pipe section with a mesh (at the bottom) was manufactured (refer to Figure 5-25) to test the amount of water that can be adsorbed by 1 kg of zeolite 13X at different relative humidities. A humidity chamber that was designed to test solar panels was utilised to control the relative humidity of the air supplied to the zeolite sample. A blower was placed inside the solar humidity chamber (refer to Figure 5-26) to suck the air from the chamber at different relative humidities and supply it to the

zeolite sample. Once the adsorption process of the zeolite was completed, the sample was weighed to determine the mass of water adsorbed at each relative humidity set point.



Figure 5-25: kg Sample Test Section



Figure 5-26: Blower Placed in Humidity Chamber

5.5.2 Results

To determine the amount of water that can be adsorbed at different humidities, five tests were performed on 1 kg samples of zeolite 13X at 10,20,30,50 and 85% relative humidity at 55 °C. A set point 55 °C was chosen to allow the widest range of humidity (i.e., 10-85%) that can be achieved by the chamber. The results are presented in Figure 5-27. The amount of water that can be adsorbed ranged from 216 g_w/kg_{zeolite} (21.6%) at 10% relative humidity to a maximum of 286 g_w/kg_{zeolite} (28.6%). The results are close to the value mentioned on the data sheet [35] i.e., 28.5% water adsorption at 75% relative humidity. It should be noted that the controller was struggling to keep the

humidity constant, inside the chamber, in the 10-30% relative humidity range since the chamber was designed for circulating air around solar panels and not for sucking air out of it.

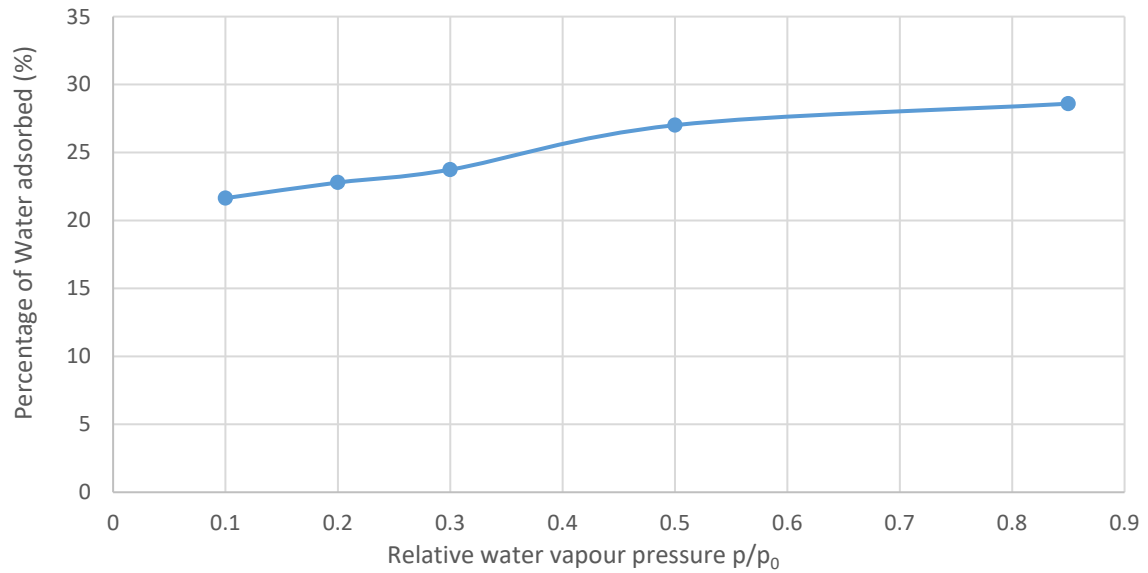


Figure 5-27: Percentage of water adsorbed at different relative humidities

6 Performance Analysis of Experimental System

According to Hauer [47] some of the important parameters for evaluating the performance of an adsorption system include energy efficiency, temperature lift, energy storage capacity and moisture adsorption capacity. Calculations for these parameters were done in this section based on previous studies and numerical models. The calculated values were then compared to the experimental results to determine the performance of the experimental system.

6.1 Energy Efficiency of System

6.1.1 Introduction

The energy efficiency is one the most important parameters of the system. It can give the user an indication of whether this type of system is feasible to implement for a particular industrial process. In this section, a detailed analysis of the energy efficiency is presented with respect to the three main parameters that were varied during testing i.e. regeneration temperature, humidity and flow rate.

6.1.2 Calculations

The amount of energy supplied, stored, and released (obtained from Section 5.1 and 5.2) for each cycle is summarised in Table 6-1. The energy supplied is the total energy input to the packed bed during charging. The energy stored is the amount of energy absorbed during charging and the energy released is the amount of energy released during discharging/ adsorption. The efficiencies are calculated based on the equations in Section 4.3. A sample calculation for each of these efficiencies has been included in Appendix C. It should be noted that the charging cycles performed at 200 °C were almost identical and therefore the one test (charging cycle 1) was used to determine the efficiencies for all the cycles that were regenerated at 200 °C.

Table 6-1: Efficiencies from Charging and Discharging cycle results

Cycle No.	Energy Supplied (kWh)	Energy Stored (kWh)	Energy Released (kWh)	Charging Efficiency (%)	Storage Efficiency (%)	Overall Efficiency (%)
1	20.44	13.64	11.56	67	85	57
2	20.44	13.64	11.50	67	84	56
3	20.44	13.64	10.20	67	75	50
4	20.44	13.64	10.19	67	75	50
5	20.44	13.64	10.48	67	77	51
6	22.45	11.99	10.73	53	90	48
7	24.69	10.47	7.50	42	72	30
8	20.44	13.64	9.83	67	72	48

The three chosen parameters (humidity, mass flow rate and regeneration temperature) parameters are plotted (Figure 6-1) against the storage efficiency of the system. From Table 6-1 and Figure 6-1 it can be seen that the humidity affects the storage efficiency and hence the overall efficiency. As the humidity was decreased from cycles 1 to 3, these efficiencies also decreased. This differs from the results of Djaeni et al [38] (Section 2.5.2) which indicate that humidity does not affect efficiency. However, it should be noted that at lower humidities, the cycle time is increased and this will lead to greater heat losses through the reactor wall, which will affect the amount of energy released at the outlet. In discharging cycles 4 and 5 the humidity was increased (from cycle 3) however the flow rate was decreased and this affected the storage and overall efficiencies which were similar to cycle 3. The flow rate and hence adsorption rate affects the efficiency as mentioned by Gaeini et al [41] (Section 2.5.6). In discharging cycle 6, the regeneration temperature was lowered. this resulted in the highest storage efficiency (90%) since less energy was absorbed by the bed and the amount of energy discharged was relatively high. However, the overall efficiency was lower due to the lower charging efficiency. This was caused by losses to the atmosphere once the outlet temperature of the reactor started to increase as discussed in Section 5.1. Similarly, the losses to atmosphere were even higher for discharging cycle 7 resulting in the lowest charging and overall efficiencies, although the storage efficiency was comparable to cycles 3-5. Since discharging cycle 8 was performed 5 months after regeneration, the effect of parameters cannot be compared to the other cycles. However, this test was included to show that zeolite 13X can be used for long term storage with minimum losses since the energy efficiencies are relatively high. It should be kept in mind that the reactor was not sealed during this period. Therefore, the outer layers adsorbed water from the surrounding air, which affected the amount of energy released and hence the efficiency.

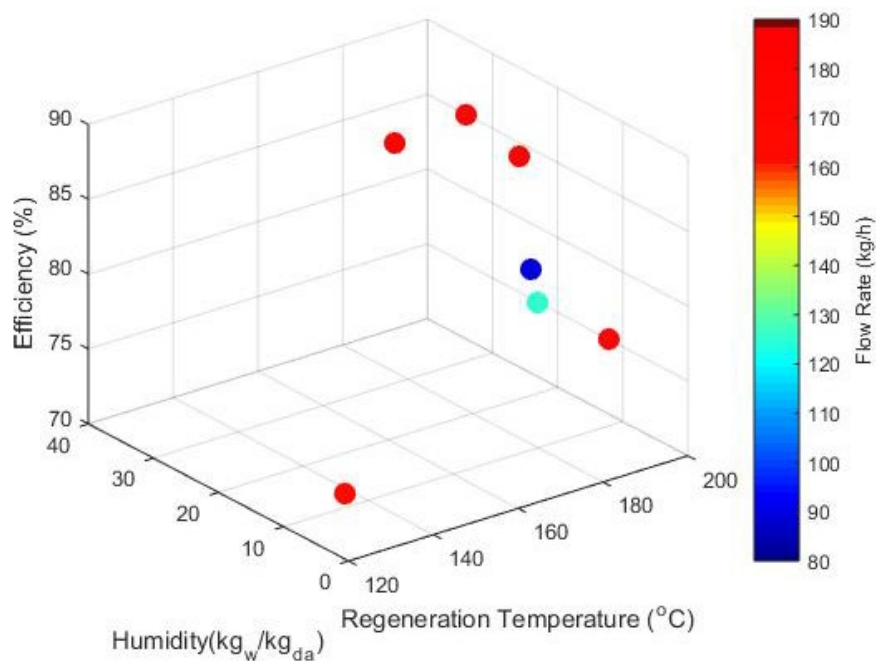


Figure 6-1: Storage Efficiencies for Cycles 1-7

For cycles 1 - 6 and cycle 8 the overall efficiencies ranged between 48-57%. This compares well with Djaeni et al [38] (Section 2.5.2) with overall efficiencies ranging between 50-55%. Cycle 7 was very low (33%) for the 130 °C regeneration temperature. However, this efficiency is strongly dependent on the charging efficiency and hence the charging efficiency needs to be improved. The maximum amount of energy absorbed from the energy supplied was 67% which occurred during charging cycle 1 (200 °C) with only 53% and 42% being absorbed during charging cycle 2 (160 °C) and 3 (130 °C) respectively. This efficiency can be increased by making the storage larger than needed and not allowing the outlet temperature to rise too high (as discussed in Section 5.1) to minimise losses to the atmosphere.

Another factor that affects the overall efficiency of the system is the sensible heat that is transferred to the zeolite particles during charging/regeneration. The focus of this work was on medium to long term storage for batch-wise processes. In batch-wise processes there is a mismatch between supply and demand of energy. A thermochemical system has the potential to ensure that energy is readily available when required, since the energy stored is not significantly affected by the time between charge and discharge cycles. To illustrate this concept, the bed was allowed to cool (to atmospheric temperature) before discharging and hence the sensible heat was lost and not considered in the efficiency calculations in Table 6-1. However, if the bed is discharged immediately after charging, the overall efficiency will be higher. To evaluate the impact on the overall efficiency, the sensible heat was calculated for each cycle using equation (2-1) based on the mass of zeolite in the reactor, the effective specific heat of zeolite and the temperature difference between the regeneration temperature and ambient. The results are summarised in

Table 6-2. It is observed that by utilising the sensible heat (all other factors remaining constant), the maximum overall efficiency will increase from 57% to 70% which is comparable to a typical sensible heat storage system of 70% (Table 2-5).

Table 6-2: Overall efficiency with sensible heat included

Cycle	Q_{sens} (kWh)	Energy Released with Q_{sens} (kWh)	Energy Supplied (kWh)	Overall Efficiency with Q_{sens} (%)
1	2.70	14.26	20.44	70
2	2.70	14.20	20.44	69
3	2.70	12.90	20.44	63
4	2.70	12.89	20.44	63
5	2.70	13.18	20.44	64
6	2.16	12.89	22.45	57
7	1.62	9.12	24.69	37
8	2.70	12.53	20.44	61

6.1.3 Conclusion

This section presented a detailed analysis of the charging, storage and overall efficiency of the system for each cycle. Ways to improve these efficiencies were discussed. The maximum overall efficiency during testing was 57% for a regeneration temperature of 200 °C and a relative humidity of 100% during discharging. The humidity also affects the temperature lift which will be discussed in the next section.

6.2 Temperature Lift

6.2.1 Introduction

The temperature lift gives a good indication of the range of applications that zeolite 13X is suited to. In this section a method for theoretically calculating the temperature lift is provided which depends on the water content of the zeolite before adsorption. The Langmuir-Freundlich model [40] was used to calculate the water content. The equations and coefficients are provided in this section. A curve by Hauer [48] for the integral heat of adsorption is presented which is also required for calculating the temperature lift. The temperature lift was calculated for the eight cycles that were run (based on the input parameters) and compared to the experimental data.

6.2.2 Calculations

According to [48] the expected temperature lift (ΔT) across the packed bed can be calculated by equation (6-1). The calculated value depends on the humidity difference between the inlet and outlet of the packed bed during adsorption/discharging, the integral heat of adsorption and the water content of the zeolite before and after adsorption.

$$\Delta T_{calc} = \Delta x \cdot \frac{\Delta H_{ads}(C_{des})}{c_{air} - \frac{\Delta x}{\Delta C} \cdot c_{sorb,eff}} \quad (6-1)$$

To proceed with equation (6-1), the water content before and after adsorption must be calculated. This can be done using the Langmuir-Freundlich model [40]. The equations are as follows:

$$C = \frac{C_{max} b P^n}{1 + b P^n}; b = b_0 \exp(\Delta E / RT) \quad (6-2)$$

$$b = b_0 \exp(\Delta E / RT) \quad (6-3)$$

$$n = n_1 + \frac{n_2}{T} \quad (6-4)$$

The partial pressure (P_v) of the water vapour can be calculated by Dalton's law [15]:

$$P_v = \left(\frac{14x_{ha}}{9 + 5x_{ha}} \right) P_{amb} \quad (6-5)$$

The values for the coefficients are summarised in Table 6-3.

Table 6-3: Langmuir-Freundlich model coefficients

Coefficient	Value
C_{max}	18 (mol/kg)
b_0	0.000308 (1/Pa ⁿ)
ΔE	18016 (J/mol)
n_1	-0.3615
n_2	274.23 (K)
R	8.314 (J/K.mol)

The graph for the integral heat of adsorption for zeolite 13X is presented in Figure 6-2 [48]. After calculating the water content of the zeolite for each cycle, the value ΔH_{ads} was read of this graph at the water content before adsorption (C_{des}). It should be noted that the effective heat capacity of zeolite is 1.17 kJ/kg.K [48]. Using Equation (6-1) the expected temperature lift for each cycle based on the inlet humidity supplied to the packed bed was calculated. The calculated and experimental values are summarised in Table 6-4.

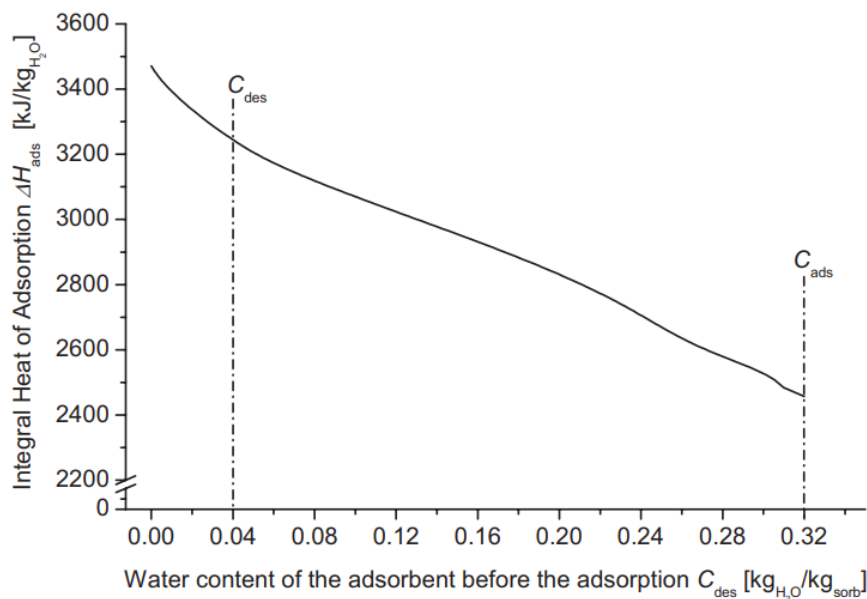


Figure 6-2: Integral heat of adsorption [48]

Table 6-4: Comparison of calculated and experimental temperature lift

Discharging cycle no.	Avg. inlet humidity (g _w /kg _{da})	C _{ads} (kg _w /kg _z)	C _{des} (kg _w /kg _z)	ΔH _{ads} (C _{des}) (kJ/kg.K)	Calculated ΔT (°C)	Experimental ΔT (°C)
1	34	0.316	0.043	3230	127.5	107
2	26	0.314	0.043	3230	93.8	75
3	12	0.304	0.043	3230	40.7	38
4	23	0.314	0.043	3230	81.8	65
5	24	0.314	0.043	3230	85.8	60
6	19	0.316	0.074	3130	65.0	58
7	7	0.303	0.121	3020	22.0	28
8	20	0.315	0.043	3230	70.2	53

The experimental and calculated temperature lift are plotted on the same axes in Figure 6-3. Discharging cycle 8 was not plotted as there was a period of 5 months between the charging and discharging cycles and the zeolite was not vacuum sealed. This could have led to inaccurate results due to a higher water content (C_{des}) before adsorption. The temperature lift is directly proportional to the specific humidity at the inlet of the packed bed as seen in in Figure 6-3. This was also observed by Mette et al [5] (section 2.6.3) and Tatsidjodoung et al [15] (Section 2.6.4). Difficulties were experienced when trying to control the humidity during discharging cycle 5 (24 g_w/kg_{da}). This could have led to the value being lower than expected.

At lower humidities (below 20 g_w/kg_{da}) the experimental values differ by a maximum of 7 °C from the calculated values. At higher humidities (above 20 g_w/kg_{da}) the maximum deviation between the experimental and calculated values was 20.5 °C. However, at higher temperatures, heat losses (from the experimental rig) to the atmosphere are expected to be greater. Furthermore, at higher humidities water condenses on the humidity sensors which may have caused it to indicate a higher value than the actual value. These two factors contribute to the deviation between the experimental and calculated values.

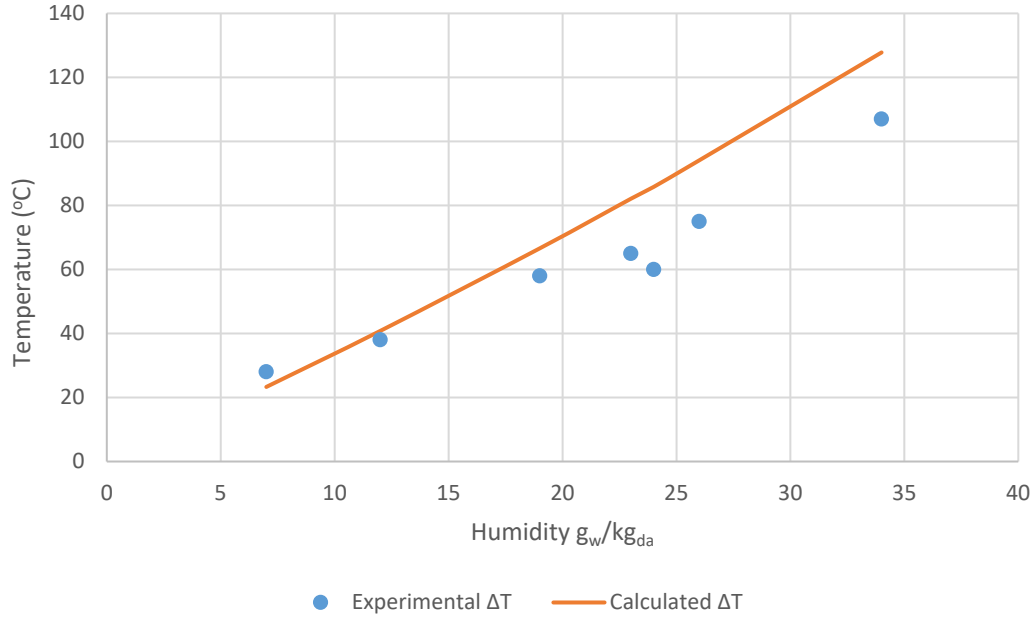


Figure 6-3: Experimental and calculated temperature increase of zeolite 13X at different humidities

6.2.3 Conclusion

This section presented a method for theoretically calculating the temperature lift. The equations and coefficients were provided. The temperature lift was calculated and compared to the experimental data. It was shown that the temperature lift is directly proportional to the specific humidity at the inlet of the packed bed during discharging.

6.3 Energy Storage Capacity

6.3.1 Introduction

The energy storage capacity is an important factor to consider when sizing the reactor for different applications. The equations and the curve for the differential heat of adsorption [48] is presented which are required to calculate this parameter. The experimental results are compared to the calculated values as well as the values provided by ZAE Bayern [49].

6.3.2 Calculations

The volume of the reactor is 0.0779 m^3 and hence the mass of zeolite 13X is approximately 47.5 kg based on the bulk density of 610 kg/m^3 (Table 2-8) which includes the void fraction. According to Hauer [47] the energy density of the system can be calculated using the following equations:

$$\frac{m_{zeolite}(Q_{cond}+Q_{bind})}{V_{zeolite}} = \rho_{zeolite}(Q_{cond}+Q_{bind}) \quad (6-6)$$

$$Q_{cond} = (C_{ads} - C_{des})L(T) \quad (6-7)$$

$$Q_{bind} = \int_{C_{des}}^{C_{ads}} \Delta H_d dC - Q_{cond} \quad (6-8)$$

The energy of binding (Q_{bind}) and the energy of condensation (Q_{cond}) can be calculated by integrating the differential heat of adsorption curve in Figure 6-4. This was done in MATLAB for each cycle based on the water content calculated in Table 6-4. This curve shows that the heat of adsorption depends on the water content of the zeolite before adsorption and the uptake of water after adsorption.

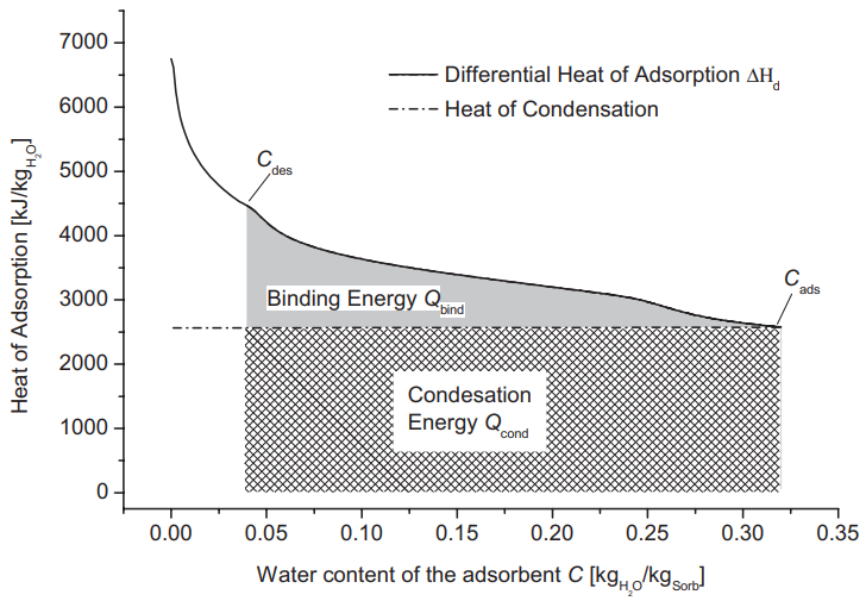


Figure 6-4: Differential heat of adsorption [48]

The energy density was calculated for each cycle (from the equations above) and compared to the experimental results in Table 6-5. The experimental results agree within 10% of the calculated results for discharging cycles 1-7. For discharging cycle 8 the deviation was 16% as expected, since the time between regeneration and discharging was 5 months. From the calculated and experimental results, it is observed that the regeneration temperature is the main factor that affects the storage energy density. The results also show that the humidity affects the storage capacity to a certain extent, However the calculated results do not take into consideration the effect of the flow rate which was seen in the experimental results. A lower flow rate lowered the storage energy density.

Table 6-5: Calculated and Experimental Energy Density

Cycle	Q_{cond} (kJ/kg)	Q_{bind} (kJ/kg)	Experimental energy released (kWh)	Calculated energy density (MJ/m ³)	Calculated energy density (kWh/m ³)	Experimental energy Density (kWh/m ³)
1	702.99	180.64	11.56	539	149.73	148.33
2	698.44	185.18	11.50	539	149.73	147.63
3	671.84	171.09	10.20	514	142.83	130.87
4	699.20	184.42	10.19	539	149.73	130.80
5	699.78	183.85	10.48	539	149.73	134.49
6	623.57	134.53	10.73	462	128.46	137.76
7	469.50	67.53	7.50	327	91.00	96.30
8	700.87	182.75	9.83	539	149.73	126.10

The energy released for the three regeneration temperatures are summarised in Table 6-6 for the reactor. The energy stored per ton of zeolite 13X was calculated and compared to the values calculated by ZAE Bayern [49].

Table 6-6: Energy stored at different regeneration temperatures

Cycle no.	Regeneration Temperature (°C)	Relative Humidity (%)	Energy released (kWh)	Energy released (kWh/ton)	Energy released (kWh/ton): ZAE Bayern [49]
1	200	100	11.56	243	255
6	160	86	10.73	226	228
7	130	20	7.50	158	189

The experimental values were plotted on the same set of axes as the values provided by ZAE Bayern [49]. For a regeneration temperature of 200 °C and 160 °C the experimental and calculated values agree within 5%. However, there was a deviation of 16% at a regeneration temperature of 130 °C. This is due to the low relative humidity (of 20%) at which the packed bed was discharged after regeneration at 130 °C. The values calculated by ZAE Bayern [49] used a relative humidity of 95%. From the results in this figure, it can be deduced that the regeneration temperature as well as the relative humidity during discharging strongly affects the storage capacity. Furthermore, a maximum of 255 kWh can be stored per ton after regenerating the zeolite 13X at 200 °C.

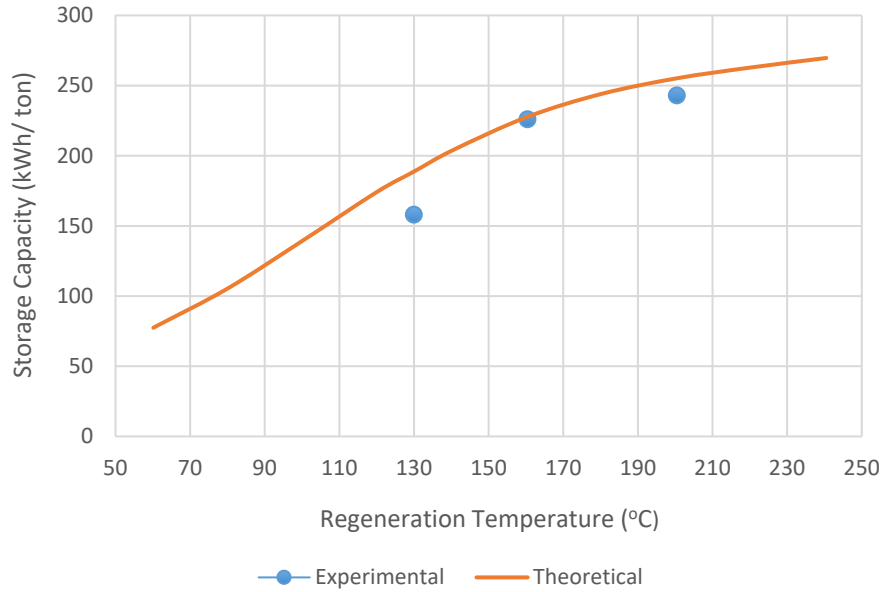


Figure 6-5: Experimental and calculated energy storage capacity of zeolite 13X [49]

6.3.3 Conclusion

This section provided equations to calculate the energy storage density of a zeolite TES system. The calculated values were compared to the experimental values. From these results it was shown that a maximum of 255 kWh can be stored per ton of zeolite 13X at a regeneration temperature of 200 °C. This equates to approximately 150 kWh/m³.

6.4 Moisture Adsorption Capacity

6.4.1 Introduction

The moisture content is an important parameter which was used to calculate the temperature lift and energy storage capacity (Section 6.2 and 6.3) of Zeolite 13X. It is therefore important to compare the experimental data to the calculated values and experiments in literature. This section compares the experimental data (presented in Section 5.5) to the Langmuir-Freundlich model [40] and experimental values generated by Bales et al [44].

6.4.2 Calculation

Calculations were done using the Langmuir-Freundlich model [40] (described in 6.2) to determine the water adsorption capacity of zeolite 13X. The calculated results are compared to the experimental results (refer to Figure 6-6) achieved during testing. A logarithmic curve was fitted to the experimental data points. From Figure 6-6 the maximum amount of water that can be adsorbed by zeolite 13X is approximately 30% or 300 g_w/kg_{zeolite} at a relative humidity of 100% and a temperature of 55 °C. The experimental results agree within 10% of the calculated values at relative humidities of 50% and 85%. However, there is a deviation of up to 20% between the calculated and experimental values between 10-30% RH. This could be due to the controller struggling to maintain lower

humidities in the chamber from which air was being sucked (as described in section 5.5.1). However, the general trend was still observed i.e., at higher relative humidities, the amount of water adsorbed was higher indicating that relative humidity affects the water adsorption capacity of zeolite 13X. The experimental values were also compared to calculations by Bales et al [44]. There was a better correlation between the experimental curve and the curve generated by Bales et al [44]. However. It should be noted that this curve was generated at a temperature of 40 °C, compared to the temperature of 55 °C used for the experimental and Langmuir-Freundlich model.

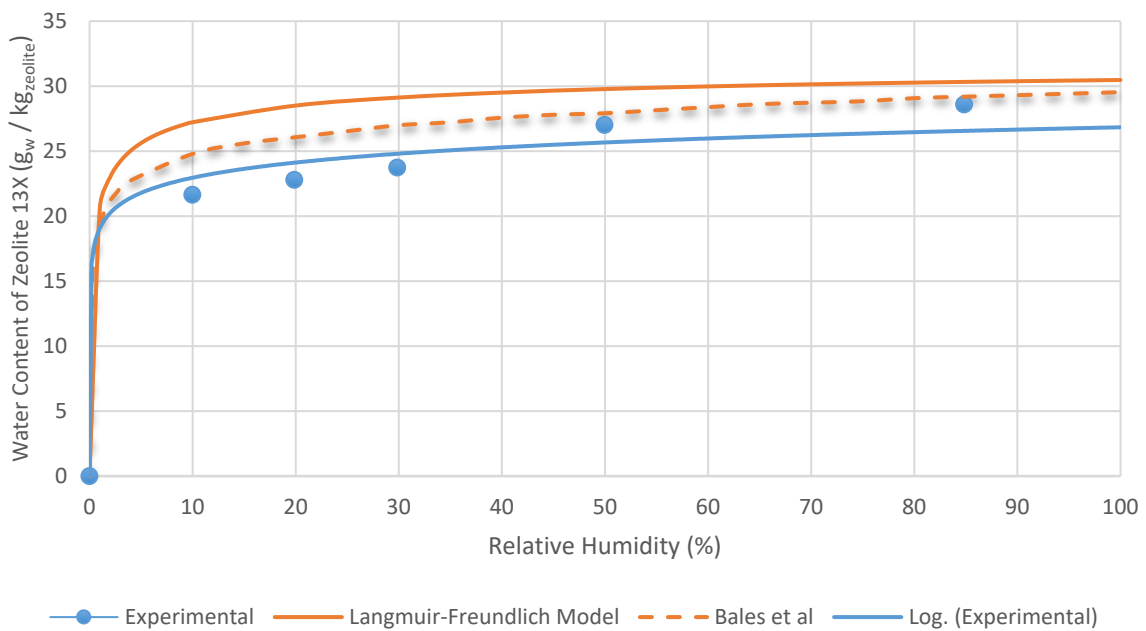


Figure 6-6: Experimental and calculated water adsorption capacity of zeolite 13X [44]

6.4.3 Conclusion

The experimental data matches the expected trend indicating that relative humidity affects the water adsorption capacity of zeolite 13X. At higher relative humidities, the amount of water adsorbed was higher. There was a good correlation between the experimental data and the curve generated by Bales et al [44] especially at higher humidities.

6.5 Sample Calculation

6.5.1 Introduction

This section provides a sample calculation to show how the experimental results from the thesis can be used to design a suitable TES system for the ceramic company described in Section 1.2. Factors such as regeneration temperature, temperature lift, humidity and flow rate were taken into consideration.

6.5.2 Calculation

The ceramic company described in Section 1.2 exhausts waste heat which is above 800 °C initially. Since zeolite 13X becomes hydrothermally unstable at temperatures above 200 °C [5, 34], this heat must be diluted with ambient air to achieve a maximum temperature of 200 °C. Based on the temperature data measured at the CSIR, the average temperature in Pretoria is approximately 20 °C. A maximum temperature of 60 °C is required to dry the Plaster of Paris moulds. This equates to a required temperature lift of 40 °C during discharging. It is assumed that the flow rate through the system will be 100 kg/h and the amount of energy (from the waste) to be stored is 1 MWh. A summary of these values is presented in Table 6-7 and the layout of the system is illustrated in Figure 6-7.

Table 6-7: Design parameters

Parameter	Value
Charging temperature	200 °C
Required discharging temperature	60 °C
Average ambient temperature	20 °C
Required temperature lift	40 °C
Mass flow rate	100 kg/h
Energy available for recovery	1 MWh



Figure 6-7: Block diagram of system

Based on the experimental results, for a temperature lift of 40 °C a specific humidity of 13 g_w/kg_{da} is required which is determined from Figure 6-3. For a regeneration temperature of 200 °C the charging efficiency was 67% (Table 6-1). Therefore, it is assumed that 670 kWh will be stored from the waste heat stream. The storage efficiency was 75% for discharging cycle 3 (Table 6-1) which had a similar humidity and regeneration temperature. This implies that approximately 500 kWh (50% overall efficiency) will be released from the storage during discharging. The energy storage density is calculated based on the amount of energy that is released from the storage. From Table 6-5 the energy density for discharging cycle 3 was 130.87 kWh/m³. For 500 kWh, a minimum volume of 3.8 m³ is required for storage. This equates to a mass of 2318 kg of zeolite 13X required for the packed bed reactor. To allow for charging and discharging to occur simultaneously, the system should consist of 2 smaller packed bed reactors with a minimum volume of 2 m³ each. However, by oversizing the reactors, the charging efficiency and hence overall efficiency is expected to be greater as discussed in Section 6.1. When the ambient humidity is too low to achieve the required temperature lift, the water evaporated from the casting moulds (in the drying chamber) should be fed back to the packed bed reactor to increase the humidity at the inlet of the packed bed. The calculated parameters are summarised in Table 6-8

Table 6-8: Calculated system parameters

Parameter	Value
Required humidity	12-13 g _w /kg _{da}
Overall efficiency	50%
Mass of zeolite required	~2320 kg
Volume of zeolite required	~4 m ³

6.5.3 Conclusion

This section provided an example of how the experimental results from the thesis can be applied to design a suitable TES system for waste heat recovery. The regeneration temperature, temperature lift, humidity, and flow rate were taken into consideration.

7 Conclusions and Recommendations

7.1 Experimental Testing

Thermochemical energy storage systems have high energy storage densities and can store heat for the long term. This ensures that thermal energy is available even when energy supply does not match demand. The integration of TCES systems with WHR technologies, in industry, can significantly increase the energy efficiency of manufacturing processes and hence reduce costs and carbon emissions. The aim of this research was to investigate the performance of a zeolite TES for waste heat recovery and thermal energy storage in the South African industrial sector. This was achieved by developing a lab-scale test rig at the CSIR (Pretoria). The zeolite 13X contained in the rig was subjected to different humidities, flow rates and regeneration temperatures. The performance of the system was analysed by comparing the experimental results to calculations and results available in literature. The potential of utilising zeolite 13X for drying was also demonstrated by connecting the packed bed to a subsystem containing ceramic casting moulds.

The results from three complete charging/desorption cycles were presented i.e., cycle 1 (200 °C), cycle 2 (160 °C) and cycle 3 (130 °C). By lowering the regeneration temperature, the amount of water dehydrated from the packed bed decreased. A maximum outlet humidity of 46 g_w/kg_{da}, 34 g_w/kg_{da} and 30 g_w/kg_{da} was achieved for cycles 1, 2 and 3 respectively. A lower regeneration temperature increases the regeneration time and decreases the amount of energy absorbed by the packed bed. 13.64 kWh was absorbed during the 200 °C, 11.99 kWh during the 160 °C charging cycle and 10.47 kWh during the 130 °C charging cycle. The time taken to charge the bed at 200 °C, 160 °C and 130 °C was 3.5 h, 4.5 h and 6 h respectively. The energy supplied to the packed bed 20.44 kWh, 22.45 kWh and 24.69 kWh for charging cycle 1, 2 and 3 respectively. The blower was run at full power and the mass flow rate ranged between 135 to 142 kg/h for the different charging tests. It was observed that regardless of the regeneration temperature, the thermocline reaches the outlet of the packed bed at $t = 1.5$ h after which the energy lost, from the outlet of the reactor to the atmosphere, increases steadily. During the first 1.5 h approximately 50% of the total energy, that can be stored for a particular regeneration temperature, is absorbed. Furthermore, between 2-3 h, the amount of energy absorbed from the supply drops to below 50%. From these results it can be concluded that the reactor should be oversized and the outlet temperature should not be allowed to rise too high to minimise losses to the atmosphere. The radial temperature profiles indicated that the temperature in the vicinity of the bed wall was a maximum of 30 °C lower than the axial temperature. This is due to heat losses through the walls of the test rig, as well as through the metal mesh at the base of the test rig.

Eight complete discharging tests were conducted at different humidities, flow rates and regeneration temperatures. From these tests it was deduced that the temperature lift across the reactor is a significant function of the specific humidity of the air entering the reactor. A temperature lift of 107 °C was

achieved for an inlet humidity of 34 g_w/kg_{da} compared to only 28 °C for an inlet humidity of 7 g_w/kg_{da}. The highest outlet temperature achieved during discharging was 138 °C for the high inlet humidity test (34 g_w/kg_{da}). A higher inlet humidity decreases the adsorption/ discharging time as more water is being adsorbed and more energy is being released per hour. The outlet humidity for the discharging cycles is approximately 0% during adsorption which indicates that zeolite adsorbs almost all the water from the inlet stream. The warm dry air exiting the reactor makes it suitable for drying applications in industry. The amount of energy released from the reactor during discharging ranged from 7.50 kWh (7 g_w/kg_{da} inlet humidity) to 11.56 kWh (34 g_w/kg_{da} inlet humidity). Thus, higher inlet humidities release more energy from the reactor during discharging. Lowering the flow rate resulted in a longer adsorption cycle time and also affected the amount of energy released from the reactor. A slight decrease in the temperature lift was also observed for lower flow rates. By decreasing the regeneration temperature, the energy released from the packed bed was also decreased implying that regeneration temperature affects the storage capacity of the system.

For discharging cycles (1-7) the adsorption test was carried out a few days after regeneration. For the final test that was presented (cycle 8), the reactor was discharged after a period of 5 months after regeneration due to Covid lockdown restrictions and the reactor was not sealed off, allowing the outer layers to adsorb water from the atmosphere. However, a temperature lift of 53 °C was achieved across the reactor. The maximum outlet temperature of the reactor was 80 °C and 9.83 kWh was released which is still significantly high. This test demonstrates the potential of zeolite 13X to store energy for the long term with minimal losses.

During the discharging cycles, the temperature profiles at the wall and radial positions clearly indicate the influence of the reactor wall since the temperature in the wall region ($r = 0.195$ m) was lower than the centre of the reactor ($r = 0$ m). The temperature also drops significantly faster than the axial temperature due to the adsorption process occurring much faster near the wall region because of the increased porosity and hence fluid velocity near the wall. Furthermore, channelling through the packed bed may have contributed to the adsorption process occurring faster at a radial position of 0.1 m.

From the additional charging cycle (after partially discharging the bed prior) presented, it can be seen that temperatures close to the regeneration temperatures are attainable during adsorption at very high specific humidities. It is also preferable to charge the bed from the top and discharge it from the bottom so in the event that the bed is partially discharged, the top layers will already be dry and hence the energy to regenerate the packed bed will be lower. In this instance the bottom layers were dry and were saturated by the water desorbed from the upper layers during charging. Energy had to be put in to dehydrate these layers although they were dry initially. The additional discharging test presented (including sensible heat) was initiated directly after the charging cycle. This test shows that initially the energy released will be

sensible heat until the reactor cools down to the adsorption temperature (depending on specific humidity) and the cycle will continue thereafter like a typical discharging cycle.

By attaching a simple subsystem (consisting of a kiln, bypass valve, PLC and motor to control the valve) to the zeolite reactor, drying tests were run on ceramic casting moulds. It was shown that the control system with the butterfly bypass valve can maintain the temperature in the kiln at 60 °C regardless of the reactor outlet temperature varying due to fluctuations in humidity. The average drying rate of the ceramic casting moulds was 0.245 kg/h for the first test and 0.66 kg/h for the second test. The drying rate can be improved by improving the airflow around the moulds as was shown with the addition of the axial fan to the kiln. This can be further improved by introducing a support mesh which minimizes obstruction to the airflow, completely filling the drying chamber with casting moulds and strategically stacking the moulds to reduce gaps and hence prevent the air from choosing the path with the least resistance.

To determine the amount of water that can be adsorbed, tests were performed on 1 kg samples of zeolite 13X at different relative humidity while keeping the temperature constant at 55 °C. The amount of water that can be adsorbed ranged from 216 g_w/kg_{zeolite} (21.6%) at 10% relative humidity to a maximum of 286 g_w/kg_{zeolite} (28.6%) at 85% relative humidity. The experimental results were compared to calculations done using the Langmuir-Freundlich model. The experimental results were close to the calculated values at higher RH values, however, there was a deviation at lower RH values. This was due to the controller struggling to maintain lower humidities in the chamber from which air was being sucked. However, this test still indicates that the relative humidity of the air, entering the reactor, profoundly affects the amount of water vapour that can be adsorbed by zeolite 13X.

7.2 Performance Analysis

Based on the experimental results from the charging and discharging cycles, the energy efficiencies of the system were calculated. The highest charging efficiency was 67% for the 200 °C regeneration cycle. The maximum storage efficiency was 90% for the discharging cycle (6) performed after the 160 °C regeneration cycle and the maximum overall efficiency was 57% for discharging cycle 1 (highest inlet humidity during adsorption). It was shown that by immediately discharging the bed after charging (i.e., capturing all the sensible heat), the overall efficiency can be improved from 57% to 70%. It was noticed that the humidity and flow rate mainly affected the storage efficiency while the regeneration temperature mainly affected the charging efficiency and hence the overall efficiency.

The Langmuir-Freundlich model was used to calculate the water content of zeolite before and after adsorption which affects the temperature lift and energy density. The experimental temperature lift was then compared to the calculated temperature lift. At lower humidities/ temperatures the experimental values agree with the theoretical values. At higher temperatures, there are greater heat

losses to the surrounding atmosphere. Furthermore, condensation on the humidity sensors may have led to inaccurate readings resulting in a deviation between the experimental and theoretical values.

The experimental values were compared to the calculated values for the energy storage density with good agreement between the two. The maximum experimental energy storage density was 148 kWh/m³. The experimental values were also compared to the values presented by ZAE Bayern. The values were close, within 16% for the outlier (130 °C) and within 5% for the other two regeneration temperatures (160 °C and 200 °C). The results indicate that regeneration temperature as well as the relative humidity during discharging affects the storage capacity. From their results it was determined that a maximum of 255 kWh can be stored per ton of zeolite 13X after regeneration at 200 °C.

7.3 Recommendations for Future Work

Further testing is required to commercialise thermochemical energy storage systems using zeolite 13X as the storage medium. The next step would be to develop a pilot-scale storage system for implementation in industry and to determine the impact on energy efficiency and costs. The ceramic manufacturing company, described in Section 1.2, provides the ideal TES opportunity as vast amounts of waste heat is available for regeneration/ desorption. The stored heat will be used for drying the ceramic casting moulds. The warm air, coupled with low humidity, leaving the zeolite reactor should yield higher drying rates compared to the conventional electric kilns. This should increase productivity while reducing manufacturing costs. A sample calculation is presented in Section 5.5 to highlight the method that will be followed to size a suitable reactor for the TCES system.

Another concept to be explored is the possibility of recovering water, from the high humidity air stream, exiting the reactor during regeneration/ desorption. zeolite 13X can store up to 300g_w/kg_{zeolite} which can be recovered, especially at higher regeneration temperatures due to the higher humidity and hence dew point. At a regeneration temperature of 200 °C, the exit air stream is at a humidity of 46 g_w/kg_{da} for a large part of the cycle and the dew point temperature is approximately 36 °C at this altitude. The recovery of water will thus reduce water consumption in industrial manufacturing processes in addition to electricity consumption.

References

- [1] Department of Mineral Resources and Energy, “Energy Statistics: Energy Balances,” 2018. [Online]. Available: http://www.energy.gov.za/files/energyStats_frame.html. [Accessed 20 October 2021].
- [2] DEPARTMENT OF ENERGY, “INTEGRATED ENERGY PLAN,” DEPARTMENT OF ENERGY, Pretoria, 2016.
- [3] I. Johnson, W. T. Choate and A. Davidson, “Waste Heat Recovery:- Technology and Opportunities in U.S. Industry,” U.S. Department of Energy, United States, 2008.
- [4] P. Klein, “Analysis of a thermal energy storage system to provide waste heat recovery for batch-wise processes,” CSIR, Pretoria, 2018.
- [5] B. Mette, H. Kerskes, H. Druck and H. Muller-Steinhagen, “Experimental and Numerical Investigations on the water vapour adsorption isotherms and kinetics of binderless zeolite 13X,” *International Journal of Heat and Mass Transfer*, pp. 555-561, 2014.
- [6] S. Vasta, V. Brancato, D. La Rosa, . V. Palomba, G. Restuccia, A. Sapienza and A. Frazzica, “Adsorption Heat Storage: State-of-the-Art and Future Perspectives,” *Nanomaterials*, vol. 8, p. 522, 2018.
- [7] A. Hauer, “Thermal Energy Storage with Zeolite for Heating and Cooling Applications,” in *International Sorption Heat Pump Conference*, Munich, 2002.
- [8] D. M. Parikh, “SOLIDS DRYING: BASICS AND APPLICATIONS,” 1 April 2014. [Online]. Available: <https://www.chemengonline.com/solids-drying-basics-and-applications/?printmode=1>. [Accessed 7 August 2021].
- [9] J. Basinger, “Chemical Processing 101: Drying,” Howard Industries, [Online]. Available: <https://howardchem.com/chemical-processing-101-drying/>. [Accessed 9 August 2021].
- [10] GlobalSpec, “Process Dryers Information,” Engineering 360, [Online]. Available: https://www.globalspec.com/learnmore/processing_equipment/materials_processing_equipment/process_dryers. [Accessed 9 August 2021].
- [11] R. H. Byrne, F. T. Mackenzie and A. C. Duxbury, “Seawater,” *Encyclopedia Britannica*, 5 November 2020. [Online]. Available: <https://www.britannica.com/science/seawater/Thermal-properties#ref540410>. [Accessed 8 August 2021].
- [12] B&C Technologies, “Industrial and Commercial Dryers,” B&C Technologies, [Online]. Available: <https://bandctech.com/industrial-commercial-dryer.php>. [Accessed 8 August 2021].
- [13] T. O. Mason, “Traditional ceramics,” *Encyclopedia Britannica*, 3 November 2016. [Online]. Available: <https://www.britannica.com/technology/traditional-ceramics>. [Accessed 6 August 2021].
- [14] Japan Metals & Chemicals Co., Ltd., “Ceramics Group: Manufacturing Process,” [Online]. Available: <http://www.jmc.co.jp/en/products/ceramics.html>. [Accessed 5 August 2021].

- [15] P. Tatsidjoudoung, N. Le Pierres, J. Heintz, D. Lagre, L. Luo and F. Durier, “Experimental and Numerical investigations of a zeolite 13X/water reactor for solar heat storage in buildings,” *Energy Conversion and Management*, vol. 108, pp. 488-499, 2015.
- [16] D. Lefebvre, “Thermal Energy Storage Using Adsorption Processes for Solar and Waste Heat Applications: Material Synthesis, Testing and Modeling,” University of Ottawa , Canada, 2016.
- [17] I. Sarbu and C. Sebarchievici, “A Comprehensive Review of Thermal Energy Storage,” *Sustainability*, vol. 10, p. 191, 2018.
- [18] . R. Balijepalli, V. P. Chandramohan and K. Kirankumar, “ Performance parameter evaluation, materials selection, solar radiation with energy losses, energy storage and turbine design procedure for a pilot scale solar updraft tower,” *Energy Conversion and Management*, vol. 150, pp. 451-462, 2017.
- [19] . A. A. Adeyanju, “THERMAL ENERGY STORAGE TECHNIQUES,” *Sci-Afric Journal of Scientific Issues, Research and Essays*, vol. 3(5), no. 2311-6188, pp. 726-736, 2015.
- [20] K. S. Reddy, V. Mudgal and T. K. Mallick, “Review of latent heat thermal energy storage for improved material,” *Journal of Energy Storage*, vol. 15, pp. 205-227, 2018.
- [21] S. S. Chandel and T. Agarwal, “Review of current state of research on energy storage, toxicity, health, hazards and commercialization of phase changing materials,” *Renewable and Sustainable Energy Reviews*, vol. 67, pp. 581-596, 2016.
- [22] N. Yu, R. Z. Wang and L. W. Wang, “Sorption Thermal Storage for Solar Energy,” *Progress in Energy and Combustion Science*, vol. 39, pp. 489-514, 2013.
- [23] B. Mette, H. Kerskes, H. Drück and H. Müller-Steinhagen, “New highly efficient regeneration process for thermochemical energy storage,” *Applied Energy*, vol. 109, pp. 352-359, 2013.
- [24] A. H. Abedin and M. A. Rosen, “Closed and open thermochemical energy storage: Energy- and exergy-based comparisons,” *Energy*, vol. 41, pp. 83-92, 2012.
- [25] B. Ugur, “Thermal Energy Storage in Adsorbent Beds,” University of Ottawa, Ottawa, Canada, 2013.
- [26] F. NEGIS, “Zeolite based composites in Energy Storage,” Izmir Institute of Technology, Izmir, Turkey, 1999.
- [27] A. Dąbrowski, “Adsorption — from theory to practice,” *Advances in Colloid and Interface Science*, vol. 93, no. 1-3, pp. 135-224, 2001.
- [28] D. Aydin, S. P. Casey and S. Riffat, “The latest advancements on thermochemical heat storage systems,” *Renewable and Sustainable Energy Reviews*, vol. 41, pp. 356-367, 2015.
- [29] N. Makhanya, B. Oboirien, J. Ren, N. Musyoka and A. Sciacovelli, “Recent advances on thermal energy storage using metal-organic frameworks (MOFs),” *Journal of Energy Storage*, vol. 34, 2021.
- [30] F. Kuznik, . K. Johannes, C. Obrecht and D. David, “A review on recent developments in physisorption thermal energy storage for building applications,” *Renewable and Sustainable Energy Reviews*, vol. 94, pp. 576-586, 2018.

- [31] L. Scapino, H. A. Zondag, J. Van Bael, J. Diriken and C. C. Rindt, "Sorption heat storage for long-term low-temperature applications: A review on the advancements at material and prototype scale," *Applied Energy*, vol. 190, pp. 920-948, 2017.
- [32] "Zeolite," [Online]. Available: <https://www.kalliergeia.com/en/glossary/zeolite/>. [Accessed 10 April 2020].
- [33] A. J. Schwanke, R. Balzer and S. Pergher, "Microporous and Mesoporous Materials from Natural and Inexpensive Sources," in *Handbook of Ecomaterials*, Springer International Publishing, 2017, pp. 1-22.
- [34] J. Jänchen, K. Schumann, E. Thrun, A. Brandt, B. Unger and U. Hellwig, "Preparation, hydrothermal stability and thermal adsorption storage properties of binderless zeolite beads," *International Journal of Low-Carbon Technologies*, vol. 7, no. 4, p. 275–279, 2012.
- [35] Zan-Technologies cc, "Zeozorb 13X APG Molecular Sieve," [Online]. Available: <https://www.zantech.co.za/wp-content/uploads/2014/09/ZAN055-ZEOSORB-13X-APG-SPEC-SHEET.pdf>. [Accessed 5 April 2020].
- [36] H. Kerskes, "Chapter 17 - Thermochemical Energy Storage," in *Storing Energy*, Elsevier, 2016, pp. 345-372.
- [37] X. Zhang and I. Dincer, "Progress in Sorption Thermal Storage," in *Energy Solutions to Combat Global Warming*, Springer International Publishing, 2017, p. 555.
- [38] M. Djaeni, C. van Asselt, P. Bartels, J. Sanders, G. van Straten and A. J. Van Boxtel, "Low Temperature Drying with Air Dehumidified by Zeolite for Food Products: Energy Efficiency Aspect Analysis," *International Journal of Food Engineering*, vol. 7, no. 6, 2011.
- [39] A. Krönauer, E. Lävemann, S. Brückner and A. Hauer, "Mobile Sorption Heat Storage in Industrial Waste Heat Recovery," *Energy Procedia*, vol. 73, pp. 272-280, 2015.
- [40] M. Gaeni, H. A. Zondag and C. Rindt, "Non-Isothermal kinetics of zeolite water vapour adsorption into a packed bed lab scale thermochemical reactor.," in *international Heat Transfer Conference*, Kyoto, 2014.
- [41] M. Gaeni, H. A. Zondag and C. Rindt, "Effects of Kinetics on the thermal performance of a sorption heat storage reactor," *Applied Thermal Engineering*, vol. 102, pp. 520-531, 2016.
- [42] Y. A. Cengel and M. A. Boles, *Thermodynamics: An Engineering Approach*, McGraw-Hill, 2006.
- [43] K. A. R. Ismail and R. Stuginsky Jr., "A parametric study on possible fixed bed models for pcm and sensible heat storage," *Applied Thermal Engineering*, vol. 19, pp. 757-788, 1999.
- [44] C. Bales, P. Gantenbein, A. Hauer, H.-M. Henning and D. Jaenig, "Thermal Properties of Materials for Thermo-chemical Storage of Solar Heat," International Energy Agency (IEA), Paris, 2005.
- [45] "What's Wrong with Relative Humidity Above 100°C? - Machine Applications Corporation," Machine Applications Corporation, [Online]. Available: <https://www.macinstruments.com/blog/whats-wrong-with-relative-humidity-above-100-celsius/>. [Accessed 6 July 2021].

- [46] E. Lilly, "9 Things Your Home's Low Humidity Is Ruining," [Online]. Available: <https://www.thisoldhouse.com/heating-cooling/21018593/9-things-your-home-s-low-humidity-is-ruining>. [Accessed 7 August 2021].
- [47] A. Hauer, "Evaluation of adsorbent materials for heat pump and thermal energy storage applications in open systems," *Adsorption*, vol. 13, p. 399–405, 2007.
- [48] A. Hauer and F. Fischer, "Open Adsorption System for an Energy Efficient Dishwasher," *Chemie Ingenieur Technik*, vol. 83, no. 1-2, pp. 61-66, 2011.
- [49] G. Storch and A. Hauer, "COST-EFFECTIVENESS OF A HEAT ENERGY DISTRIBUTION SYSTEM BASED ON MOBILE STORAGE UNITS: TWO CASE STUDIES," 2006. [Online]. Available: <https://pdfs.semanticscholar.org/09f0/f0a413957bd5ce421d38bc4d67da8a7587.pdf>. [Accessed 25 September 2021].
- [50] P. Klein, "High Temperature Packed Bed Thermal Storage For Solar Gas Turbines," University of the Witwatersrand, Johannesburg, 2016.
- [51] K. Ratshomo and R. Nembahe, "2018 SOUTH AFRICAN ENERGY SECTOR REPORT," Department of Energy, Pretoria, 2018.
- [52] E. I. Alnaimi, "The Effect of Key Parameters Such as Temperature and Contact Time on The Hydroisomerization of n-heptane Over Platinum Loaded Zeolite USY Catalysts," University of Manchester, Manchester, 2012.
- [53] M. Gacini, H. A. Zondag and C. Rindt, "Effect of kinetics on the thermal performance of a sorption heat storage reactor," *Applied Thermal Engineering*, vol. 102, pp. 520-531, 2016.

Appendix A: Experimental Apparatus

Equipment and Instrumentation Utilised

Humidifier

A Shell and Tube heat exchanger was designed to transfer heat between air and water. The air which is heated by the 8.5 kW electric heater is used to boil water in the tube of the heat exchanger and hence create steam for humidification. As shown in Figure A-1, spiral deflectors were strategically welded onto the tube of the heat exchanger to force the air to swirl in two separate planes to increase the efficiency by increasing the path length of the heating flow. A storage tank was connected to the heat exchanger to supply water for humidification. The storage tank indicates the exact height of the water in the tube of the heat exchanger so as not to overflow the humidifier and cause water to flood into the airstream entering the reactor. A ball valve was used to control the flow of water into the tube of the heat exchanger. A K-Type thermocouple was inserted into the tube to monitor the water temperature and determine when the boiling point of the water (100 °C at sea level and 95 °C in Pretoria) is reached. The heater has a potentiometer to control the temperature of the air and hence control the humidity of the air entering the bed. The flanges allow for the heater to be bolted to the humidifier.

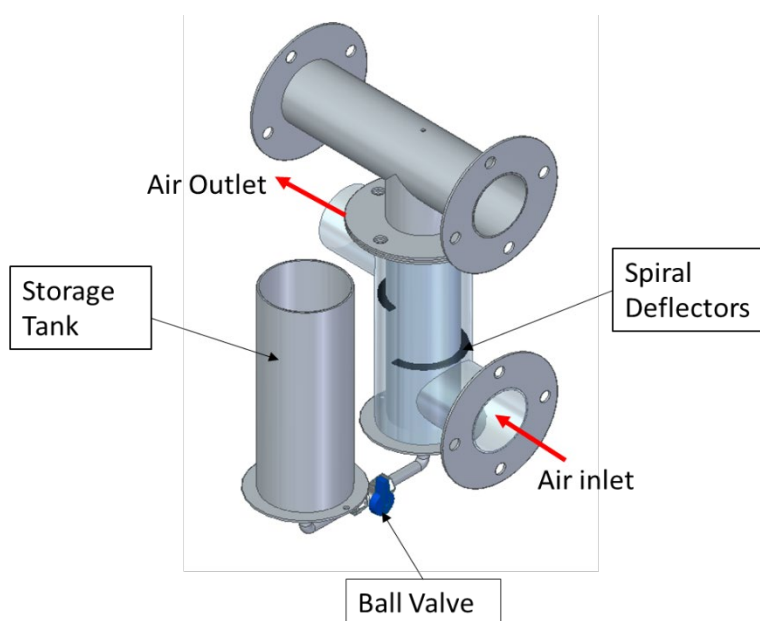


Figure A-1: Humidifier

Electric Heater

A Leister LHS 61S Premium heater (Figure A-2) was purchased to dehydrate the zeolite beads during the charging cycle and to provide steam for humidification during the discharging cycle. The heater is

3-phase and provides a maximum of 8.5 kW of power. It has a potentiometer to manually control the temperature output. It can produce a maximum temperature of 650°C.



Figure A-2: Leister LHS 61S Premium Heater

Primary Blower

A 2.2 kW Side channel oil free blower was used to supply air to the packed bed during charging and discharging. The blower is manufactured by Mapro International (Model: RB50-620) and it is 3-phase and has a frequency of 50 Hz. A conical inlet was bolted to the inlet to measure the airflow through the system as shown in Figure A-3.



Figure A-3: Centrifugal Blower with Conical Inlet Attached

Secondary Blower

A 40W ‘ebm-papst’ centrifugal blower (Figure A-4) was used to supply air to the heater to boil water for humidification during the discharge cycle. The blower is rated at 155m³/h at STP.



Figure A-4: ebm-papst centrifugal blower

Data Logger

The Keysight 34970A Data logger was used to measure and store the data from the experiments that were conducted. It can accommodate three multiplexer cards. The 34901A multiplexer, which consists of 20 channels, was used. Figure A-5 shows the thermocouples wired to the multiplexer.

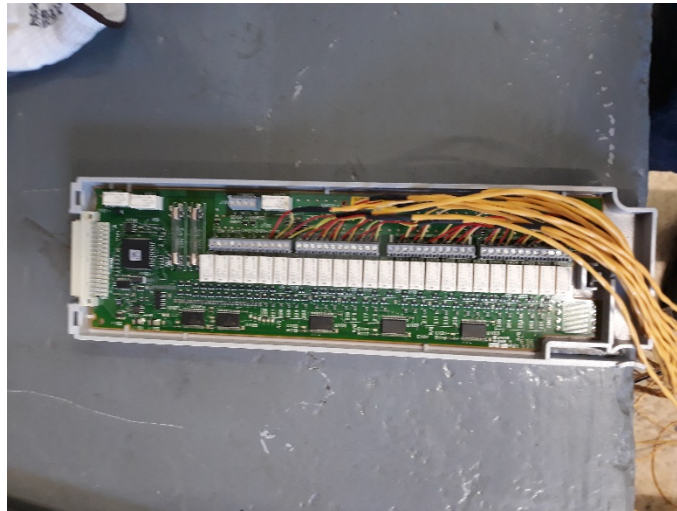


Figure A-5: Thermocouples wired to Multiplexer

Conical Inlet for Air Flow Rate Measurement

The conical inlet was designed according to the BS 848 standard [50]. The internal diameter chosen was 30 mm. This ensures that the Reynolds number is greater than 20 000 which is a requirement according to the standard. The geometry for the conical inlet is shown Figure A-6.

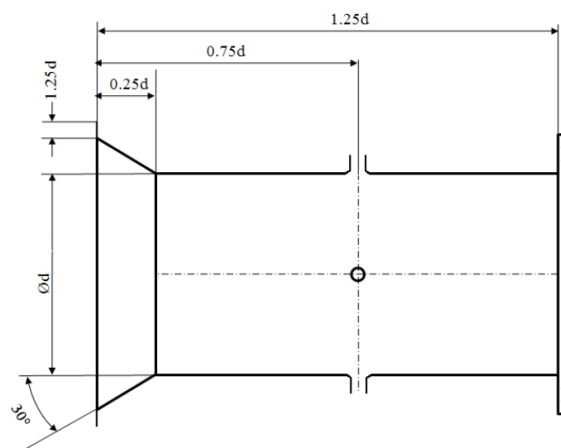


Figure A-6: Conical inlet geometry [50]

The conical inlet was machined from aluminium as seen in Figure A-7. It consists of four pressure tappings to measure the pressure in the throat of the conical inlet. 5mm Festo push-in fittings were inserted into the conical inlet for easy attachment of hoses from the pressure sensor. To minimise the

complexity of the instrument, the conical inlet, diffuser and flange were machined as one part. The diffuser is necessary to step up the diameter from that of the conical inlet to the suction side of the blower while the flange allows easy attachment to the blower with minimal leaks.



Figure A-7: Conical inlet

The following equations are used to calculate the mass flow rate through the system. The pressure differential used in the equation (ΔP_c) is the difference between the pressure in the throat ($d_c = 30mm$) of the conical inlet and atmospheric pressure

$$\dot{m}_f = C_d \pi \frac{d_c^2}{4} \sqrt{2\rho_f \Delta P_c} \quad (A-1)$$

$$C_d = 0.01 \log_{10} Re_c + 0.887 \quad (A-2)$$

Humidity Sensors

The HTM2500LF Humidity sensor, manufactured by Measurement Specialities, was one of two sensors utilises during testing. The other being the Testo ‘Robust humidity/temperature probe (digital),’ which was acquired at a much higher cost than the HTM2500LF . The HTM2500LF sensor comprises a 10000 Ohms thermistor for temperature measurement. The supplier claims that the sensor has an accuracy of ± 3 %RH between 10 to 95% RH. At higher humidities, condensation on the sensors led to inaccurate readings above 100% RH. However, the sensor proved to be quite accurate at lower humidities with values comparable to the Testo sensor. The operating range is -40 to 85 °C and 0 to 99% relative humidity. It requires a 5 volts supply voltage and produces a 1–4-volt DC output. The sensor is shown Figure A-8.



Figure A-8: HTM2500LF Humidity Sensor

The humidity sensor consists of four wires and a shield. A summary of the respective wires and their purpose is presented in Table A-1

Table A-1: Humidity sensor wires

Wire Colour	Function
Brown	Ground
White	Supply Voltage
Yellow	Humidity Voltage Output
Green	Temperature Output

Since the HTM2500LF sensor is more accurate at lower humidities (compared to higher humidities) it was used to monitor the lower humidities at the inlet of the packed bed during charging/desorption (before the air was heated) and the outlet of the packed bed during discharging/adsorption. The Testo sensor was used to measure the higher humidities at the inlet of the packed bed during discharging and the outlet of the packed bed during charging.

The Testo sensor has a higher temperature limit of 180 °C (making it suitable for monitoring the bed outlet humidity during charging) and a higher RH accuracy of ± 2 % RH between 2.1 to 98 % RH and ± 3 % RH between 0 to 2 % RH and 98 to 100 % RH. The sensor is portable and connects to the Testo 440 IAQ measuring instrument for displaying readings and logging data (refer to Figure A-9). The Testo sensor was calibrated by ‘Montech Calibration Services’ (accredited by the South African National Accreditation System) with a maximum deviation of 2.2% RH realised during calibration.



Figure A-9: Testo humidity sensor and measurement device

Pressure Transducers

Differential pressure sensors with a maximum pressure rating of 7 kPa were purchased. The sensors were used to determine the mass flow rate, through the system, based on the pressure differential across the conical inlet. The sensors were wired to the Keysight data logger mentioned above. A 5 kPa Betz Manometer was used to calibrate the pressure sensors (as shown in Figure A-10).



Figure A-10: Pressure transducers connected to Betz manometer

Assembly of Rig

A fine mesh (2mm) was placed over the grating to prevent the zeolite beads from falling through as shown in Figure A-11. The mesh was cut approximately 10mm larger than the diameter of the reactor to allow the flanges to clamp it and prevent movement. Gaskets were cut from 3mm ceramic fibre paper and placed between the flange and grating to contain the air pressure. The bottom cone and

reactor were bolted to the grating using 12 M12 bolts (refer to Figure A-12). Copper slip/ grease was applied to the thread of the bolts to prevent seizing when the system is subjected to high temperature.

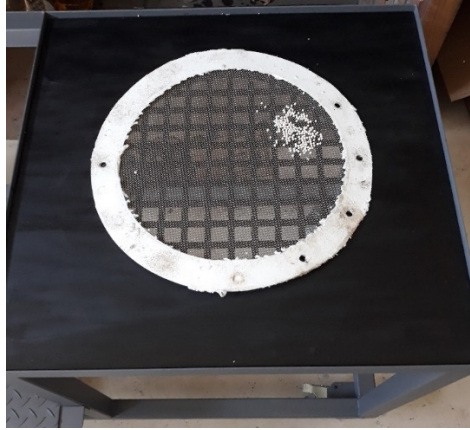


Figure A-11: Fine mesh and gasket placed on grating



Figure A-12: Reactor and Bottom Cone bolted together

Thermocouples were inserted into the lowest ports of the reactor. A Vernier Calliper was used to position the thermocouples at the desired radial distance. Silicone was used to seal the spaces around the thermocouple to minimise pressure losses in the system. Zeolite beads were then filled into the reactor (Figure A-13) until the next axial increment with thermocouple ports was reached. Thermocouples were inserted and the process was then repeated until the reactor was completely packed. It should be noted that the loaded particles were not vibrated nor tamped with but rather poured into the reactor (with a 1.5 litre vessel) until the reactor was full.



Figure A-13: zeolite packed in reactor bed

The top cone was bolted onto the reactor with a ceramic gasket between the flanges. The reactor was then insulated using ceramic fibre blanket (Figure A-14) of 75mm thickness.



Figure A-14: Insulated Reactor

A 90-degree bend was bolted to the top of the reactor followed by a 300 mm straight section of pipe. The humidifier was then bolted onto this pipe section and the heater was bolted onto the frame. A picture of the full assembly for the charging and discharging configuration is shown in Figure A-15 and Figure A-16.



Figure A-15: Full Assembly showing charging configuration



Figure A-16: Full Assembly showing discharging configuration

Appendix B: Detailed Experimental Results

Charging Cycle 2: 160 °C

The temperature profiles for the second charging test are presented in Figure B-1. The inlet temperature was raised to 160 °C for the duration of the test. The time taken to complete the cycle was 4.5 hours. By lowering the temperature from 200 °C to 160 °C the cycle time increased by almost 1 hour. Similar behaviour was exhibited by the packed bed, as charging cycle 1, in terms of the shape of the profiles and the thermocline moving through the bed.

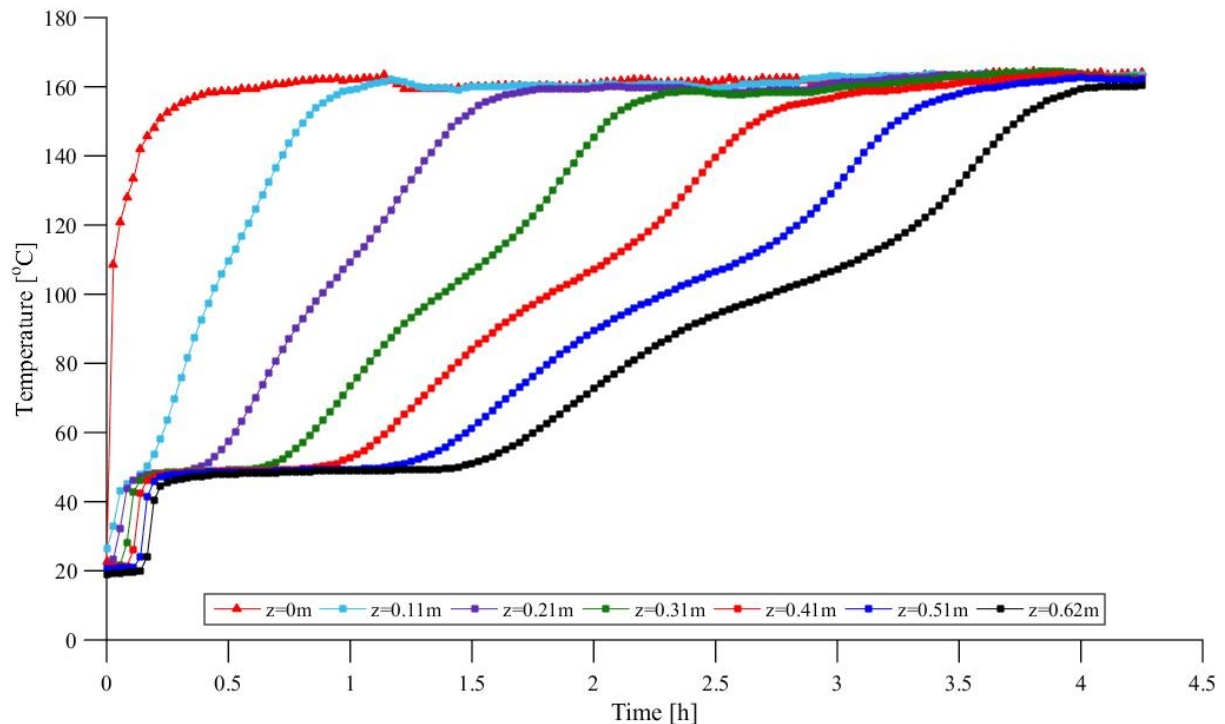


Figure B-1: Axial temperature profiles at various bed depths (z) - Charging cycle 2

The humidity and mass flow rate results for charging cycle 2 are presented in Figure B-2. The inlet humidity ranged between 5-10 g_w/kg_{da} for the cycle. The maximum outlet humidity was 34 g_w/kg_{da}. The outlet humidity decreased from t = 1.3 h to t = 4 h. A slight increase was noted in the outlet humidity at t = 4 h. The outlet humidity should continue to decrease as the bed dries. However, due to the reduced RH scale at temperatures above 100 °C, the outlet humidity does not continue to decrease and agree with the inlet (ambient) humidity at the end of the test. According to [45], an instrument with a 2% RH accuracy will indicate a ±20% accuracy of the specific humidity at a temperature of 175 °C. The average mass flow rate was 139 kg/h for the cycle and varied by 2% during the test. The mass flow rate decreases as the bed heats up due to a change in air density.

The radial temperature profiles at various bed depths are presented in Figure B-3. Similar behaviour was observed as the first charging test.

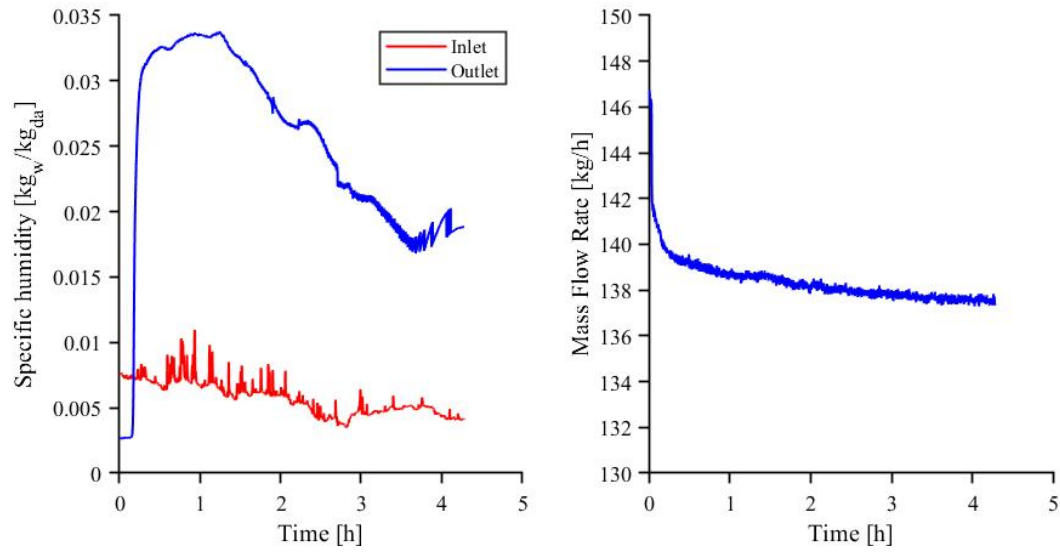


Figure B-2: Humidity and Mass flow rate - Charging cycle 2

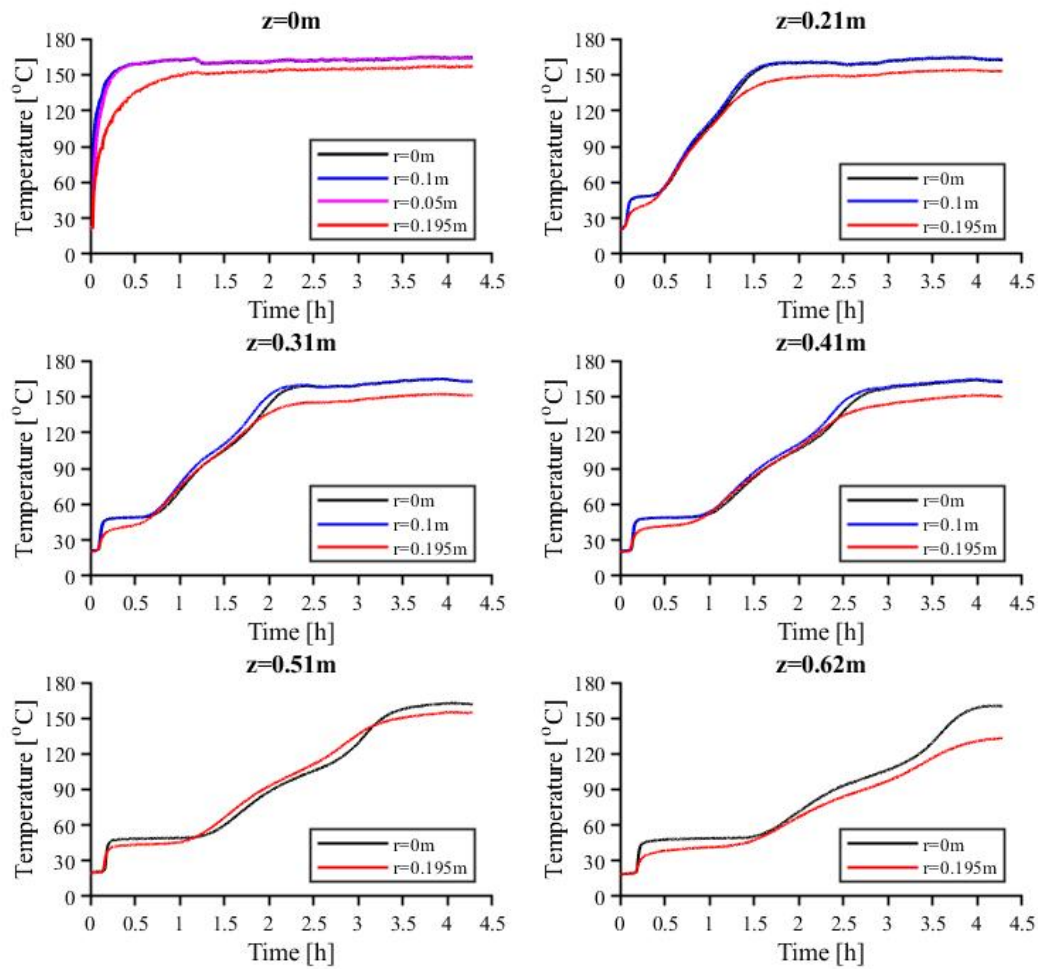


Figure B-3: Radial temperature profiles at various bed depths (z) - Charging cycle 2

Charging Cycle 3: 130 °C

The temperature profiles and humidity for the third charging test is presented in Figure B-4. The inlet temperature was raised to 130 °C for the duration of the test. The time taken to complete the cycle was 6 hours. Lowering the charging temperature almost doubles the cycle time (compared to 200 °C) as less energy is being supplied to the bed. The temperature increase, once the desorption front reached a particular layer, was also very gradual compared to the steep increases seen in the previous cycles. This can be attributed to the much slower rate of desorption.

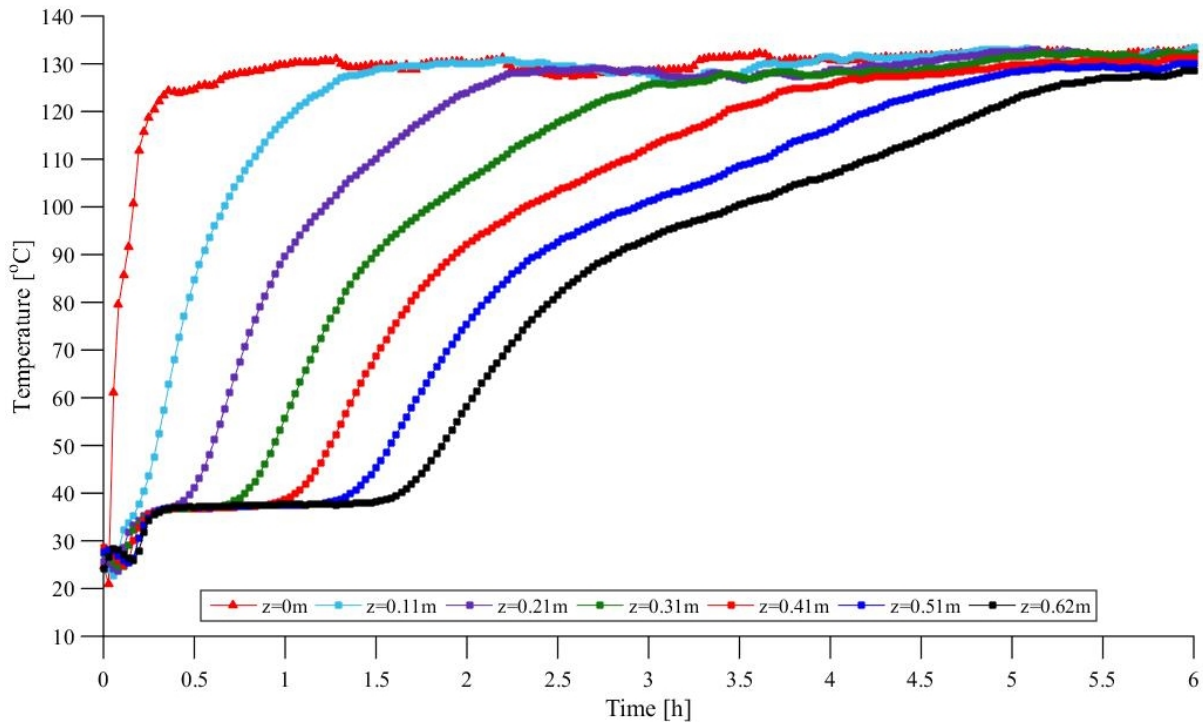


Figure B-4: Axial temperature profiles at various bed depths (z) - Charging cycle 3

The humidity and mass flow rate results for charging cycle 3 are presented in Figure B-5. The inlet (ambient) humidity range was between 5-10 $\text{g}_w/\text{kg}_{\text{da}}$ for the entire cycle. The maximum outlet humidity was 30 $\text{g}_w/\text{kg}_{\text{da}}$. The outlet humidity decreased as the bed dried. The outlet humidity should agree with the inlet (ambient) humidity at the end of the test as no more water is being desorbed. However, the humidity sensors are not accurate at temperatures above 100 °C due to the reduced scale of relative humidity in this temperature range. According to [45], an instrument with a 2% RH accuracy will indicate a $\pm 10\%$ accuracy of the actual/ specific humidity, of the air, at a temperature of 150 °C. The average mass flow rate was 142 kg/h for the cycle and varied by 2% during the test. As mentioned previously, the mass flow rate decreases as the bed heats up since the air density drops at higher temperatures.

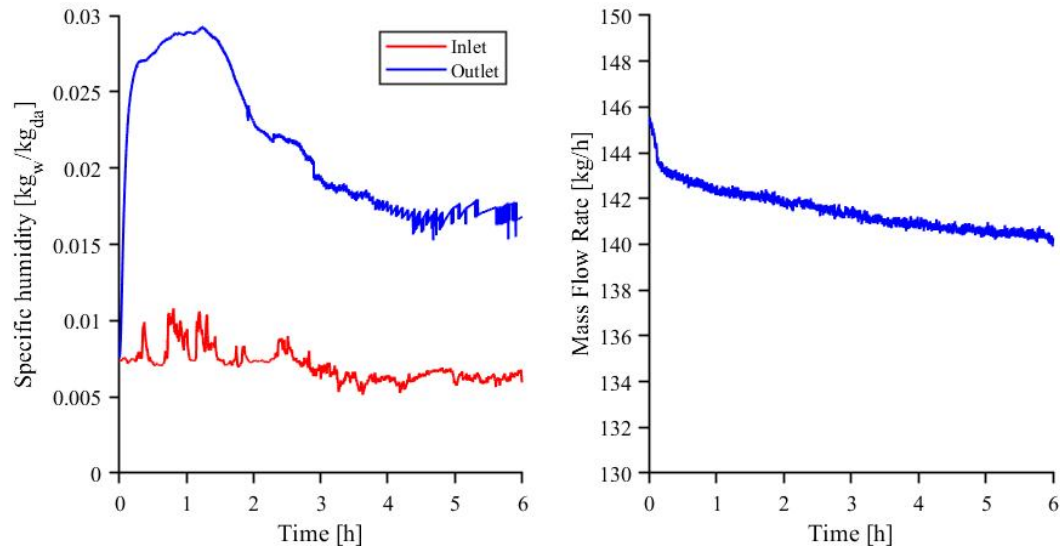


Figure B-5: Humidity and Mass flow rate - Charging cycle 3

The radial temperature profiles at various bed depths are presented in Figure B-6. The wall temperature is lower than the axial temperature as seen in previous tests. However, the temperature difference between the wall and the centre of the bed is slightly lower since the heat losses are less at lower temperatures. The channelling effects seen in the previous cycles are not noticeable since the temperatures at a radial position of 0.1 m are almost the same as the axial temperatures.

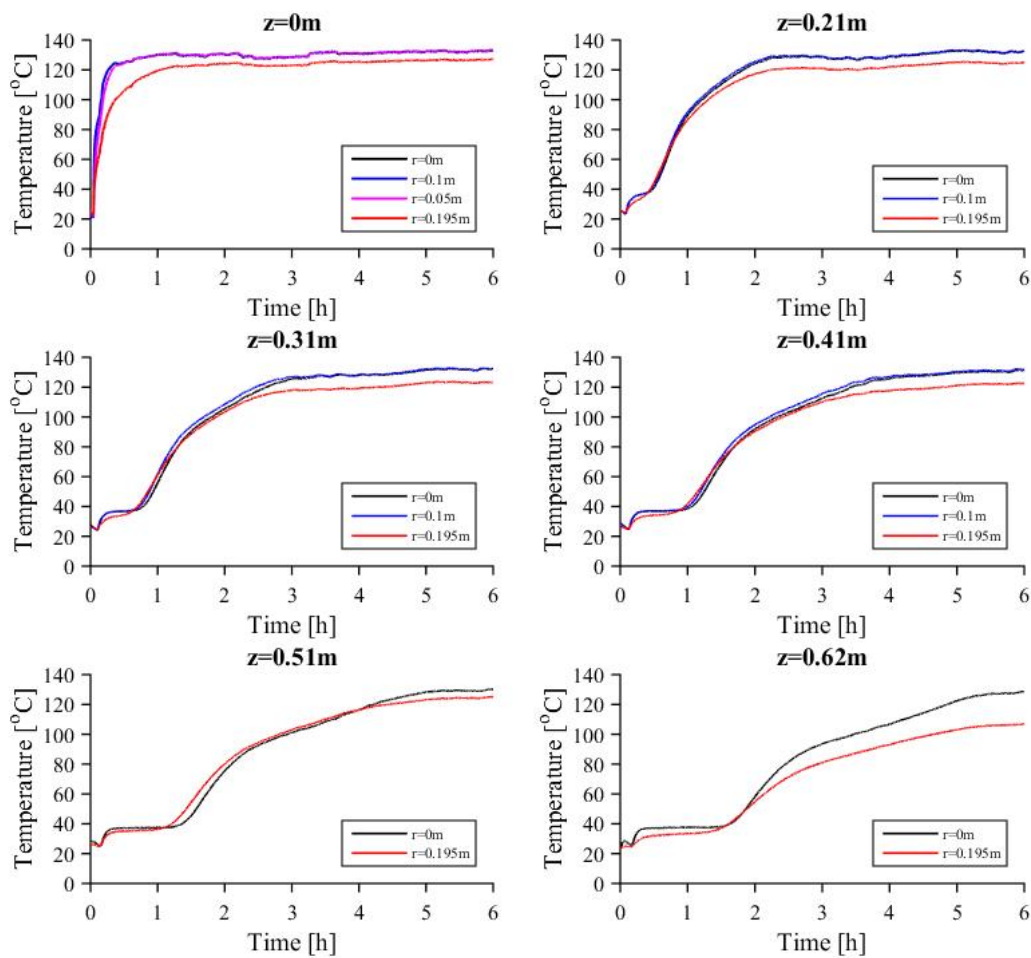


Figure B-6: Radial temperature profiles at various bed depths (z) - Charging cycle 3

Discharging Cycle 2: ~70% RH

The temperature profiles at the centre of the bed are presented in Figure B-7. The maximum temperature achieved was 108 °C i.e., a temperature lift of 75 °C was achieved. The outlet of the bed took approximately 30 min to heat up as seen in the previous test. Fluctuations in temperature are caused by variations in the humidity at the inlet since the humidity was controlled manually i.e., by filling water into the humidifier at intervals. This decreases the temperature and increases the pressure of the water already in the humidifier resulting in a slight decrease in humidity. The initial high temperature of approximately 47 °C (at $z = 0$ m) is due to steam flowing through the pipe from the humidifier which was turned on before blowing air through the packed bed. The cycle took approximately 4.25 h to complete which was longer than discharge cycle 1 (which lasted 3 h). This is due to the lower humidity supplied to the reactor and hence a lower adsorption rate.

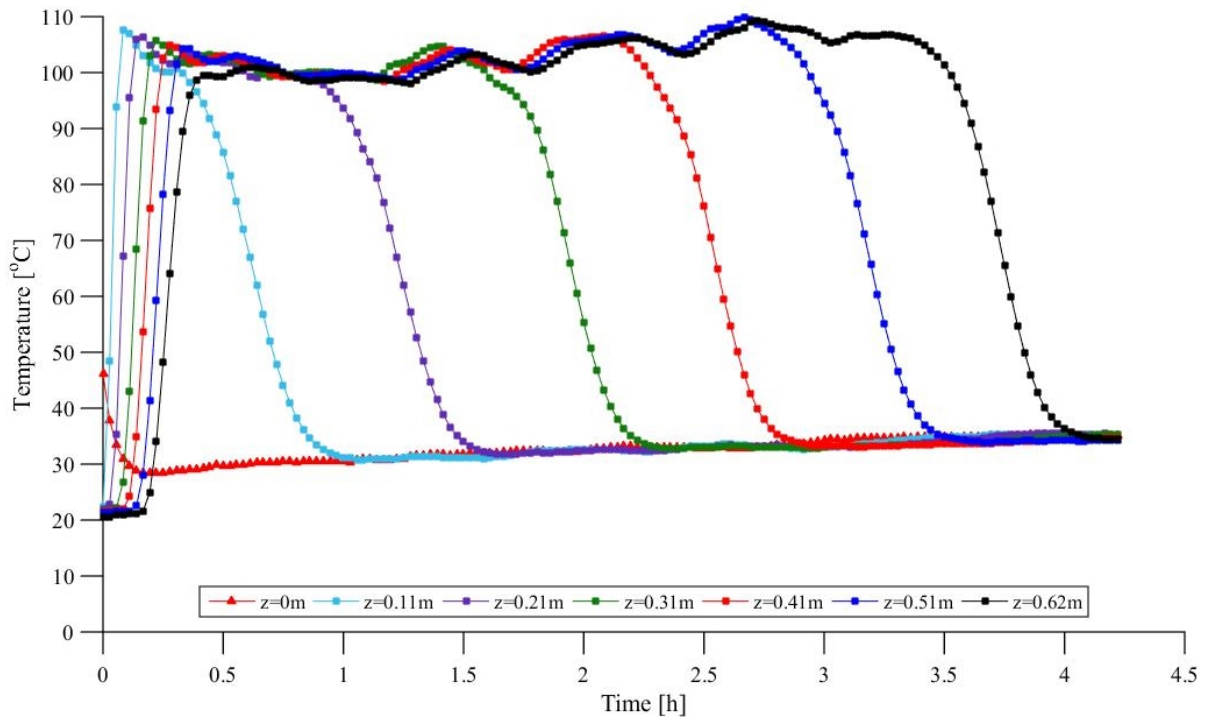


Figure B-7: Axial temperature profiles at various bed depths (z) - Discharging cycle 2

The humidity and mass flow rate results are presented in Figure B-8. The inlet humidity varied between 23 g_w/kg_{da} and 32 g_w/kg_{da}. The outlet humidity was approximately 0 g_w/kg_{da} during the cycle. Since the HTM2500LF humidity sensor has a temperature limit of 85 °C, it was removed from the rig for when the outlet temperature approached 85 °C and reinserted (just after 4 h) when the outlet temperature started to decrease. The outlet humidity approaches the value of the inlet humidity towards the end of the cycle indicating that no more water is being adsorbed and the discharging process is complete. The mass flow rate ranged between 176 kg/h and 179 kg/h which was consistent with discharging cycle 1.

The radial temperature profiles are presented in Figure B-9. The results were consistent with that of the previous cycle, in terms of the behaviour exhibited by the packed bed, at the different radial locations.

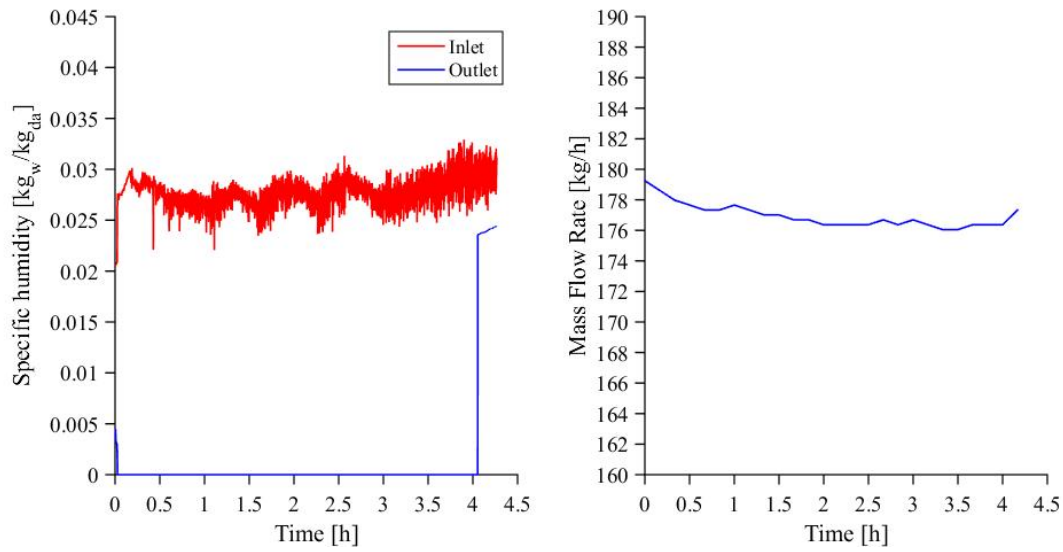


Figure B-8: Humidity and Mass flow rate - Discharging cycle 2

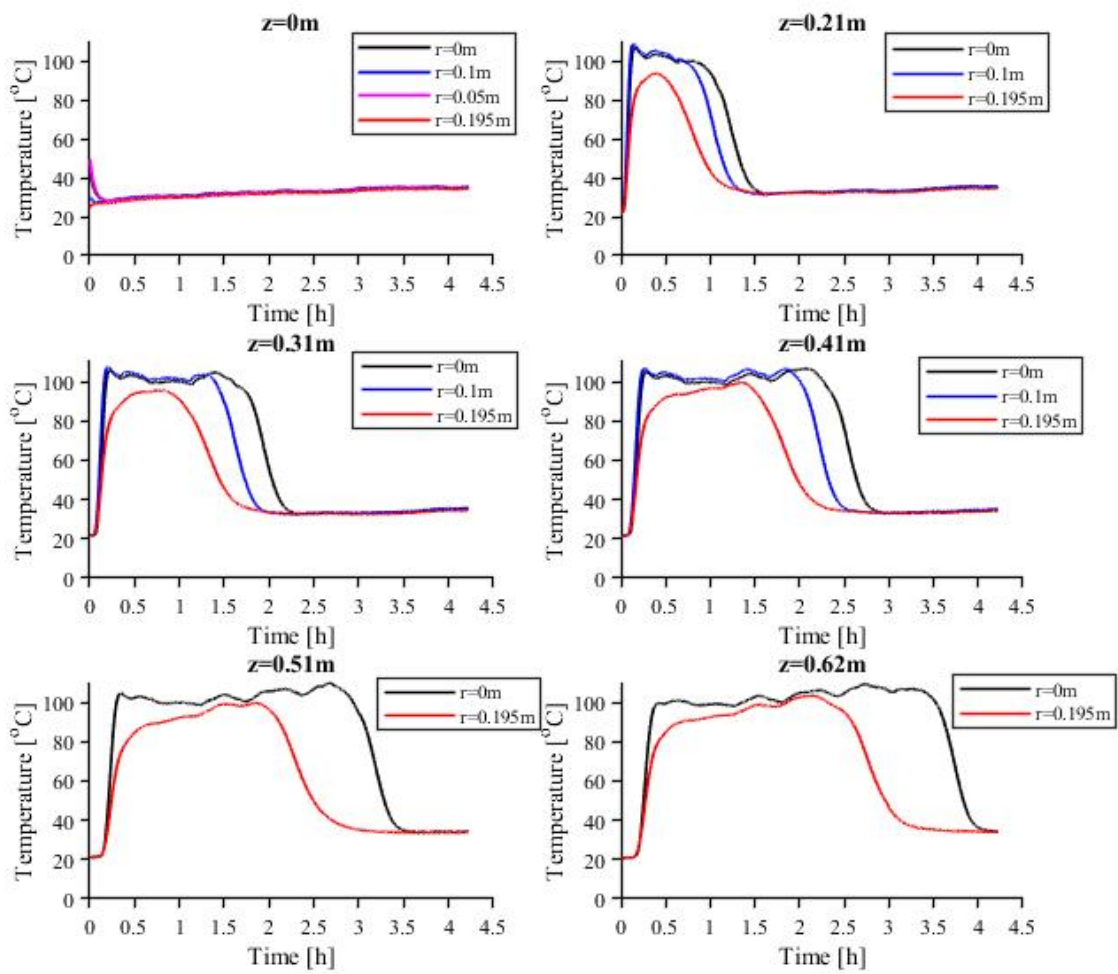


Figure B-9: Radial temperature profiles at various bed depths (z) - Discharging cycle 2

The energy released during discharging cycle 2 is presented in Figure B-10. A maximum of 3.6 kW was released during this discharging cycle. The total energy discharged was 11.50 kWh which was slightly lower than discharging cycle 1.

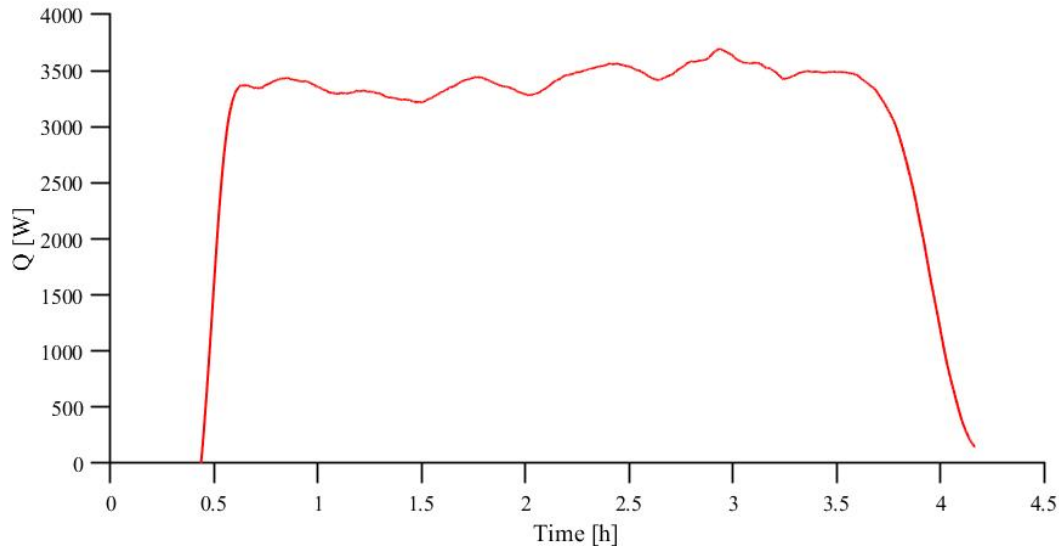


Figure B-10: Heat released - Discharging cycle 2

Discharging Cycle 3: ~25% RH

The third discharging cycle was performed on a very hot and dry day. The temperature profiles are presented in Figure B-11. The temperature increase was only 38 °C which was significantly lower than discharging cycle 1 result of 108 °C. This implies that the temperature lift is a significant function of the humidity of the air entering the reactor as mentioned by Mette et al (Section 2.6.3) [5]. The adsorption process also took 7 hours compared to 3 in the first test. This is due to the lower humidity supplied to the reactor and lower adsorption rate. The outlet of the bed took approximately 30 min to heat up as also seen in the previous two tests which implies that it is not affected by humidity.

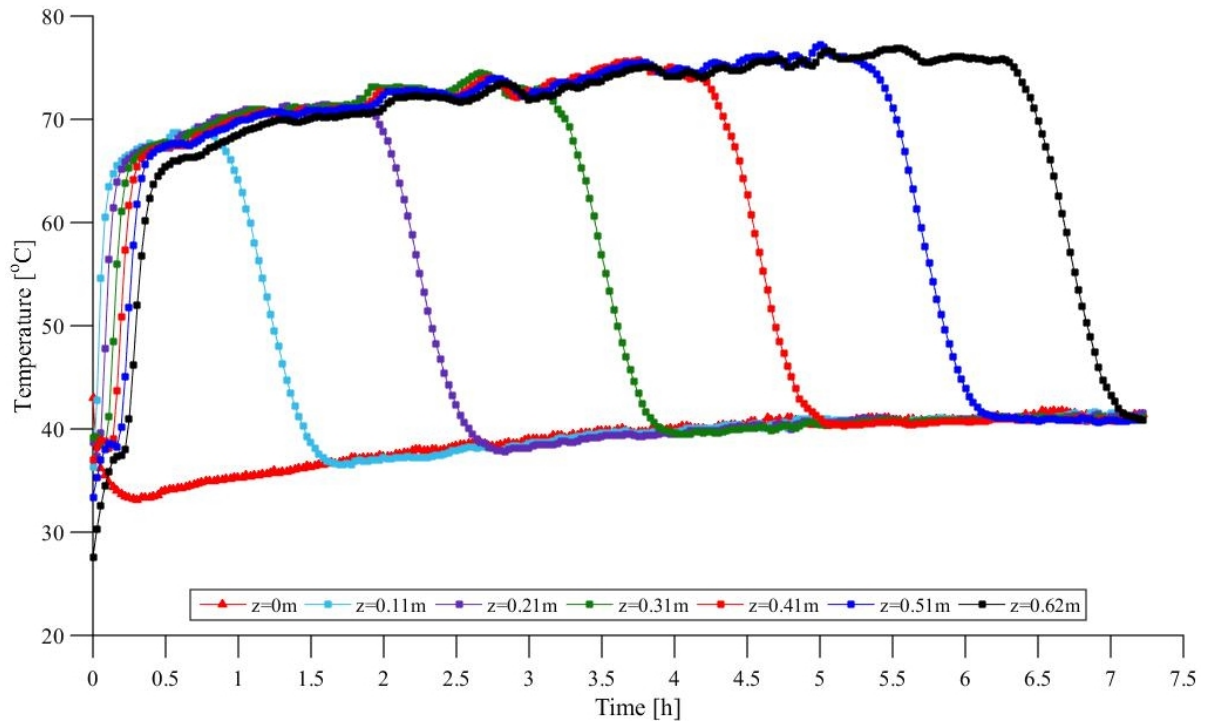


Figure B-11: Axial temperature profiles at various bed depths (z) - Discharging cycle 3

The humidity and mass flow rate results are presented in Figure B-12. The inlet humidity was approximately $12 \text{ g}_w/\text{kg}_{da}$ for the test. Since the outlet temperature did not exceed the temperature limit of the humidity sensors (of $85 \text{ }^\circ\text{C}$), the outlet humidity was recorded for the entire test. The outlet humidity was $0 \text{ g}_w/\text{kg}_{da}$ for most of the test i.e. roughly 6.7 h. It then rapidly rose to the inlet humidity indicating that no more water was being adsorbed and the adsorption cycle was complete. The mass flow rate ranged between 168 kg/h and 173 kg/h which was slightly lower than the previous tests.

The radial temperature profiles are presented in Figure B-13 . Similar behaviour was exhibited by the packed bed, at the different radial locations, as the previous tests.

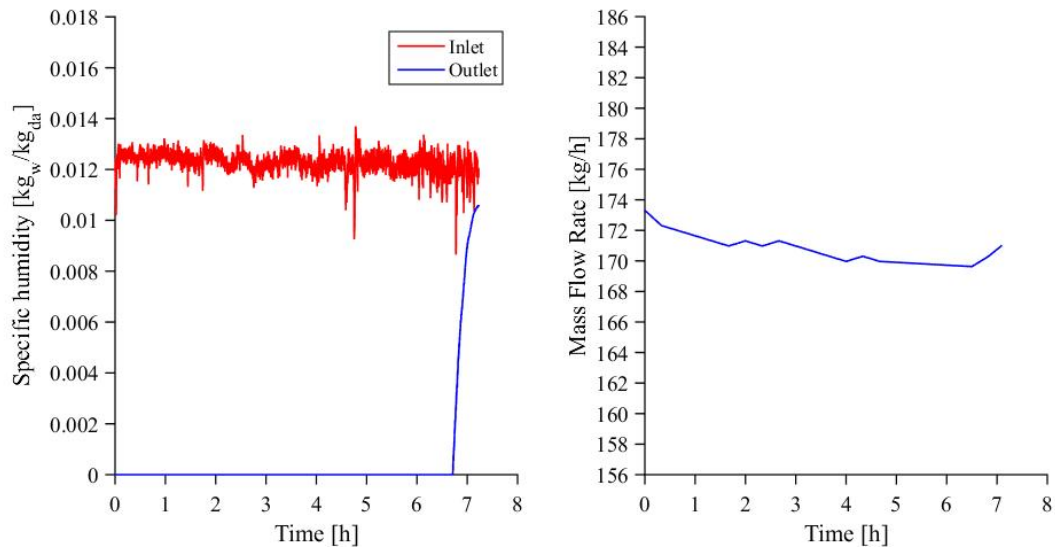


Figure B-12: Humidity and Mass flow rate - Discharging cycle 3

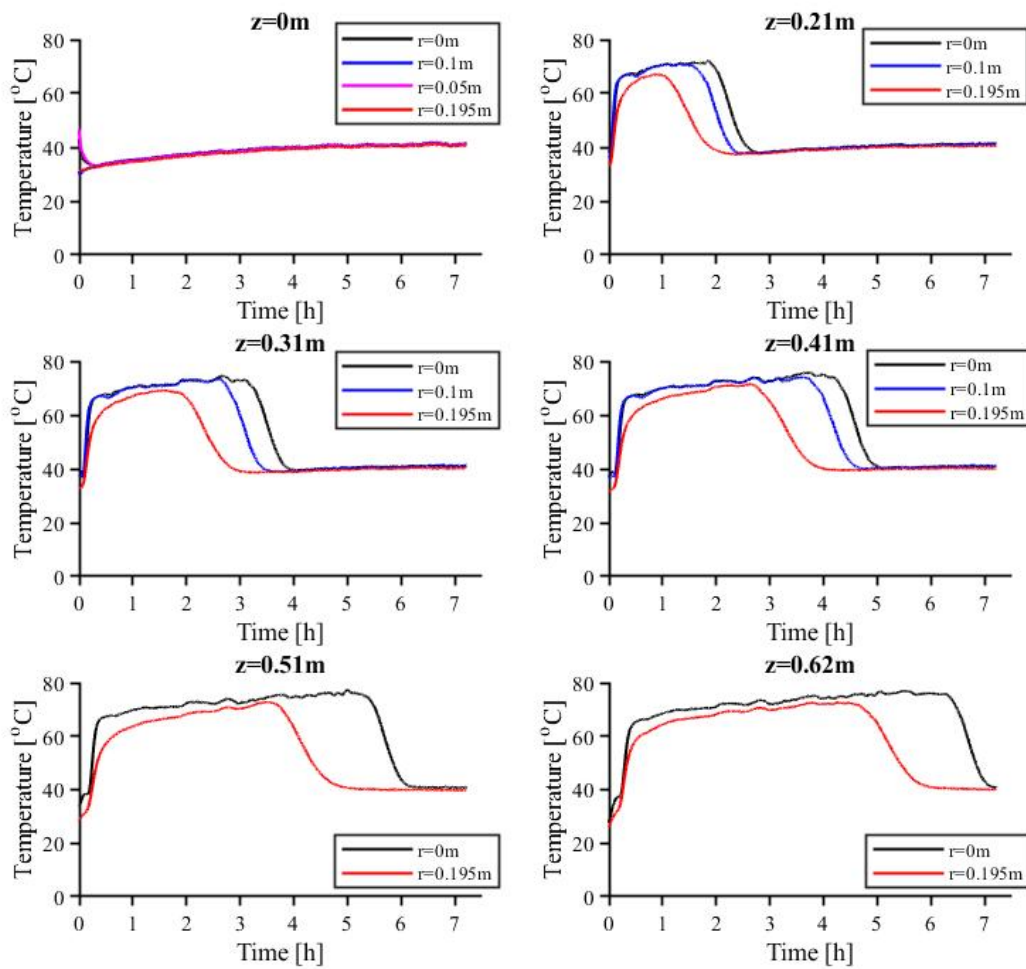


Figure B-13: Radial temperature profiles at various bed depths (z) - Discharging cycle 3

The energy released during discharging cycle 3 is presented in Figure B-14. A maximum of 1.6 kW was released during discharging cycle 3. The total energy discharged was 10.20 kWh. The low humidity clearly affected the amount of energy released which is approximately 12% lower than discharging cycle 1.

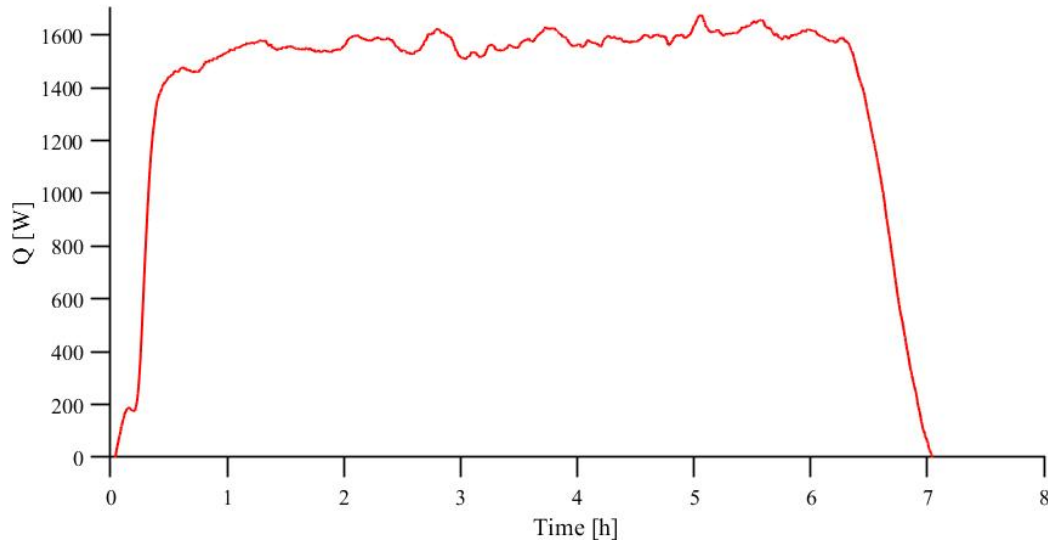


Figure B-14: Heat released - Discharging cycle 3

Discharging Cycle 4: 70% Flow rate

Discharging cycle 4 was performed at 70% of the maximum flowrate using a variable speed drive (VSD) to control the speed of the fan. The temperature profiles at the centre of the bed are presented in Figure B-15. The maximum temperature achieved was 95 °C. The cycle took approximately 6 h to complete which was longer than discharging cycle 2 (which lasted 4 h but at 100% flow rate) and was performed at a similar humidity as shown in Table 5-2. However, a temperature lift of 65 °C was achieved compared to 75 °C in discharging cycle 2, which could be due to the slightly lower humidity achieved in this test. The outlet of the bed took approximately 45 min to heat up which is longer than the 30 min observed in the previous tests which is due to the 30% reduction in flow rate.

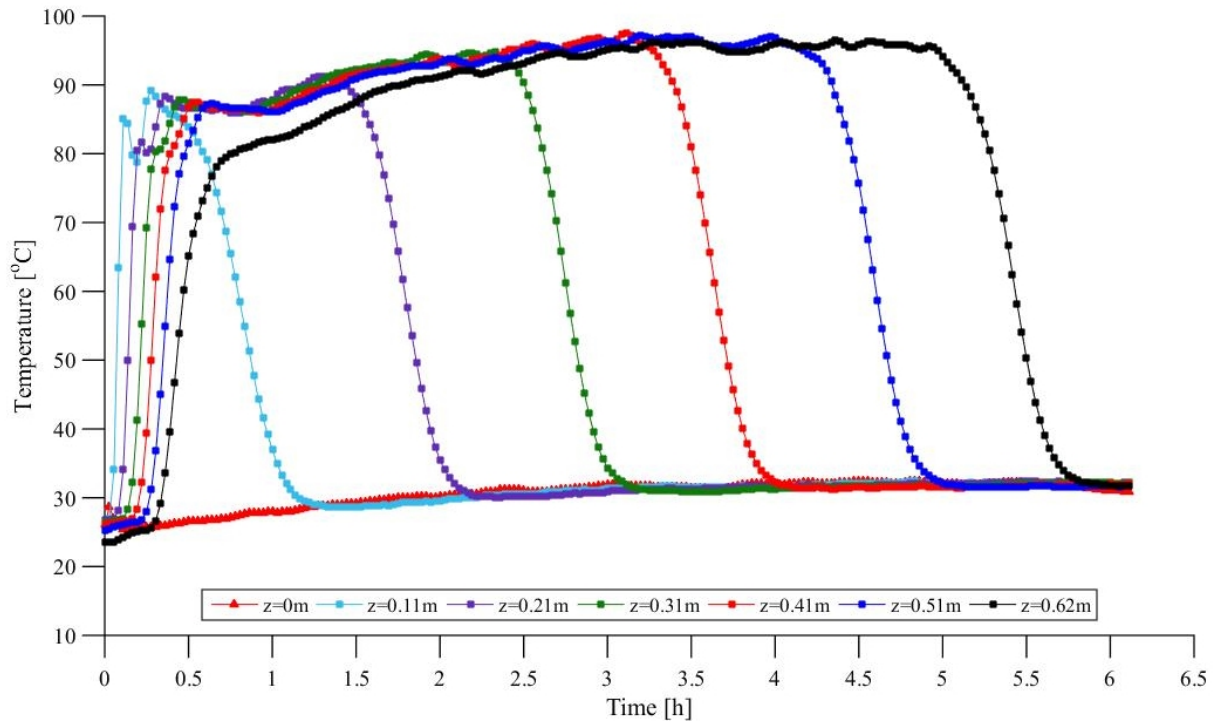


Figure B-15: Axial temperature profiles at various bed depths (z) - Discharging cycle 4

The humidity and mass flow rate results are presented in Figure B-16. The average inlet humidity was $23 \text{ g}_w/\text{kg}_{da}$ for the test. The outlet humidity was $0 \text{ g}_w/\text{kg}_{da}$ from $t = 0 \text{ h}$ to $t = 5.3 \text{ h}$. It then rapidly rose from $t = 5.3 \text{ h}$ to $t = 6 \text{ h}$ indicating that the adsorption cycle was nearing completion. The mass flow rate ranged between 125 kg/h and 128 kg/h , which was approximately 70% of the mass flow rate in the previous tests since the speed of the fan was adjusted to 70% (35 out of 50 Hz).

The radial temperature profiles are presented in Figure B-17. Similar behaviour was exhibited by the packed bed, at the different radial locations, as the previous tests. However, the channelling effects at $r = 0.1 \text{ m}$ were less evident at a lower flow rate.

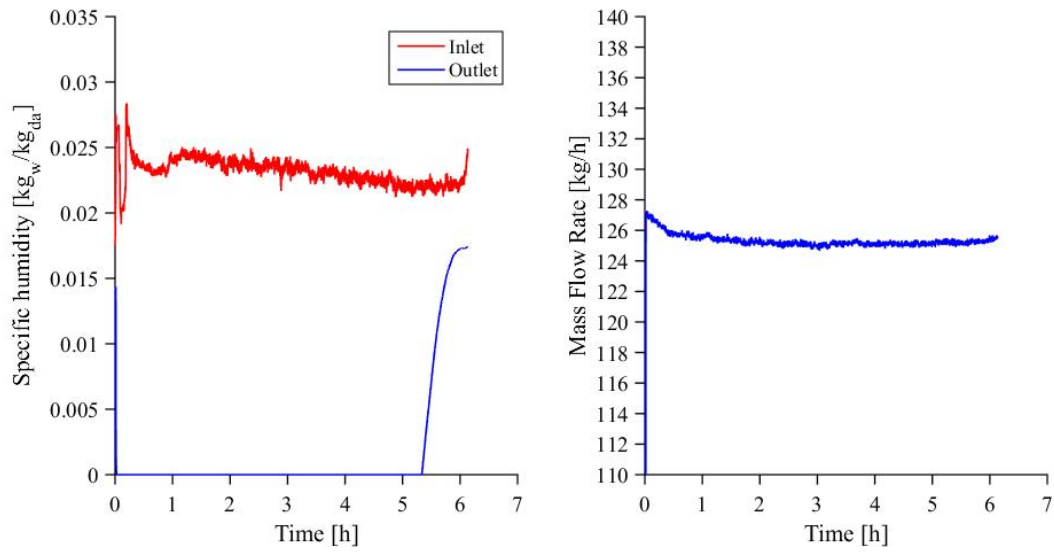


Figure B-16: Humidity and Mass flow rate - Discharging cycle 4

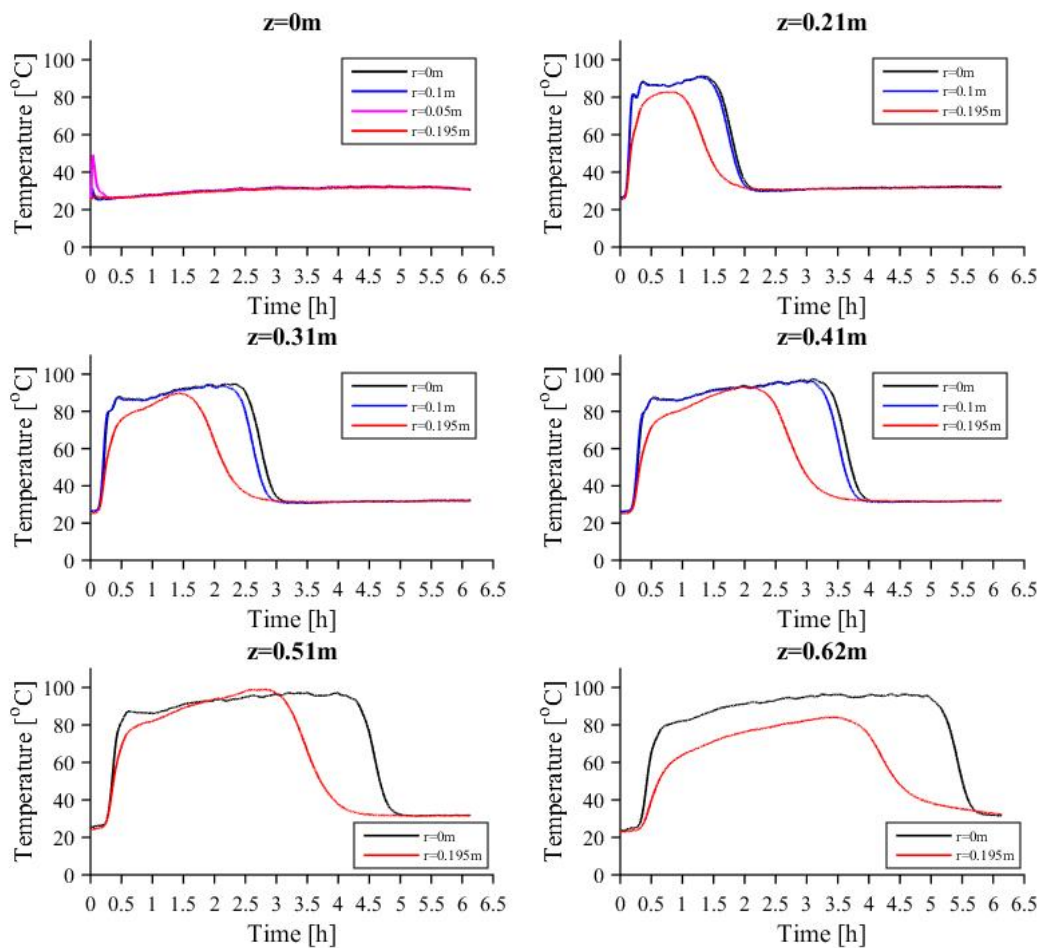


Figure B-17: Radial temperature profiles at various bed depths (z) - Discharging cycle 4

The energy released during discharging cycle 4 is presented in Figure B-18. A maximum of 2.2 kW was released during discharging cycle 4. The total energy discharged was 10.19 kWh. The lower flow rate affected the amount of energy released from the packed bed.

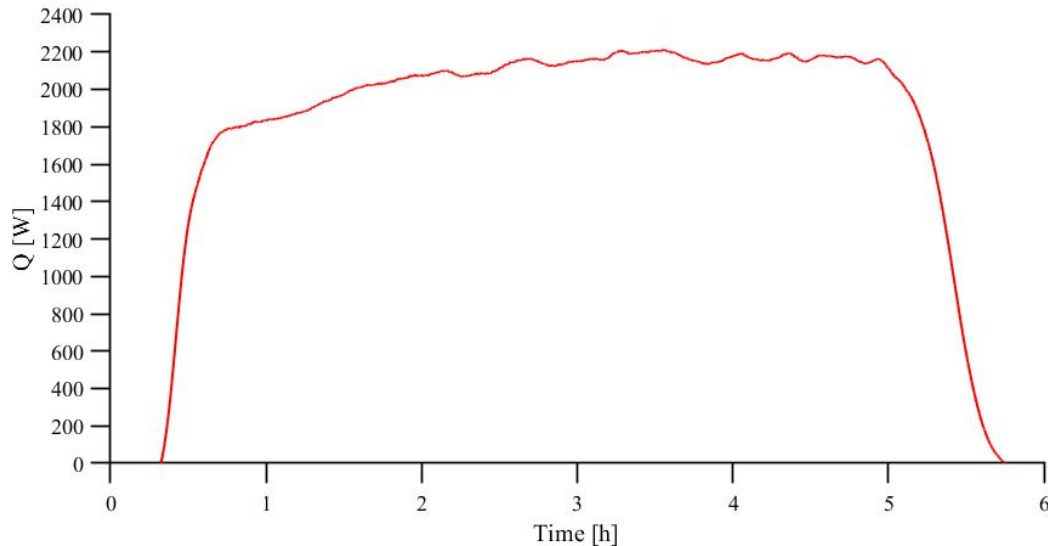


Figure B-18: Heat released - Discharging cycle 4

Discharging Cycle 5: 50% Flow rate

Discharging cycle 5 was performed at 50% of the maximum flowrate, again using a VSD to control the speed of the fan. The temperature profiles at the centre of the bed are presented in Figure B-19. A huge decrease in temperature is noticed from $t = 1.6$ h onwards. This is due to a significant drop that occurred in the ambient humidity where the relative humidity dropped from 37% to 20% in 2 h which equates to a drop of approximately $5 \text{ g}_w/\text{kg}_{da}$. Since the humidifier was controlled manually, it was difficult to compensate for the drop in ambient humidity and therefore fluctuations in temperature occurred before the temperature finally levelled off at $t = 4$ h.

The maximum temperature achieved was 90°C . The cycle took approximately 9 h to complete which was longer than discharging cycle 4 (which lasted 6 h at 70% flow rate) and was performed at a similar humidity. However, a temperature lift of 60°C was achieved compared to 65°C in discharging cycle 2, although the humidity was slightly higher in this test. This indicates that a lower flow rate only influences the temperature lift slightly. The outlet of the bed took approximately 1 h to heat up which was longer than the 45 min observed in the previous test. This indicates that a lower flow rate influences the time taken for the outlet temperature to increase. This is because the flow rate affects the rate at which the thermocline moves along the height of the reactor [50].

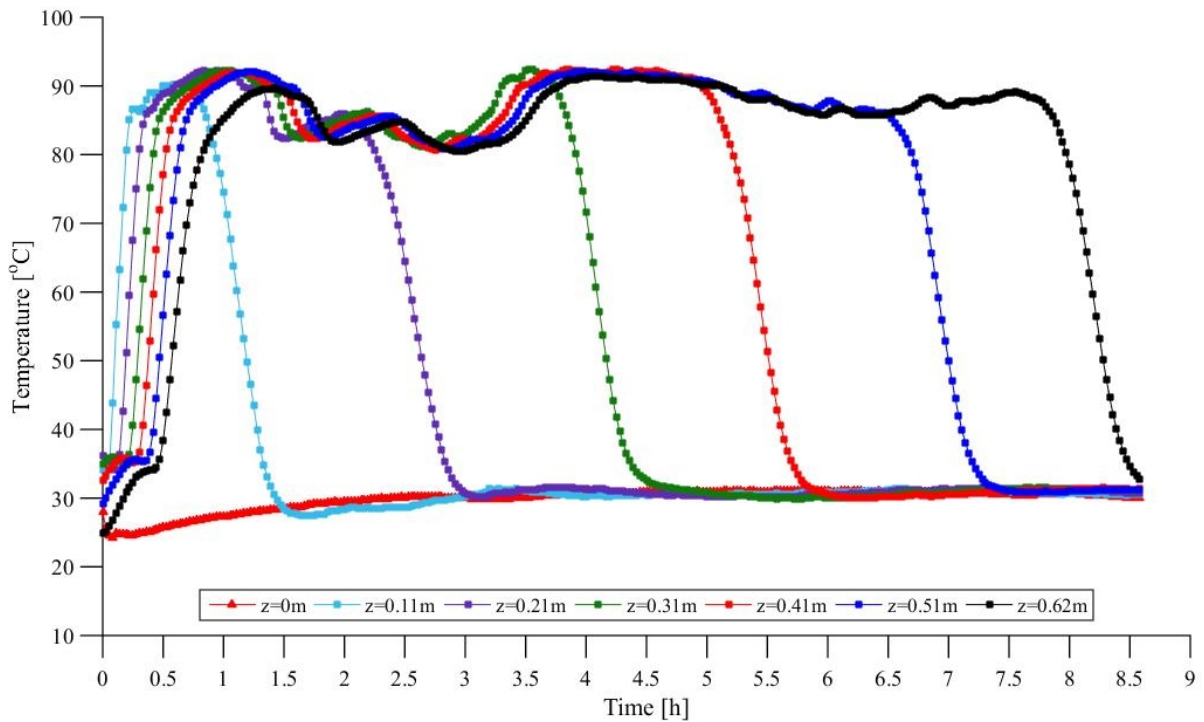


Figure B-19: Axial temperature profiles at various bed depths (z) - Discharging cycle 5

The humidity and mass flow rate results are presented in Figure B-20. The average inlet humidity was $24 \text{ g}_w/\text{kg}_{\text{da}}$ for the test. The fluctuations in the inlet humidity are due to the drastic change in ambient humidity as explained above. The outlet humidity was $0 \text{ g}_w/\text{kg}_{\text{da}}$ for the test. The mass flow rate ranged between 89 kg/h and 91 kg/h , which was approximately 50% of the mass flow rate in the previous tests since the frequency of the fan was adjusted to 25 Hz out of a maximum of 50 Hz.

The radial temperature profiles are presented in Figure B-21. Similar behaviour was exhibited by the packed bed, at the different radial locations, as discharging cycles 1-3. However, the channelling effects, at $r = 0.1 \text{ m}$ as noted with the 70% flow rate test, is now clearly less due to the lower flow rate through the packed bed.

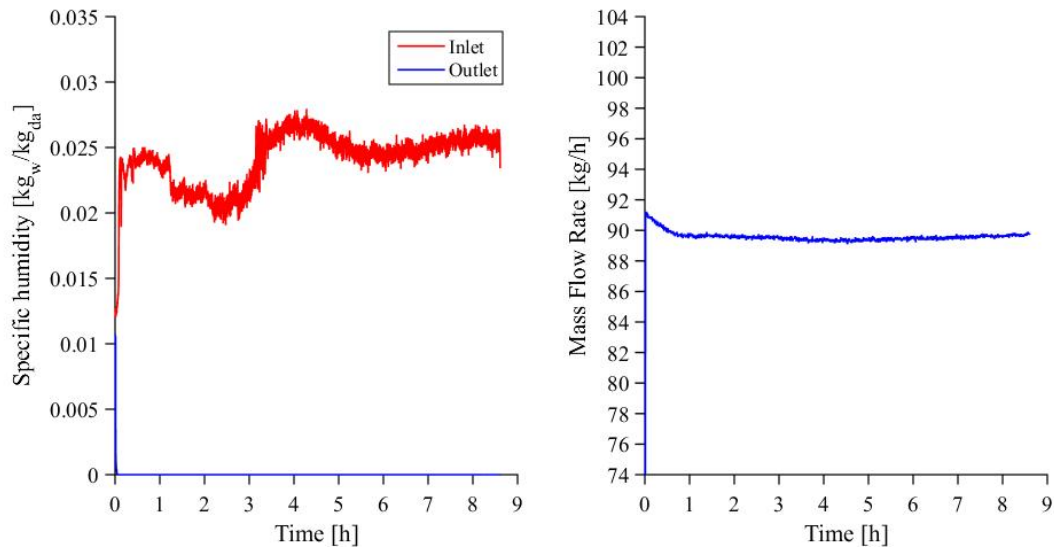


Figure B-20: Humidity and Mass flow rate - Discharging cycle 5

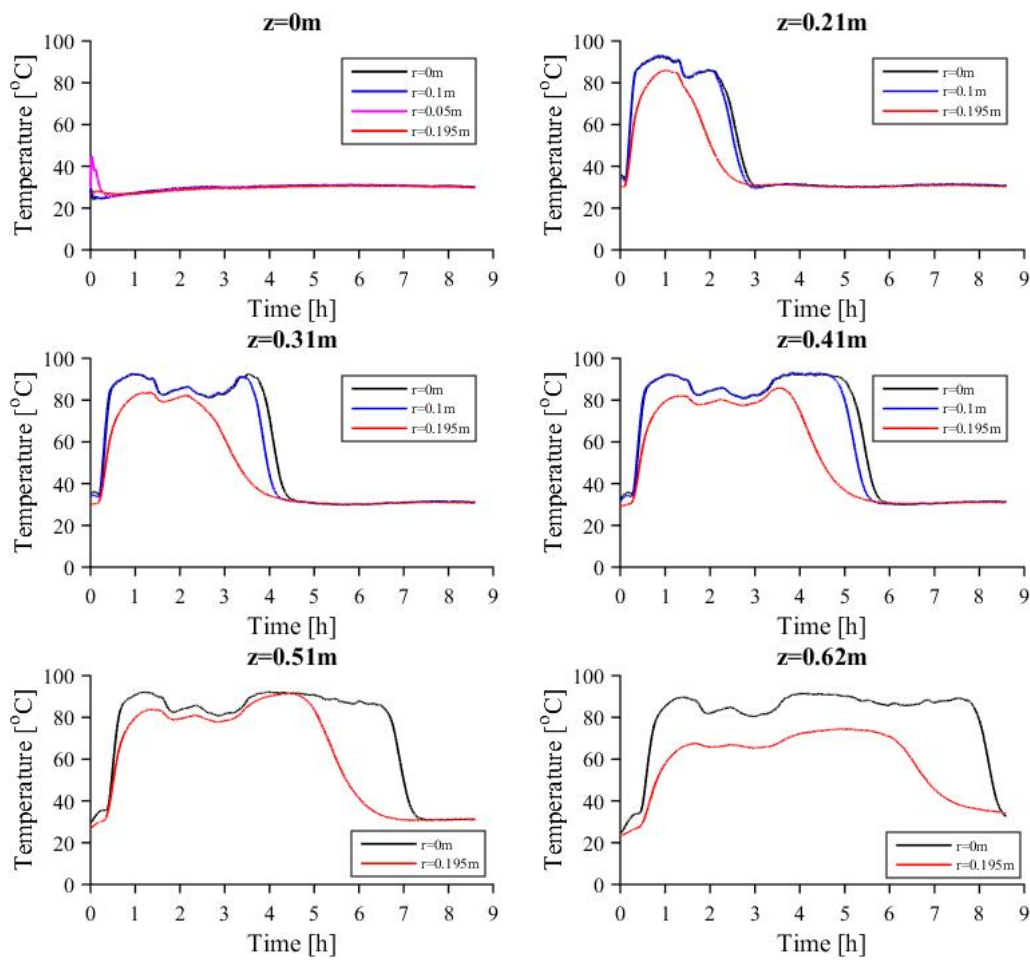


Figure B-21: Radial temperature profiles at various bed depths (z) - Discharging cycle 5

The energy released during discharging cycle 5 is presented in Figure B-22. A maximum of 1.5 kW was released during discharging cycle 5. The total energy discharged was 10.48 kWh. The trend of the lower flow rate leading to a decrease in energy released is now clear. This is due to a lower adsorption rate which affects the amount of energy released as mentioned by [41] in Section 2.5.6.

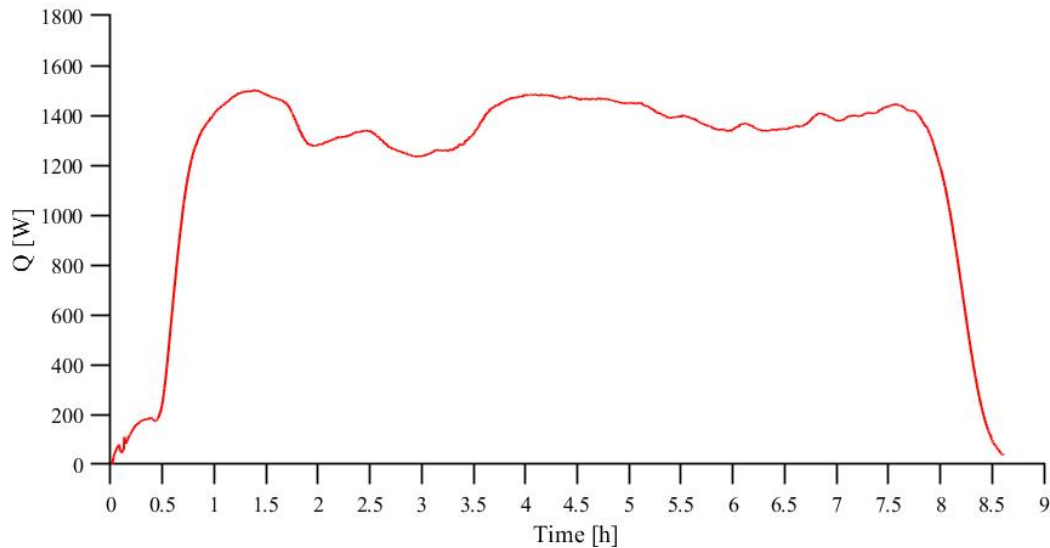


Figure B-22: Heat released - Discharging cycle 5

Discharging Cycle 6: 160 °C Regeneration temperature

The axial temperature profiles are presented in Figure B-23. The packed bed was regenerated at 160 °C compared to 200 °C in the previous tests. The temperature of the ambient air that was supplied to the inlet of the reactor was 24 °C. The maximum temperature realised at the outlet of the reactor was 83 °C which equates to a temperature increase of 58 °C across the reactor. It took approximately 5 hours for the cycle to complete. The outlet of the bed took approximately 30 min to heat up as also seen in discharging cycles 1-3.

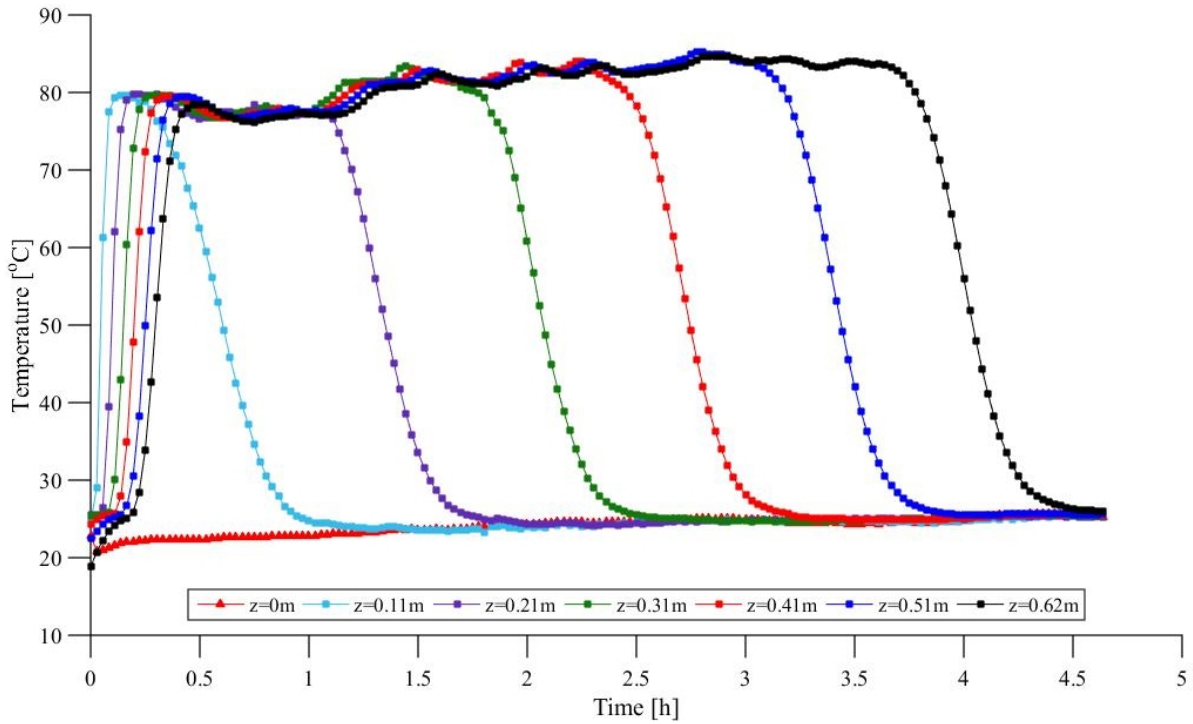


Figure B-23: Axial temperature profiles at various bed depths (z) - Discharging cycle 6

The humidity and mass flow rate results are presented in Figure B-24. The average inlet humidity was $19 \text{ g}_w/\text{kg}_{da}$ for the test. The outlet humidity was $0 \text{ g}_w/\text{kg}_{da}$ for most of the test before rising (from $t = 3.8 \text{ h}$) to the inlet humidity at the end of the test. The mass flow rate ranged between 180 kg/h and 183 kg/h , which was within 2% of discharging cycles 1 and 2.

The radial temperature profiles are presented in Figure B-25. Similar behaviour was exhibited by the packed bed, at the different radial locations, as the previous tests.

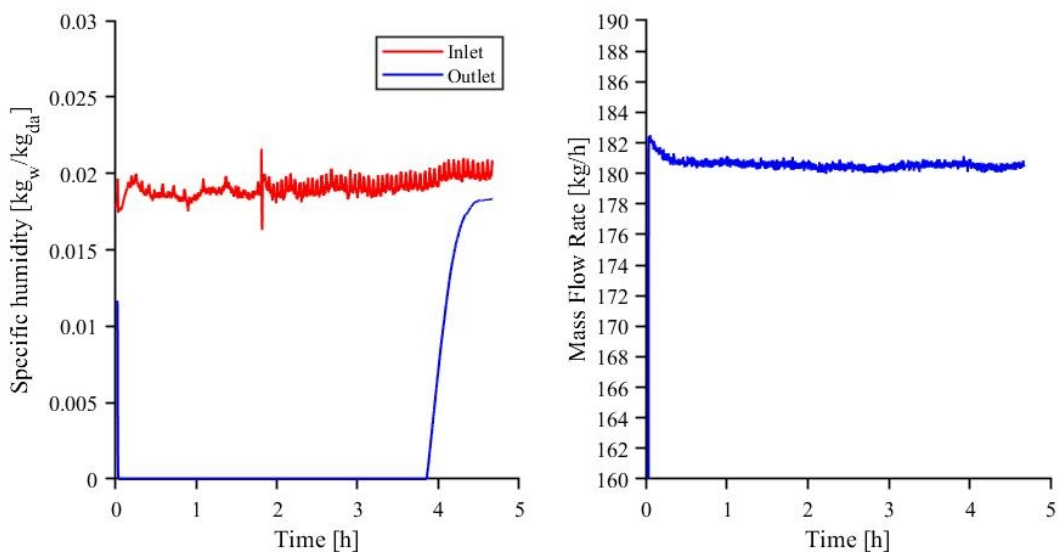


Figure B-24: Humidity and Mass flow rate - Discharging cycle 6

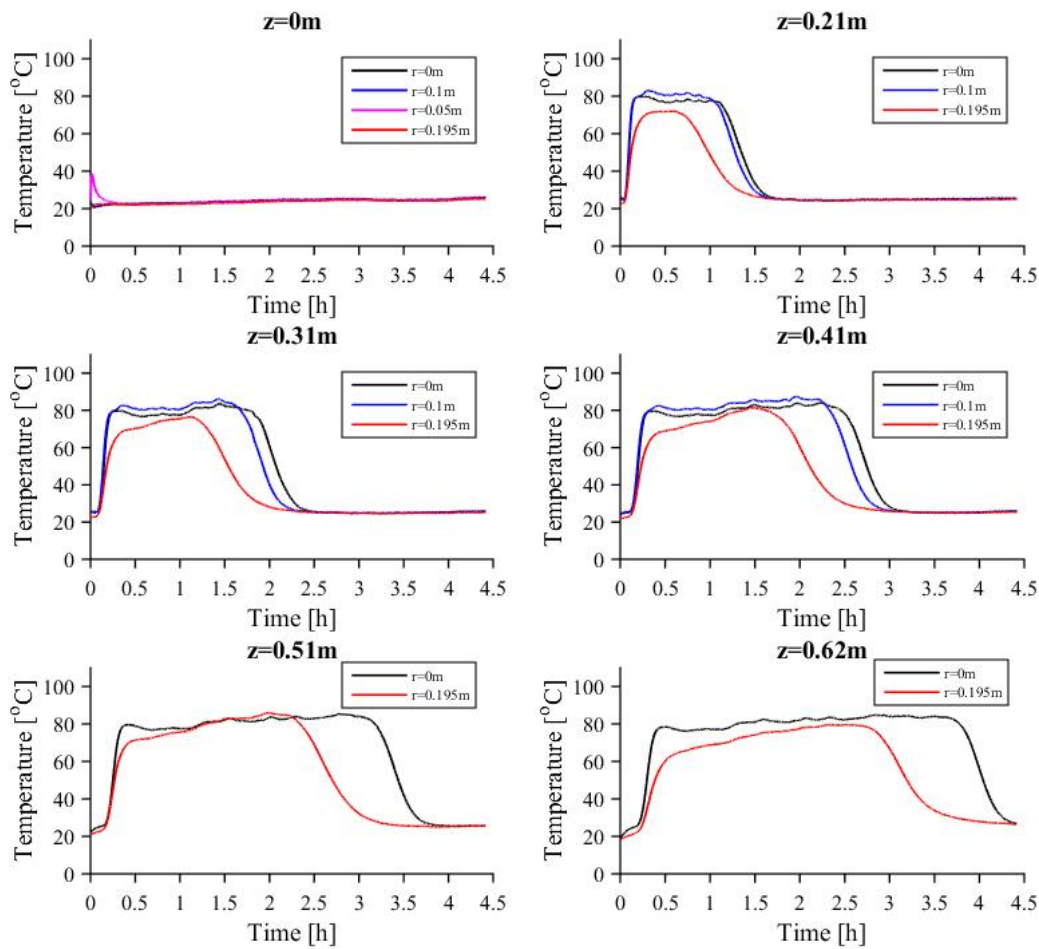


Figure B-25: Radial temperature profiles at various bed depths (z) - Discharging cycle 6

The energy released during discharging cycle 6 is presented in Figure B-26. A maximum of 2.9 kW was released during discharging cycle 6. The total energy discharged was 10.73 kWh. The lower regeneration temperature did not affect the amount of energy released significantly as the amount of energy released during this cycle is slightly greater than discharging cycle 3 (10.20 kWh) which was performed after a regeneration temperature of 200 °C. However it should be noted that the humidity was higher for this test (19 g_w/kg_{da}) compared to 12 g_w/kg_{da} in discharging cycle 3 which also affects the amount of energy released.

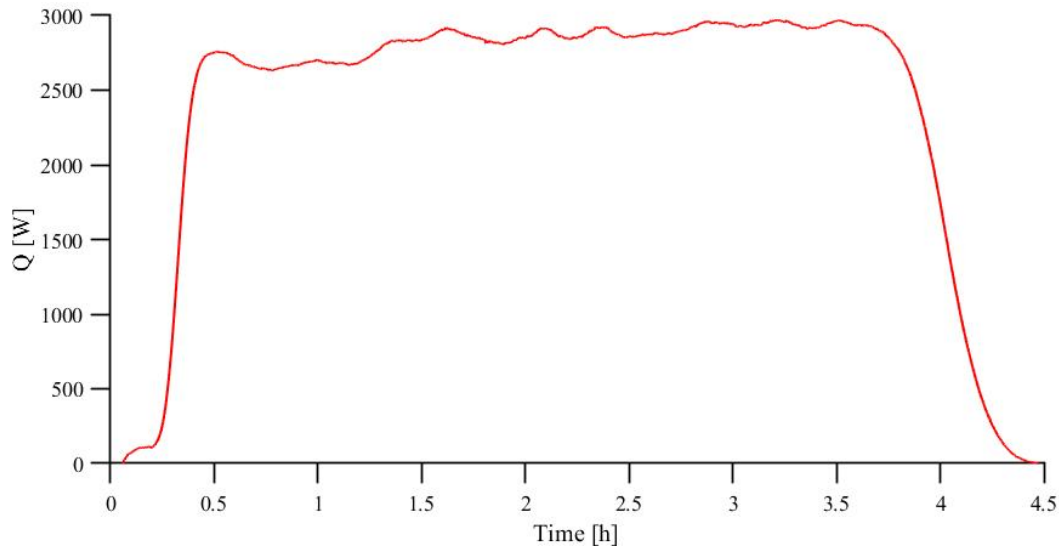


Figure B-26: Heat released - Discharging cycle 6

Discharging Cycle 7: 130 °C Regeneration temperature

The axial temperature profiles are presented in Figure B-27. The packed bed was regenerated at 130 °C compared to 200 °C for the majority of the tests. The average temperature of the ambient air that was supplied to the inlet of the reactor was 33 °C. It should be noted that there was a steep rise in the ambient temperature from 22 °C at the beginning of the test to 34 °C at the end. Therefore, the outlet temperature did not vary much during the test even though the specific humidity at the inlet to the packed bed decreased noticeably (refer to Figure B-28). The maximum temperature realised at the outlet of the reactor was 61 °C, which equates to a temperature increase of 28 °C across the reactor. This was the lowest temperature lift achieved during testing as shown in Table 5-2. It took approximately 8 hours for the cycle to complete. The outlet of the bed took approximately 30 min to heat up as seen in the previous test.

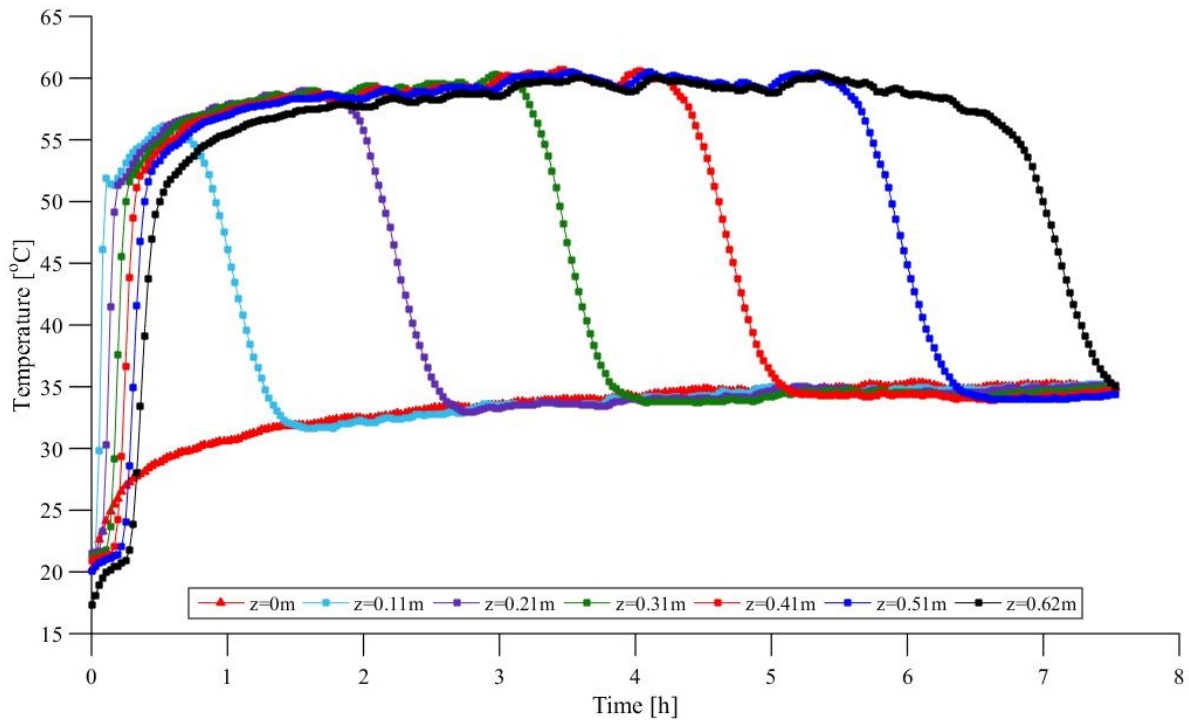


Figure B-27: Axial temperature profiles at various bed depths (z) - Discharging cycle 7

The humidity and mass flow rate results are presented in Figure B-28. The average inlet humidity was $7 \text{ g}_w/\text{kg}_{da}$ for the test. This was the lowest inlet humidity measured during testing. There was a significant change in humidity from $9 \text{ g}_w/\text{kg}_{da}$ (at the beginning of the test) to $5 \text{ g}_w/\text{kg}_{da}$ at the end of the test. The outlet humidity was $0 \text{ g}_w/\text{kg}_{da}$ for most of the test before rising (from $t = 7 \text{ h}$) to match the inlet humidity at the end of the test. The mass flow rate ranged between 163 kg/h and 167 kg/h , which was lower than the previous test. This could be due to the higher ambient temperature and lower ambient humidity.

The radial temperature profiles are presented in Figure B-29. At lower temperatures the difference between the axial and wall temperatures are minimal i.e., the heat losses are lower. However, the adsorption process still occurs faster at the wall due to the higher fluid velocity in the wall region and channelling still occurred at $r = 0.1 \text{ m}$.

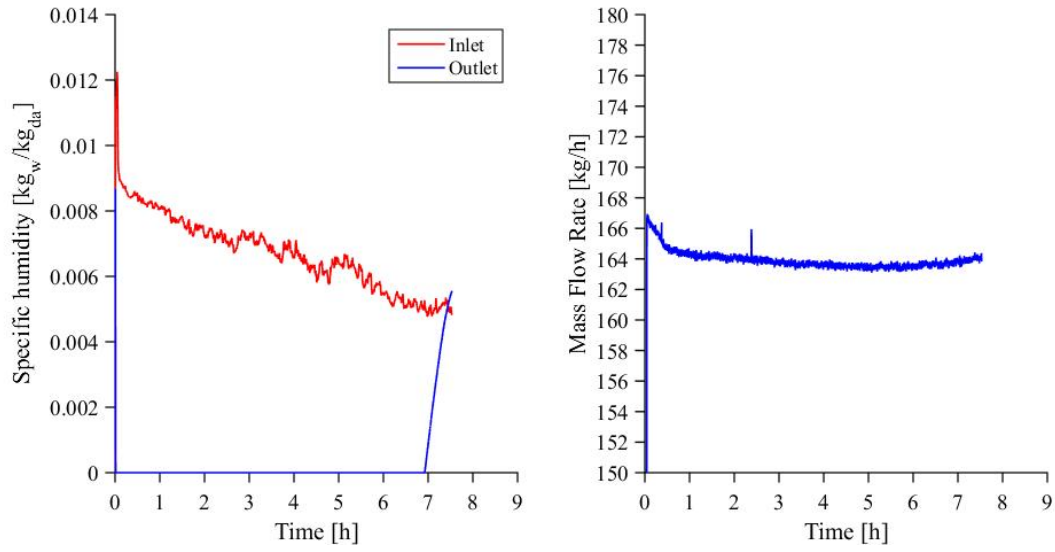


Figure B-28: Humidity and Mass flow rate - Discharging cycle 7

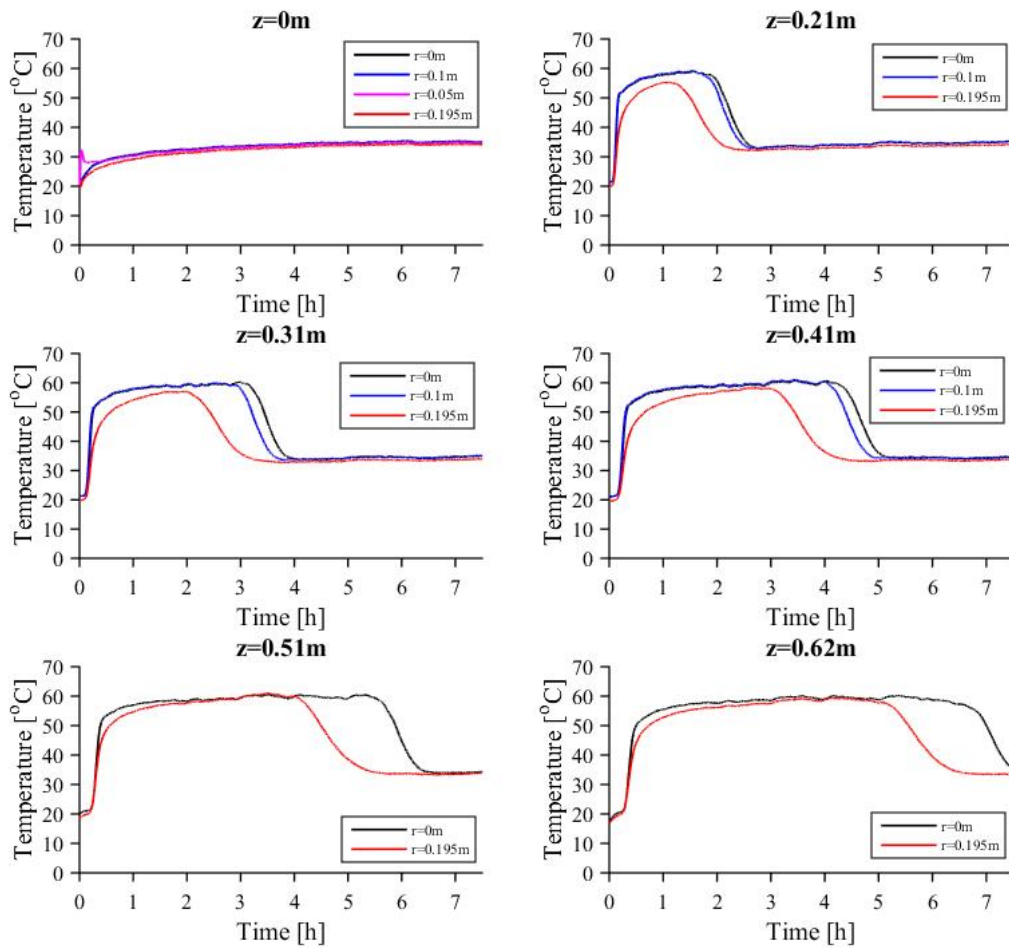


Figure B-29: Radial temperature profiles at various bed depths (z) - Discharging cycle 7

The energy released during discharging cycle 7 is presented in Figure B-30 . A maximum of 1.1 kW was released during discharging cycle 7. The total amount of energy discharged was 7.50 kWh. This implies that very low regeneration temperatures lower the amount of energy released as this was the lowest from all the cycles. However, it should be noted that the humidity was the lowest for this test ($7 \text{ g}_w/\text{kg}_{\text{da}}$) and this was also a factor with regards to the amount of energy released during this cycle.

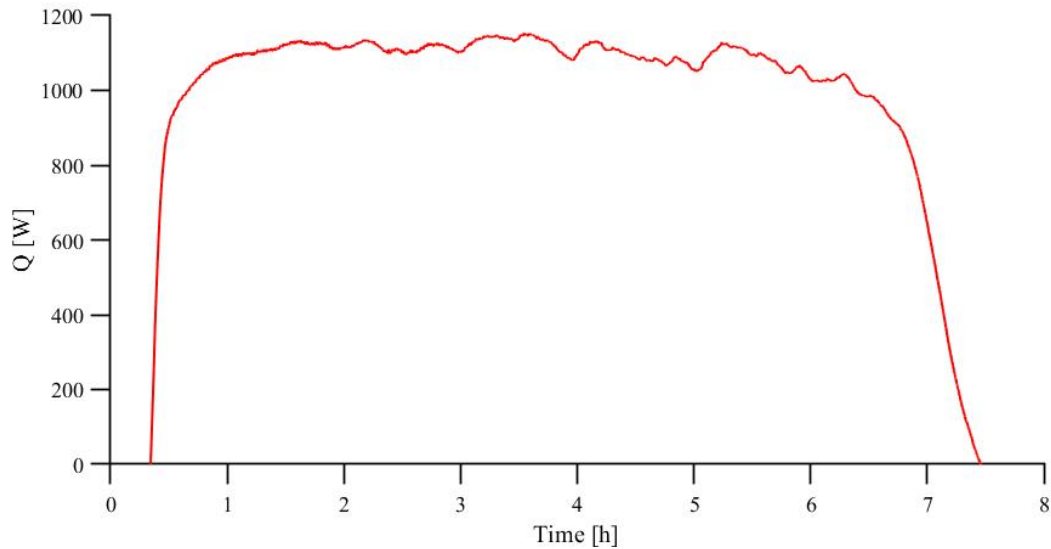


Figure B-30: Heat released - Discharging cycle 7

Discharging Cycle 8: 5 months after regeneration

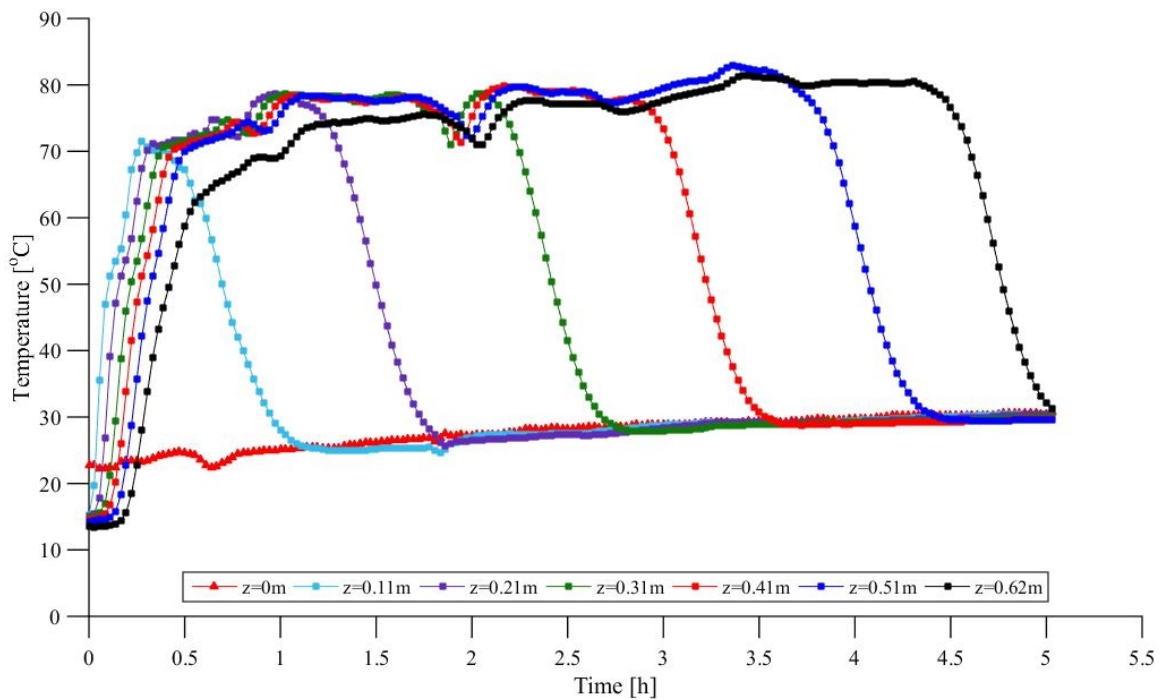


Figure B-31: Axial temperature profiles at various bed depths (z) - Discharging cycle 8

The humidity and mass flow rate results are presented in Figure B-32. The humidity entering the reactor was maintained at approximately 20 g_w/kg_{da}. The humidity at the outlet of the reactor was 0 g_w/kg_{da} for most of the cycle implying that all the water vapour entering the reactor was being adsorbed by the zeolite. The maximum mass flow rate was 174.5 kg/h and varied by approximately 2% during the test.

The radial temperature profiles are presented in Figure B-33. Similar behaviour was exhibited by the packed bed, at the different radial locations, as the previous tests.

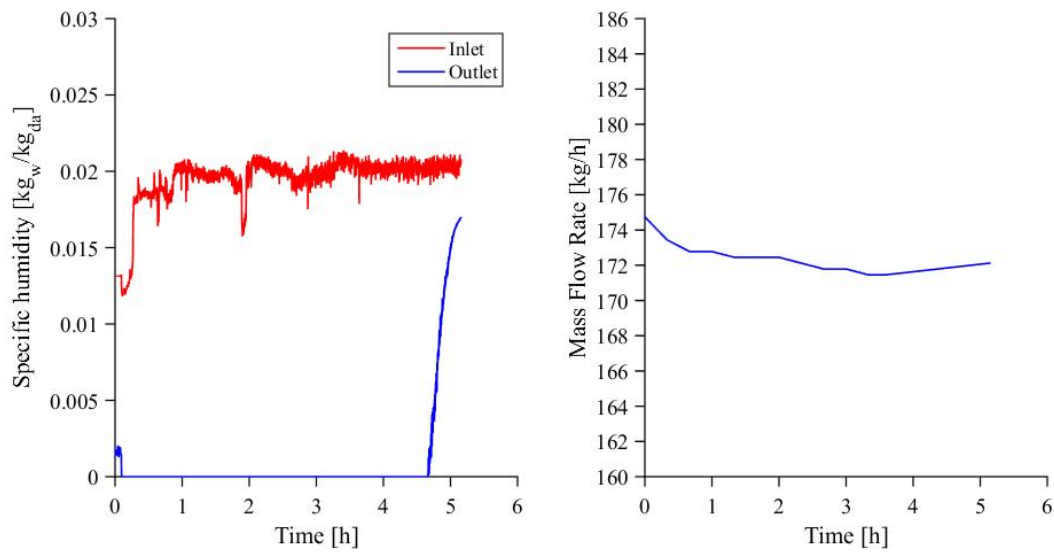


Figure B-32: Humidity and Mass flow rate - Discharging cycle 8

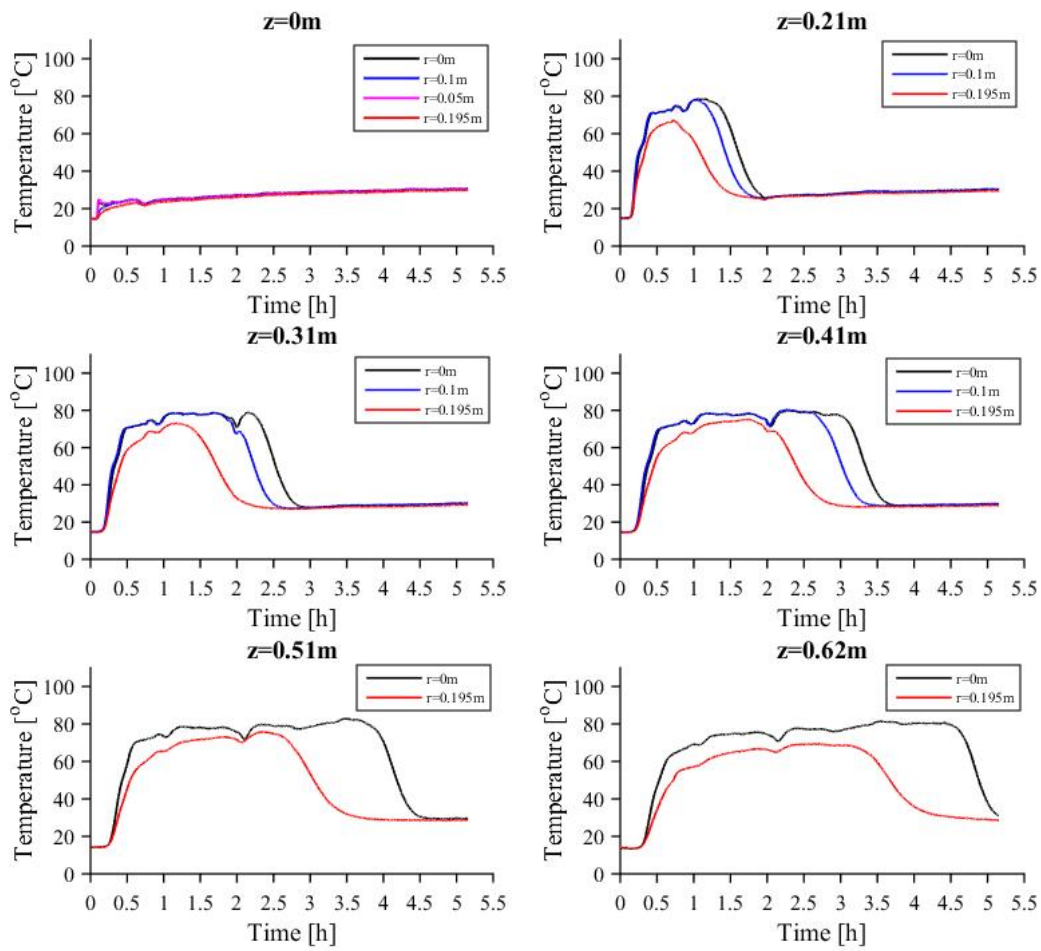


Figure B-33: Radial temperature profiles at various bed depths (z) - Discharging cycle 8

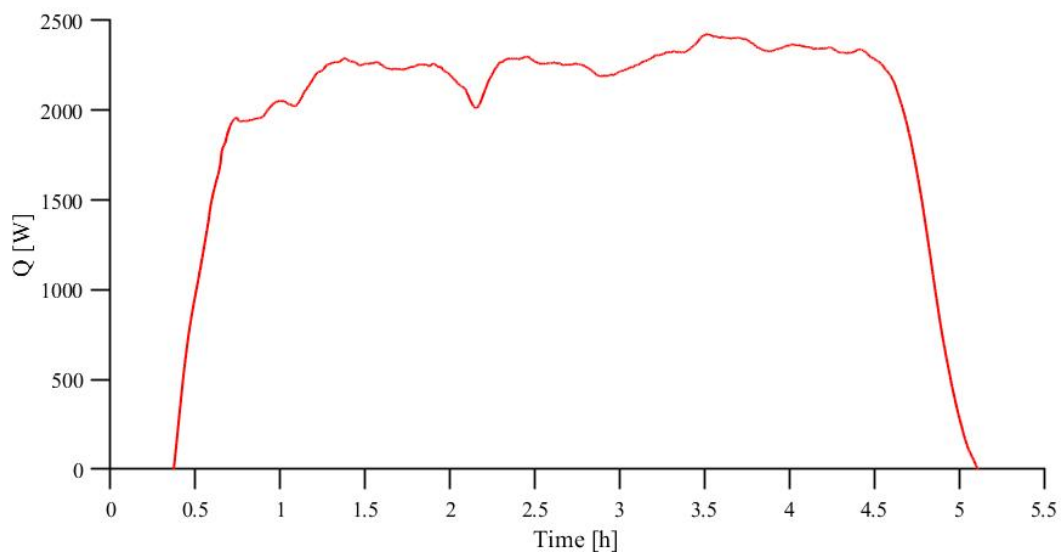


Figure B-34: Heat released - Discharging cycle 8

Appendix C: Sample Calculation for Energy Balance

A sample calculation for the first charging cycle (200 °C) and discharging cycle (100% RH) is presented. Calculations for the energy supplied, stored and released from the packed bed are included at a particular time step. Furthermore, the calculation for the charging, storage and discharging efficiencies for these cycles are also presented,

Charging Cycle 1

This calculation was performed at a time of 1 h for charging cycle 1 at the three different points in the system. ‘CoolProp’ was used through MATLAB to calculate the specific humidity from the temperature and relative humidity measured by the sensors. The enthalpy of water vapor/ steam (h_g) was also obtained from ‘CoolProp’. This enthalpy value can be read off the saturated steam tables. The mass flow rate was calculated in MATLAB using equations (A-1) to (A-2), based on the differential pressure measured across the conical inlet, for each time step. Furthermore, the equations (4-1) to (4-5) were used to determine the mass flow rates of water vapour (and dry air) at each point in the system. The data is summarised in Table C-1.

Table C-1: Data at three points in the system during charging cycle 1

	Conical inlet (Point 1)	Reactor Inlet (Point 2)	Reactor Outlet (Point 3)
Temperature [°C]	25	198	46
Humidity (x) [kg/kg]	0.013	0.013	0.045
Enthalpy of water vapour/ Steam (h_g) [kJ/kg]	2546	2792	2582
Mass flow rate of dry air (\dot{m}_{da}) [kg/s]	0.037	0.037	0.037
Mass flow rate of water vapour \dot{m}_w [kg/s]	0.00047	0.00047	0.00175

The Specific enthalpy formula for moist air is:

$$h = C_{p1,da}T + xh_g$$

Therefore, the energy at points 1-3 can be calculated as follows:

$$\dot{Q}_1 = \dot{m}_1 h_1 = \dot{m}_{da}C_{p,a}T_1 + \dot{m}_{1,w}x_1h_{1,g}$$

$$\dot{Q}_1 = (0.037)(1.007)(25) + (0.00047)(0.013)(2546)$$

$$\dot{Q}_1 = 0.95 \text{ kW}$$

$$\dot{Q}_2 = \dot{m}_{da} C_{p2,da} T_2 + \dot{m}_{2,w} x_2 h_{2,g}$$

$$\dot{Q}_2 = (0.037)(1.023)(198) + (0.00047)(0.013)(2792)$$

$$\dot{Q}_2 = 7.51 \text{ kW}$$

$$\dot{Q}_3 = \dot{m}_{da} C_{p3,da} T_3 + \dot{m}_{3,w} x_3 h_{3,g}$$

$$\dot{Q}_3 = (0.037)(1.007)(46) + (0.00175)(0.045)(2582)$$

$$\dot{Q}_3 = 1.92 \text{ kW}$$

The losses through the wall (between point 2 and 3) can be calculated from equations (4-16) to (4-19). The temperature of the air in the wall region is approximately 180 °C (Figure 5-3) and the ambient temperature was approximately 25 °C, therefore:

$$h_x = 1.42 \left(\frac{\Delta T}{L} \right)^{1/4}$$

$$h_x = 1.42 \left(\frac{180 - 25}{0.62} \right)^{1/4} = 5.646$$

$$h_w = \left(\frac{k_f}{2d_p} \right) [2.576 Re^{1/3} Pr^{1/3} + 0.0936 Re^{0.8} Pr^{0.4}]$$

$$h_w = \left(\frac{0.03779}{2(0.005)} \right) [2.576(61.76)^{1/3}(0.6974)^{1/3} + 0.0936(61.76)^{0.8}(0.6974)^{0.4}] = 42.414$$

$$U_w = \frac{1}{\frac{1}{A_0 h_w} + \frac{\ln[(r_0 + e)/r_0]}{2\pi L k_{iso}} + \frac{1}{A_x h_x}}$$

$$U_w = \frac{1}{\frac{1}{(0.1257)(42.415)} + \frac{\ln[(0.2) + e]/(0.2)}{2\pi(0.62)(0.06)} + \frac{1}{(1.0713)(5.646)}} = 0.0846$$

$$\dot{Q}_{loss,2-3} = U_w A_w \Delta T = 0.0846(0.779)(180 - 25) = 0.0102 \text{ kW}$$

The losses are less than 0.2% of the energy at \dot{Q}_2 and are therefore neglected in the calculations below.

Energy Supplied (Q_{in})

From equation (4-11) the energy supplied to the packed bed is:

$$\dot{Q}_{in} = \dot{Q}_2 - \dot{Q}_1 = 7.51 - 0.95 = 6.6 \text{ kW}$$

\dot{Q}_{in} is 6.6 kW at a time of 1 h which can be seen in Figure 5-5. Using ‘CoolProp’ and MATLAB, \dot{Q}_{in} was calculated for each data point and plotted in Figure 5-5. By integrating this curve (using the ‘trap(z)’ function in MATLAB), a value of 20.44 kWh (Q_{in}) was obtained which was the total amount of energy supplied to the packed bed for charging cycle one.

Energy Stored (Q_s)

From equation (4-14) the amount of energy stored in the packed bed can be calculated as follows:

$$\dot{Q}_s = \dot{Q}_3 - \dot{Q}_2 = 7.51 - 1.92 = 5.6 \text{ kW}$$

The energy stored was plotted in Figure 5-5 for each time step. The total amount of energy stored in the packed bed was 13.64 kWh (Q_s) for charging cycle 1.

Discharging Cycle 1

This calculation was performed at a time of 1 h for discharging cycle 1 at the three different points in the system. The data is summarised in Table C-2.

Table C-2: Data at three points in the system during discharging cycle 1

	Conical inlet (Point 1)	Reactor Inlet (Point 2)	Reactor Outlet (Point 3)
Temperature [°C]	17	32	130
Humidity (x) [kg/kg]	0.014	0.035	0
Enthalpy of water vapour/ Steam (h_g) [kJ/kg]	2530	2559	2720
Mass flow rate of dry air (\dot{m}_{da}) [kg/s]	0.049	0.049	0.049
Mass flow rate of water vapour \dot{m}_{wv} [kg/s]	0.0007	0.00175	0

$$\dot{Q}_2 = \dot{m}_{da} C_{p2,da} T_2 + \dot{m}_{2,w} x_2 h_{2,g}$$

$$\dot{Q}_2 = (0.049) (1.007)(32) + (0.00175)(0.035)(2559)$$

$$\dot{Q}_2 = 1.74 \text{ kW}$$

$$\dot{Q}_3 = \dot{m}_{da} C_{p3,da} T_3 + \dot{m}_{3,w} x_3 h_{3,g}$$

$$\dot{Q}_3 = (0.049) (1.012)(130) + (0)$$

$$\dot{Q}_3 = 6.45 \text{ kW}$$

Energy Released/discharged (Q_d)

From equation (4-20) the energy discharged can be calculated as follows:

$$\dot{Q}_d = \dot{Q}_3 - \dot{Q}_2$$

\dot{Q}_d is 4.71 kW at a time of 1 h which can be seen in Figure 5-10. By integrating this curve, the total amount of energy released from the packed bed was 11.56 kWh (Q_d).

Energy Efficiencies of the System

The energy efficiencies of the system can be calculated from equations (4-23) to (4-25). A sample calculation is done below for charging cycle 1 and discharging cycle 2. The values substituted in these equations can be found in Table 5-1 and Table 5-2. The procedure to obtain those values is explained above.

Charging Efficiency (η_c)

$$\eta_c = \frac{Q_s}{Q_{in}} = \frac{13.64}{20.44} = 67\%$$

Discharging/Storage Efficiency (η_d)

$$\eta_d = \frac{Q_d}{Q_s} = \frac{11.56}{13.64} = 85\%$$

Overall Efficiency (η_o)

$$\eta_o = \frac{Q_d}{Q_{in}} = \frac{11.56}{20.44} = 57\%$$

Appendix D: Zeolite 13X Properties and Supplier Details



ZEOSORB™

13X APG Molecular Sieve



Description

ZEOSORB 13X APG is a superior grade synthetic zeolite of the type X-type crystal structure in sodium form, with a pore opening of 9 angstroms, allowing the adsorption of molecules with critical diameters up to 8 angstroms.

Application

ZEOSORB 13X APG is used for oxygen generation in both PSA and VSA systems as well as the adsorption of straight and branch chain hydrocarbons, aromatics NOx and SOx

ZEOSORB 13X APG has a very strong affinity for water vapour, carbon dioxide and nitrogen.

Typical Properties

PROPERTIES		BEADS			PELLETS	
Items	Units	8x12 Mesh	6x8 Mesh	4x8 Mesh	1/16"	1/8"
Diameter	mm	1.6 - 2.5	2.5 - 3.5	3.0 - 5.0	1.5 - 1.8	3.0 - 3.2
Bulk Density	g/ml	≥ 0.64	≥ 0.64	≥ 0.61	≥ 0.6	≥ 0.58
Crush Strength	N	≥ 25	≥ 45	≥ 60	≥ 25	≥ 60
Static Water Absorption ⁽¹⁾	wt%	≥ 28.5	≥ 28.5	≥ 28.5	≥ 27	≥ 27
Static CO ₂ Adsorption ⁽²⁾	wt%	≥ 19.5	≥ 19.5	≥ 19.5	≥ 18.5	≥ 18.5
Attrition	wt%	≤ 0.1	≤ 0.1	≤ 0.1	≤ 0.4	≤ 0.4
Moisture Content	wt%	≤ 1.0	≤ 1.0	≤ 1.0	≤ 1.0	≤ 1.0
Standard Packaging	kgs	140	140	140	125	125

⁽¹⁾ Measured @ 25 °C - 75% RH ⁽²⁾ Measured @ 25 °C - 250 mm Hg

ATTENTION:

Before handling this product, please refer to the appropriate material safety data sheet. (MSDS)

This product can be regenerated in PSA as well as heat regenerated systems. The maximum regeneration temperature not to exceed 350° C.

All information presented in this publication are perceived to be accurate and reliable. All risks and liability obtained by use of this product are assumed by the user. No warranties are made regarding the data of the products above whether it be expressed or implied. The user should not assume that data and safety measures are indicated or that other procedures may not be required.

For more information please do not hesitate to contact us

ZAN-TECH

7 Heron Park, River Horse Valley, Durban - South Africa
Ph: 031- 569 2997 - Fax: 031 - 569 2177 Email: sales@zantech.co.za

